



Iron-based photocatalytic and photoelectrocatalytic nano-structures: Facts, perspectives, and expectations



Yamen AlSalka^{a,b,*}, Luis I. Granone^{a,b}, Wegdan Ramadan^{a,b,c}, Amer Hakki^d, Ralf Dillert^{a,b}, Detlef W. Bahnemann^{a,b,e,*}

^a Institut für Technische Chemie, Leibniz Universität Hannover, Callinstr. 3, D-30167, Hannover, Germany

^b Laboratorium für Nano- und Quantenengineering, Leibniz Universität Hannover, Schneiderberg 39, 30167, Hannover, Germany

^c Faculty of Science, Physics Department, Alexandria University, 21511 Moharram Bek, Alexandria, Egypt

^d Department of Chemistry, University of Aberdeen, Meston Building, Meston Walk, AB24 3UE, Aberdeen, Scotland, United Kingdom

^e Saint-Petersburg State University, Laboratory Photoactive Nanocomposite Materials, Saint-Petersburg, Russia

ARTICLE INFO

Keywords:
Photocatalysis
Photoelectrocatalysis
Iron-based
Nanostructures
Perovskites
Ferrites

ABSTRACT

The increasing demand for clean renewable energy needed for sustainable industrial progress and population growth is the driving force for the scientific community to achieve a continuous development in the field of photocatalysis and photoelectrochemistry. Nanostructures and nanomaterials have contributed significantly to the field of renewable energy due to their new physicochemical properties. Iron-based nanostructures have considerable advantages like small band gaps, allowing to harvest photons in the visible region of the solar spectrum, abundance, and important physical properties like magnetism and ferroelectricity. But they also have many shortcomings and drawbacks related to stability in the different photocatalytic media, low surface area, conductivity, and fast charge carrier recombination. In this review, the focus is placed on important members of the iron-based photocatalyst family such as, hematite, iron oxy-hydroxide, iron-based perovskites, and spinel ferrites. Also, iron doped titanium dioxide as visible light photocatalysts is covered. Various strategies employed for enhancing the photocatalytic and photoelectrocatalytic performance are discussed. Doping, oxygen vacancies, induced defects and formation of solid solutions seem to be a working strategy to address some of the challenges in photocatalysis and photoelectrocatalysis. Finally, photocatalytic and photoelectrocatalytic applications employing iron-based semiconductors are presented.

1. Introduction

Iron-based oxide semiconductors proved to be promising materials for photocatalytic and photoelectrocatalytic applications in the fields of environmental remediation and solar fuel generation [1]. Hematite (α - Fe_2O_3) gained particular attention during the last three decades after its application as a functional material for the preparation of visible-light-active photoanodes for the water oxidation reaction in a photoelectrochemical cell (PEC) [2]. The growing interest in hematite is possibly attributed to its outstanding properties such as narrow band gap, non-toxicity, abundance of the constituent elements, and low cost [3,4]. Beyond any doubt, these are essential properties that all photocatalyst should meet in order to be useful for large-scale applications. Nevertheless, drawbacks such as poor electrical conductivity, short diffusion lengths, and short-lived charge carriers drastically reduce the activity of

pristine hematite [1]. In an effort to overcome these limitations, scientists have applied different techniques to prepare modified hematite photocatalysts [2]. An enhancement on the photocatalytic and photoelectrocatalytic activity was achieved by modifications such as morphology and size control, doping and co-doping, and surface engineering.

Recently, research focused into mixed iron oxides with the aim of synthesizing new materials with the advantages of hematite but lacking the above-mentioned drawbacks. A growing number of publications in the field of photocatalysis and photoelectrochemistry is possibly found for iron-based materials such as perovskite-type MFeO_3 [5] or spinel-type MFe_2O_4 (M = metal ion) [6,7]. Because some of the physicochemical properties of these mixed oxides are closely related with those of hematite, a well understanding of the structural, optoelectronic, and electronic properties of the latter is essential to tackle the study of these

* Corresponding authors at: Institut für Technische Chemie, Leibniz Universität Hannover, Callinstr. 3, D-30167, Hannover, Germany.

E-mail addresses: alsalka@iftc.uni-hannover.de (Y. AlSalka), bahnemann@iftc.uniXXHYPHENXXhannover.de, 0,0,2

> bahnemann@iftc.uni-hannover.de (D.W. Bahnemann).

complex materials.

In the first section of the present review, the physicochemical properties affecting the photocatalytic and photoelectrocatalytic behavior of hematite, with emphasis on the advantages and disadvantages of this material towards the solar-light-driven energy conversion, are described. The crystalline structure, light absorption properties, charge carrier kinetics, native point defects, and surface chemistry of pristine hematite are discussed. The influence of titanium as a dopant is also covered. Subsequently, the most outstanding improvements in the activity obtained by the combination of hematite and TiO_2 are reviewed. Special emphasis is made on the presentation of an emerging group of iron-based semiconductors, the iron based perovskites. These materials attract attention due to their exceptional magnetic and electronic properties. Among them, bismuth iron oxide (BiFeO_3 , BFO) represents the rare case where spontaneous antiferromagnetic ($T_N = 643$ K) and ferroelectric ($T_C \sim 1123$ K) order coexist well above room temperature [8,9]. Furthermore, the magnetization of BFO shows a size-dependant behavior [10]. The many intrinsic features of BFO and their effects on the photocatalytic activity make it an interesting material. In fact, BFO showed promising results for its application on visible-light driven water splitting. Other groups of promising iron-based semiconductors, such as spinel ferrites and iron oxy-hydroxides are presented, and their properties are discussed as well.

Finally, a compilation of the latest results and state-of-the-art efficiencies for photocatalytic and photoelectrocatalytic water treatment and water oxidation to produce oxygen using iron-based oxide semiconductors is provided.

2. Hematite as a model photocatalyst

Among the six known iron oxides ($\alpha\text{-Fe}_2\text{O}_3$, $\beta\text{-Fe}_2\text{O}_3$, $\gamma\text{-Fe}_2\text{O}_3$, $\epsilon\text{-Fe}_2\text{O}_3$, Fe_3O_4 , and FeO), hematite ($\alpha\text{-Fe}_2\text{O}_3$) is thermodynamically the most stable under aerobic conditions and consequently exhibits the highest abundance in soils and sediments [11,12]. Without any doubt, the abundance of its constituent elements is the most attractive property of hematite with a view to its application in solar energy conversion. This aspect, together with the non-toxicity, the high chemical stability, and the suitable optoelectronic properties makes hematite a promising photocatalyst [2]. However, the poor charge-transfer dynamics, fast charge carriers recombination times, and the unfavorable effect of point defects on the electronic properties decrease its efficiency [2,13]. The foremost physicochemical properties affecting the photocatalytic and photoelectrocatalytic behavior of hematite are discussed below, with emphasis on the advantages and disadvantages of this material towards the solar-light-driven energy conversion.

2.1. Crystalline structure

All Fe^{3+} oxides structures are characterized by the presence of octahedrons in which Fe^{3+} ions are surrounded by six O atoms [11,14]. Hematite, in particular, has a corundum-like ($\alpha\text{-Al}_2\text{O}_3$) structure consisting of layers of FeO_6 octahedrons linked by edge- and face-sharing and stacked perpendicular to the c direction (Fig. 1). The resulting hexagonal close-packed crystallographic system, with two-thirds of the octahedral interstices filled with Fe^{3+} ions and all the tetrahedral sites remaining unoccupied, belongs to the space group $R\bar{3}c$ [15]. One unit cell consists of six formula units and has the lattice parameters $a = 5.034$ Å and $c = 13.752$ Å. The high density of hematite, 5260 kg m^{-3} , is due to the distortion of the FeO_6 octahedrons caused by a regular displacement of the Fe^{3+} ions. This distortion is necessary to achieve an optimal face-sharing of the FeO_6 units. Another consequence of the Fe^{3+} displacement is the presence of two different Fe–O bond lengths.

2.2. Light absorption properties

The optical absorptivity is a key physicochemical property of photocatalysts since it defines the maximum amount of photons that is possibly harvested by a certain material. Furthermore, having the knowledge about the nature of the fundamental and excited states of light-induced electronic transitions is of utmost importance to understand the behavior of a photocatalytic material. For semiconductors, the energetic separation between the valence band and the conduction band, the band gap, can be determined by means of UV-vis-NIR spectroscopy. In the case of hematite, although the absorption spectrum in the near-infrared to the near-ultraviolet spectral region (2000–200 nm) is well known, the corresponding band assignment is still a matter of debate [15,17]. This is because the absorption bands is possibly assigned to three different electronic transitions: ligand field (LF) transitions, ligand to metal charge-transfers (LMCTs), and transitions due to the simultaneous excitation of magnetically-coupled adjacent Fe^{3+} ions [17,18]. Shortly, the LF transitions arise due to the excitation of an electron from the fundamental state ($^6\text{A}_{1g}$ in the case of high spin Fe^{3+} ions) to higher energy states formed due to the exchange splitting of the t_{2g} and e_g atomic orbitals. It is worth mentioning that all the possible transitions (predicted by the Tanabe-Sugano equations) are both spin- and parity-forbidden but become allowed due to the magnetic coupling of the electronic spins of neighboring Fe^{3+} ions [17]. LMCTs in hematite are the transitions from non-bonding molecular orbitals of the O^{2-} ions to the antibonding t_{2g} (3d) orbitals of the Fe^{3+} ions. Finally, the excitation of magnetically-coupled Fe^{3+} ions corresponds to the simultaneous electron transition on two neighboring Fe^{3+} ions (double excitation process). The energy of these transitions is approximately the sum of two single LF transitions.

Fig. 2 shows the Kubelka-Munk remission function in the visible and near-infrared regions obtained from a diffuse reflectance spectrum (Fig. 2a) and the visible and near-UV absorption spectrum (Fig. 2b) of hematite as published by Sherman et al. [17]. Based on the ligand field theory as well as on SCF molecular orbital calculations, the authors assigned the bands observed at 900 nm, 640 nm, 430 nm, 405 nm, 380 nm, 310 nm, and 290 nm to LF transitions. The signals observed between 480 nm and 550 nm were assigned to double excitation processes and the bands below 270 nm were addressed to LMCTs.

According to the assignment made by Sherman and Waite, the visible light absorption of hematite is a consequence of the electronic transitions between energy states formed due to the exchange splitting of the 3d orbitals in the Fe^{3+} ions, and not because of LMCTs between 2p O^{2-} and 3d Fe^{3+} orbitals. Indeed, Sherman attributed the photoactivity of hematite under visible light to the absorption tail of the LMCT band [19]. Hence, the band gap could be attributed to a combination between LF transitions and LMCTs and the valence band edge would consist of non-bonding molecular orbitals of the O^{2-} ions and the $^6\text{A}_{1g}$ fundamental state of the Fe^{3+} ions, and the conduction band edge would be constituted by the unoccupied energetic states formed due to the exchange splitting of the t_{2g} and e_g atomic orbitals in the Fe^{3+} ions. A valuable technique to determine the electronic structure of metal oxide semiconductors is the x-ray-absorption near-edge-structure spectroscopy at the oxygen K edge [20–23]. Ma et al. [24] and Wu et al. [25] agree that the top of the valence band is mostly ligand orbitals of O 2p character and the bottom of the conduction band are antibonding oxygen 2p states hybridized with Fe 3d orbitals. Theoretical calculations made by Lee et al. [13] support this experimental result.

2.3. Charge carrier kinetics

Charge carrier dynamics play a major role in semiconductor photocatalysis and photoelectrocatalysis. Properties such as carrier mobility, carrier lifetime, and diffusion length define how photogenerated electrons and holes migrate towards the surface of the material to interact with the respective acceptor and donor species. Hence, it is not

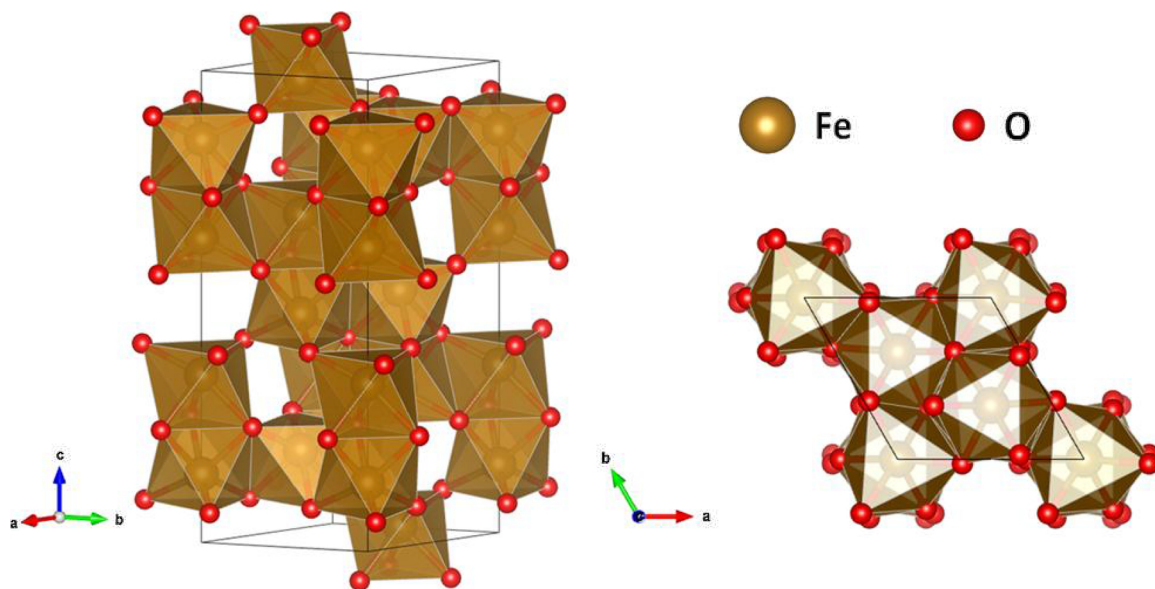


Fig. 1. Hematite unit cell (left) with a structure consisting of layered FeO_6 octahedrons linked by edge- and face-sharing. The FeO_6 units are stacked perpendicular to the c direction as can be seen from the view along the c axis (right). Crystallographic 3D structures were created using the VESTA 3 visualization system [16].

surprising to find several reports in the literature studying the charge carrier dynamics of hematite [26–35]. It is well known that carrier lifetimes and diffusion lengths are hematite's Achilles' heel. Short diffusion lengths and short excited-state lifetimes, as well as the high resistivity (in the order of $10^6 \Omega \text{ cm}$ for single crystal) are the main drawbacks limiting the photoelectrocatalytic activity [36]. Cherepy

et al. [31] studied the dynamics of photoexcited electrons in nanoparticulate hematite by femtosecond laser spectroscopy. **Fig. 3** shows the transient absorption decay profile obtained 8.3 ps and 48 ps after the excitation (390 nm laser). The signal, measured at 720 nm, was attributed to excited electrons at the bottom of the conduction band [37]. The fate of these excited species is trapping, relaxation into mid-

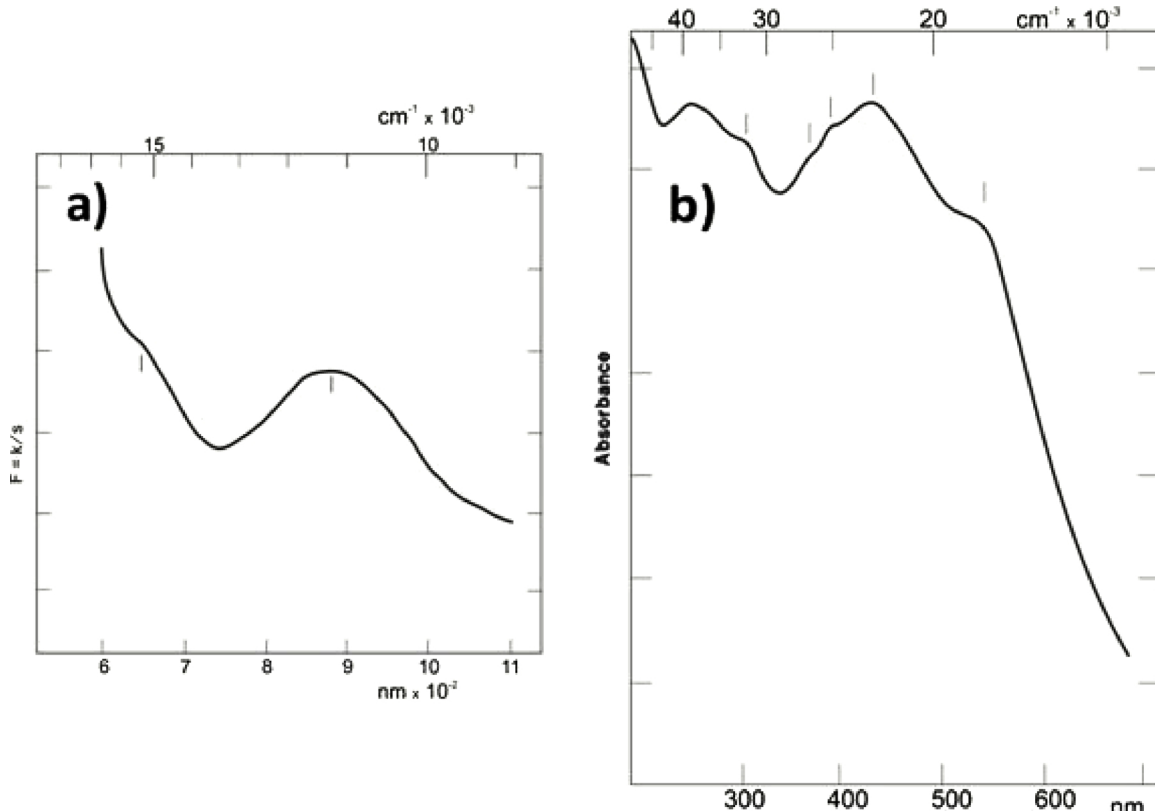


Fig. 2. (a) Kubelka-Munk remission function of hematite in the visible and near-infrared regions obtained from a diffuse reflectance spectrum. (b) Visible and near-UV absorption spectrum of hematite. The vertical lines indicate band positions. Adapted with permission from reference [17] (the spectra of goethite, lepidocrocite, and maghemite were removed from the original figure).

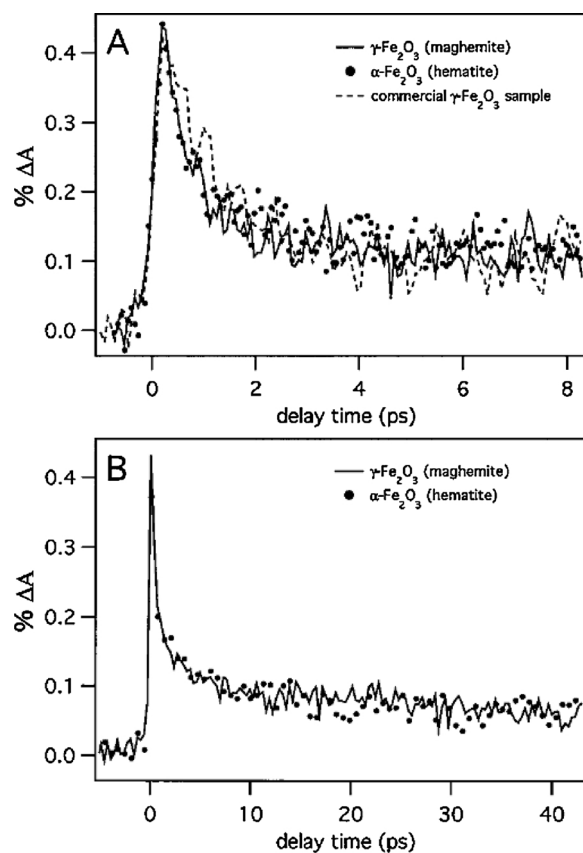


Fig. 3. Transient absorption decay profiles of nanoparticulate hematite (black dots) up to (a) 8.3 ps and (b) 48 ps after laser excitation. Reproduced with permission from reference [31].

bandgap states, or recombination with holes in the valence band and trap states. By fitting the decay profile with a triple-exponential decay function, the authors observed three decay processes with 0.36 ps, 4.2 ps, and 67 ps time constants related to electron-hole recombination mediated by intrinsic mid-bandgap states and trap states. None of the short-lived charge carriers remain longer than ca. 100 ps after the laser excitation.

In addition to the short lifetimes of the charge carriers of hematite, their mobilities were determined to be rather low. Morin obtained a value of $10^{-2} \text{ cm}^2 \text{ V}^{-1} \text{ s}^{-1}$ based on conductivity and Seebeck effect measurements [38]. This combination of the charge carrier mobility and lifetime results in a very short diffusion length of less than 4 nm [39]. Hence, low diffusion length and bulk recombination are the main reasons for the low photocatalytic and photoelectrocatalytic activities of pristine hematite [40]. Table 1 compares the carrier mobility, carrier lifetime, diffusion length, and donor density of visible-light-active hematite and WO_3 and UV-light active TiO_2 (anatase polymorph). The latter two compounds are commonly used as photoanode materials for water oxidation.

Table 1

Comparison of carrier mobility, carrier lifetime, diffusion length, and donor density of hematite, WO_3 , and TiO_2 (anatase polymorph).

Property	Hematite	WO_3	TiO_2 (anatase)
Carrier Mobility / $\text{cm}^2 \text{ V}^{-1} \text{ s}^{-1}$	0.01 [38,41]	10 [42]	0.1 [43]
Carrier Lifetime / ns	< 0.1 [31]	9 – 10 [42]	> 1000 [44]
Diffusion Length / nm	2 – 4 [39]	500 [42]	100,000 [44]
Donor Density / cm^{-3}	10^{18} [39]	10^{17} – 10^{20} [45]	10^{18} – 10^{20} [46]

From Table 1 it can be observed that the carrier mobility, carrier lifetime, and diffusion length of hematite are 10, 10⁵, and 10⁴ fold smaller, respectively than those of anatase TiO_2 . Comparing with WO_3 , hematite values are 10³, 10², and 10² fold smaller, respectively. The poor charge carrier dynamics of hematite is responsible for the lower photocatalytic activity observed under UV light irradiation when the three semiconductors are compared [47].

2.4. Native point defects

The incidence and consequences of native point defects is another physicochemical property of utmost importance for photocatalysts. Since different synthetic conditions possibly induce distinctive point defects on the crystal structure of the material, it is significant to understand whether these defects might have an effect on the photocatalytic activity. Lee et al. [13] theoretically investigated the native point defects in hematite using *ab initio* methods based on the density functional theory. They reported the change in the local atomic and electronic structures when oxygen vacancies, iron vacancies, interstitial oxygen, interstitial iron, and electron polarons have been introduced with the neutral charge state. Oxygen vacancies were found to produce a relaxation of the crystal structure together with the generation of three defect levels within the band gap. One of these levels consists of perturbed valence-band states whereas the other two correspond to orbitals belonging to Fe atoms that have become Fe^{2+} . Iron vacancies also produce an atomic relaxation in the structure but in a larger extent than oxygen vacancies. Shallow acceptor levels close to the valence band maximum are induced by Fe removal as well. Interstitial oxygen defects do not generate levels within the band gap except for shallow energetic levels near the valence band edge. Interstitial iron defects induce a significant strain field in the neighboring structure, generating levels that are mostly $\text{Fe d}_{(t_{2g})}$ orbitals. Because the interstitial Fe atoms donate two electrons to the adjacent Fe atoms, three consecutive Fe^{2+} centers are formed. This native point defect is responsible for the n-type behavior of hematite under ambient conditions.

Interesting results were obtained regarding the effect of an electron polaron in the density of states of hematite [13]. In addition to the relaxation produced around the host Fe atom [48], Hartree-Fock calculations showed that the electron polaron is 0.57 eV more stable than the delocalized electron in the conduction band (Fig. 4). As consequence of the formation of the electron polaron, the Fermi level is pinned by ca. 0.5 eV below the conduction band, hampering the photoelectrochemical performance of hematite photoanodes. In spite of this negative effect, the activity of hematite is possibly enhanced by manipulating the concentration of another type of native defects such as the oxygen vacancies. In this sense, defect engineering plays a fundamental role in the photocatalytic and photoelectrocatalytic properties of hematite and has been a matter of experimental research [36]. Ling et al. [49] showed that the photoactivity of pristine hematite towards

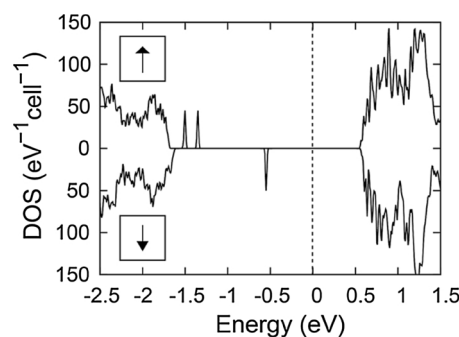


Fig. 4. Density of states of hematite in the presence of an electron polaron obtained via *ab initio* calculations. The Fermi level is indicated by the vertical dashed line. Reproduced with permission from reference [13].

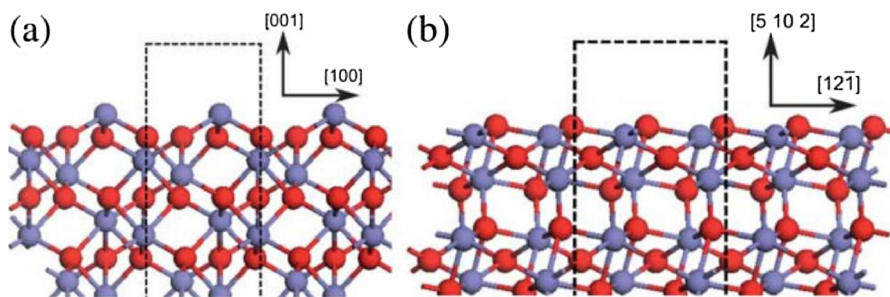


Fig. 5. Illustration of (a) [001] and (b) [012] surfaces. The red and grey balls stand for oxygen and iron, respectively. Partially reproduced with permission from reference [51]. (For interpretation of the references to colour in this figure legend, the reader is referred to the web version of this article.)

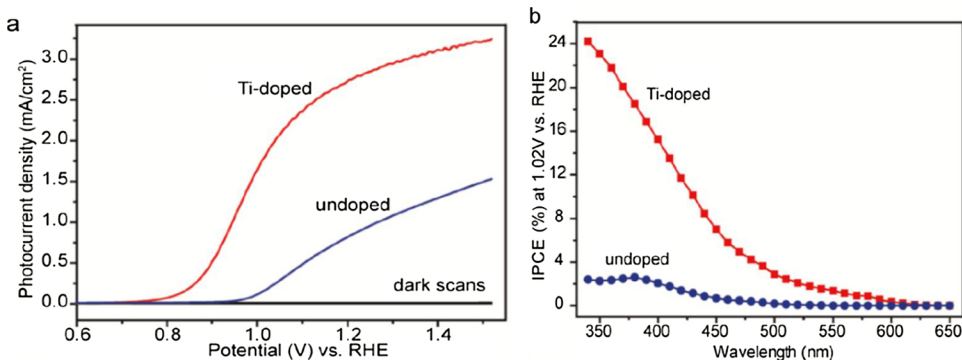


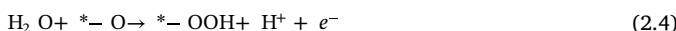
Fig. 6. (a) Comparison of photocurrent densities collected for optimized undoped and Ti-doped α -Fe₂O₃ films. (b) IPCE spectra of these two films collected at 1.02 V vs. RHE. Reproduced with permission from reference [60].

water oxidation can be significantly increased by inducing oxygen vacancies into the structure. This enhancement is due to the increased donor density resulting from the formation of Fe²⁺ sites, as was determined by electrochemical impedance spectroscopy. The Fe rich hematite was synthesized by thermal decomposition of β -FeOOH in an oxygen-deficient atmosphere.

2.5. Surface chemistry

Heterogeneous photocatalytic and photoelectrocatalytic water oxidation are surface-mediated processes. Therefore, the mechanism and dynamics of these reactions closely depend on properties such as adsorptivity and reactivity of the exposed surface of the semiconductor. The two natural growth faces of hematite are the [001] and the [012] surfaces [50] (Fig. 5).

Because of the layered structure, the [001] surface can exhibit an oxygen termination or an iron termination after cleavage [50]. The stoichiometric and non-polar Fe-terminated surface was suggested to be the most stable according to X-ray photoelectron diffraction and scanning tunneling microscopy experiments performed under ultra-high vacuum [52–54]. To model the water oxidation reaction, the following mechanism was considered [55,56]:



Here “*” represents a surface with one oxygen vacancy site immediately in contact with water. “* $-\text{OH}_2$ ”, “* $-\text{OH}$ ”, “* $-\text{O}$ ”, and “* $-\text{OOH}$ ” represents the surface with the corresponding chemisorbed species. The above mechanism was employed by Liao et al. [57] to calculate the reaction free energies for the fully hydroxylated [001] hematite surface.

By means of periodic density functional + U calculations, an overpotential value of 0.77 V was obtained for the water oxidation reaction under these conditions. This elevated extra energetic requisite for the light-assisted oxidation of water is another limitation of pristine hematite towards its application as photoanode.

Based on a thermodynamic morphology model with input parameters from reliable first-principles calculations and thermochemical data, the [012] surface was suggested to be the most stable one in hematite nanoparticles [51]. Although this surface has been also characterized under ultra-high vacuum [58] and in contact with water [50,59], the overpotential for the water oxidation has not been calculated due to computational complexity.

2.6. Ti-doped hematite and Fe-doped TiO₂

It is obvious from the main drawbacks of hematite, i.e., the very short diffusion length of the photogenerated holes (only 2–4 nm) and the poor carrier conductivity, that bare hematite will never fulfill all the criteria for efficient water oxidation unless certain modification is applied. One approach to improve the conductivity of hematite is by doping with different metals (e.g. Ti, Mn, Ta, Sn, etc.). In particular, titanium as a dopant element has received great attention because of its different roles in enhancing the practical performance of hematite. Wang et al. [60] have reported that doping of α -Fe₂O₃ with Ti results in a shift in the photocurrent onset potential of about 0.1–0.2 V to lower potential comparing with that of the undoped material (see Fig. 6).

Thus, improvement in the photocurrent and incident photon to current conversion efficiency (IPCE) at lower bias voltages occurs upon Ti doping. Based on electrochemical impedance spectroscopy and ultrafast transient absorption measurements, the authors attributed this enhanced photocurrent to an improvement in the donor density and a reduction in the electron-hole recombination at the time scale beyond a few picoseconds. Glasscock et al. [61] also observed a cathodic shift in the potential onset and, based on electrochemical impedance spectroscopy, this effect was attributed to the improved electrical

conductivity and the enhanced charge carrier density. Furthermore, Hahn et al. [62] attributed the high efficiency of titanium-doped hematite films to: (i) the improved electron transport within the bulk and (ii) the suppression of the recombination at the surface – electrolyte interface because of a stronger electric field near the surface.

Surface modification of semiconductor photoelectrodes with passivation overlayers is another effective strategy to improve charge-separation and charge-transfer processes across the semiconductor – liquid interface. Ahmed et al. [63] have successfully modified a nanostructured hematite photoanode with TiO_2 overlayers using a water-soluble titanium complex (i.e., titanium bis(ammonium lactate) dihydroxide, TALH). The thus modified nanostructured hematite photoanode exhibited a photocurrent response ca. 4.5 times higher (i.e., 1.2 mA cm^{-2} at 1.23 V vs. RHE) than that obtained by the bare hematite photoanode (i.e., 0.27 mA cm^{-2} at 1.23 V vs. RHE) measured under simulated solar light illumination. On the basis of steady-state polarization, transient photocurrent response, open-circuit potential, intensity-modulated photocurrent spectroscopy, and impedance spectroscopy measurements the authors concluded that the TiO_2 overlayer acts as a passivation layer of the surface states, thus reducing the surface electron – hole recombination.

Zhang et al. [64] have compared the performance of $\alpha\text{-Fe}_2\text{O}_3$ with that of Ti-doped $\alpha\text{-Fe}_2\text{O}_3$ and TiO_2 coated Ti-doped $\alpha\text{-Fe}_2\text{O}_3$. They have found that Ti-doped $\alpha\text{-Fe}_2\text{O}_3$ achieves a five time increase in the water oxidation photocurrent compared to the bare hematite. Based on electrochemical impedance spectroscopy, they attributed this effect to the promotion of the transport of charge carriers, including both, separation of photogenerated charge carriers within the bulk semiconductor and transfer of holes across the semiconductor – electrolyte interface. Fig. 7 illustrates the photogenerated charge carriers generation, recombination, and transport processes in the $\alpha\text{-Fe}_2\text{O}_3$, TiO_2 -coated Ti- $\alpha\text{-Fe}_2\text{O}_3$, and Ti- $\alpha\text{-Fe}_2\text{O}_3$ photoanodes. The presence of a TiO_2 layer (Fig. 7b) leads to a significant increase in the electron concentration. This results in (i) shifting the Fermi level toward the conduction band and thus increases the degree of band bending, (ii) improving the conductivity of the photoanodes, and (iii) facilitating the separation of the photogenerated electron – hole pairs in the space-charge layer.

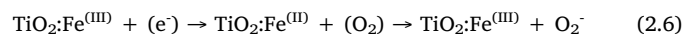
However, due to the more positive potential of the valence band maximum of TiO_2 compared to $\alpha\text{-Fe}_2\text{O}_3$, a hole injection barrier exists between Ti- $\alpha\text{-Fe}_2\text{O}_3$ and the electrolyte. This hinders the transfer of holes from the bulk hematite to the electrolyte, causes a loss of the photovoltage in the TiO_2 -coated Ti- $\alpha\text{-Fe}_2\text{O}_3$ photoanode, and leads to an anodic shift of the photocurrent onset potential. Interestingly, by later removal of this hole injection barrier, i.e., TiO_2 layer (see Fig. 7c), the hindrance in the Ti- $\alpha\text{-Fe}_2\text{O}_3$ photoanode will be eliminated and thus enhancing the photogenerated holes transfer from the bulk hematite to the electrolyte solution and further promoting the PEC water-splitting

performance by improving both the separation and injection efficiencies of photogenerated charge carriers.

Petit et al. [15] have correlated the structural aspects of Ti–Fe–O based materials, used as photoanode, with their efficiency for water oxidation. For this purpose, they have prepared Ti–Fe–O nanomaterials with iron and titanium atoms being combined in the same structure or into heterostructured nanocomposites. They have found that the nature of the obtained material depends strongly on the ratio of Fe/Ti atoms with Fe_2TiO_5 being the formed material at higher ferric concentrations whereas anatase TiO_2 doped with various amounts of Fe was formed at lower ferric concentrations. In order to test the efficiency of these different composites for the water oxidation reaction, Petit et al. have prepared nanocomposite electrodes with various compositions: $x\text{Fe}_2\text{TiO}_5/y\text{TiO}_2$ or $x\text{Fe}_2\text{TiO}_5/y\text{Fe}_2\text{O}_3$; x and y represent the weight percentage (%) of Fe_2TiO_5 and pure oxides, respectively. Fig. 8 summarizes the current density ($\mu\text{A cm}^{-2}$) they recorded at 1.8 V vs. RHE for these electrodes.

Among all thus prepared nanocomposites electrodes the one consisting of 25% Fe_2TiO_5 and 75% TiO_2 has generated the highest photocurrent. Petit et al. assumed that TiO_2 limits the fast charge carrier recombination due to both, the high absorption coefficient of TiO_2 compared to Fe_2O_3 and the higher electron mobility in TiO_2 compared to Fe_2O_3 .

On the other hand, iron has been considered a good candidate for TiO_2 doping. This is a promising method for modifying the properties of TiO_2 because it leads to the appearance of additional states in the band gap and, consequently, to an increase in the absorption of the visible light. Compared to undoped TiO_2 , Fe-doped TiO_2 usually exhibits enhanced light harvesting; however, controversial results on its photocatalytic activity have been reported. Wang et al. [65] have successfully synthesized Fe-doped TiO_2 with uniform doping and growth of particles yielding a highly active photocatalyst for the oxidation of methanol in oxygenated aqueous solution. The enhancement of methanol photocatalytic oxidation by Fe^{3+} -doping has been explained by assuming that the Fe^{3+} center acts predominantly as a shallow electron trap from which the electron is transferred to molecular oxygen more rapidly than in undoped TiO_2 :



Importantly, the authors found that the amount of Fe dopant per particle is a critical factor. A single Fe^{3+} center at particle is sufficient as a shallow electron trap for the optimal catalysis of the O_2 -reduction reaction. If more than one Fe^{3+} center is present per particle, a distribution of the catalytic activity will arise from their different positions in the bulk or at the surface of the photocatalyst, respectively. Alternatively, some of the $\text{Fe}^{(\text{III})}$ dopants might act as shallow hole traps (Eq. (2.7)) leading to an enhanced recombination of the trapped

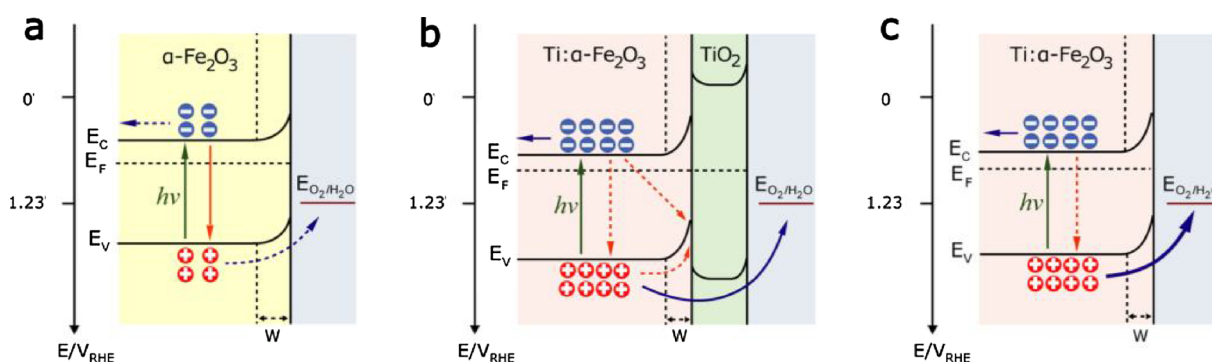


Fig. 7. Mechanism of charge generation, recombination, and transport processes at a bias of 1.23 V vs. RHE in (a) $\alpha\text{-Fe}_2\text{O}_3$, (b) $\text{TiO}_2:\text{Ti}:\alpha\text{-Fe}_2\text{O}_3$, and (c) $\text{Ti}:\alpha\text{-Fe}_2\text{O}_3$ Photoanodes. The green, red, and blue arrows refer to the charge generation, recombination, and transport processes, respectively, whereas the dashed and solid lines indicate the relative rates of the charge transport and recombination processes, in which the former represents the slower or impeded rates and the latter represents the faster rates. “W” represents the width of the depletion layer. Adapted with permission from reference [64]. (For interpretation of the references to colour in this figure legend, the reader is referred to the web version of this article.)

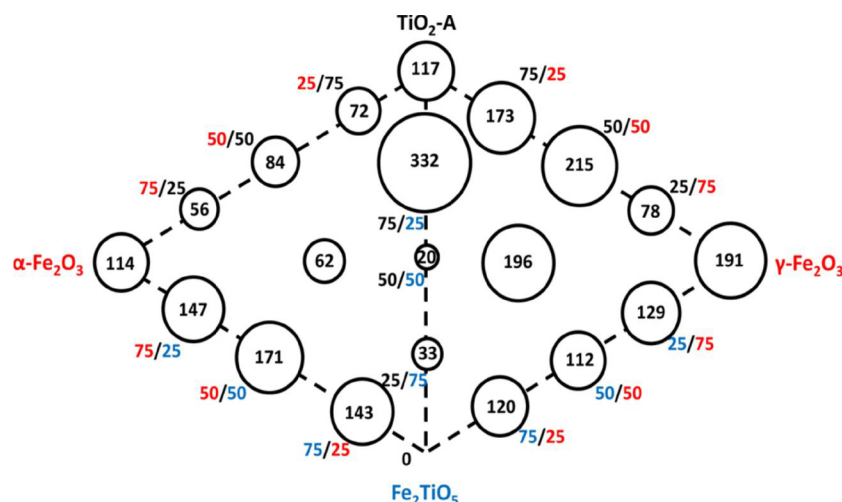
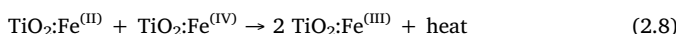


Fig. 8. Photocurrents measured at 1.8 V vs. RHE in aqueous NaOH, pH = 14, for the nanocomposite photoelectrodes with various compositions. The area of the circle is proportional to the photocurrents value in $\mu\text{A cm}^{-2}$. Reproduced with permission from reference [15].

charge carriers (Eq. (2.8))



Calculations performed by Wu et al. [66] showed that an increase in the concentration of iron in $\text{Ti}_{1-x}\text{Fe}_x\text{O}_2$ is consistent with the narrowing of the band gap of the semiconductor and, consequently, with the manifestation of the optical absorption and photocatalytic activity in the visible spectral range. However, the comparison of the calculated absorption in the iron-doped anatase and rutile with the experimental spectra which has been done by Krasil'nikov et al. [67] has shown that the most probable cause of the experimentally observed absorption in the visible region is the presence of hematite impurities in the samples.

3. Iron oxy-hydroxides

Compounds with the general formula FeOOH are known as iron oxy-hydroxides. There are five identified FeOOH polymorphs, namely, goethite (α - FeOOH), akaganéite (β - FeOOH), lepidocrocite (γ - FeOOH), feroxyhyte (δ - FeOOH), and a high-pressure crystal phase. Except for the latter, all the FeOOH polymorphs have been shown to be photocatalytically active semiconductors [68]. Among them, goethite is the most studied material and will be, therefore, discussed in more detail. All five polymorphs of iron oxy-hydroxide (α , β , γ , δ , and high-pressure) are formed by $\text{FeO}_3(\text{HO})_3$ octahedron specially arranged in five different ways [11]. Goethite has an orthorhombic unit cell (Fig. 9) consisting of a hexagonal close-packed array of O^{2-} and OH^- anions with Fe^{3+} cations occupying 1/2 of the octahedral sites [69]. Goethite has an antiferromagnetic structure below the Néel point (ca. 130 °C) and can acquire a thermoremanent magnetization when cooled in the presence of a magnetic field from its Néel temperature [70,71].

The UV-vis-NIR spectrum of goethite presents four absorption bands at ca. 900 nm, 650 nm, 450 nm, and 430 nm [11]. Morris et al. attributed the first three signals to ligand field transitions from the $^6\text{A}_{1g}$ fundamental state [72]. The transition at 430 nm (2.88 eV) was attributed to the intense ligand to metal charge-transfers between O^{2-} and Fe^{3+} ions [72]. Zhang et al. demonstrated that although bulk goethite is a direct band gap material ($E_g \approx 2.5\text{--}3.1$ eV), nano-goethite contains a significant amount of indirect band gap structure in the range of 2.1 eV to 2.6 eV [73]. Furthermore, the authors showed the band gap energies are size dependent and increase as the particle size decreases [73].

Scientific investigations analyzing the charge carrier dynamics of photogenerated electron-hole pairs in goethite are scarce. Ma et al. have studied the kinetics of interfacial electron-transfer processes in goethite suspensions systems containing methylviologen dichloride hydrate as an electron acceptor, but neither diffusion lengths nor lifetimes were investigated [74]. Katz et al. studied the electron injection process of ferrihydrite, a poorly ordered iron oxy-hydroxide [75]. By means of ultrafast optical transient-absorption spectroscopy, they found that the electron mobility of ferrihydrite enables the charge transfer between widely separated surface sites. Nevertheless, as for hematite, the lifetime of the carriers was observed to be less than 200 ps [75].

The conduction and valence band energetic edges of nanostructured Goethite were investigated by Jelle et al. [68]. The authors determined the valence band edge energetic position from XPS measurements and deduced the conduction band edge energetic position considering the band gap energy obtained from diffuse reflectance measurements. They reported values of ca. + 0.6 and + 2.8 V vs. NHE for the conduction band and valence band edge, respectively. The high positive potential of the valence band edge, more positive than the $\text{H}_2\text{O}/\text{OH}$ redox potential, results in a high oxidative power of photogenerated holes. However, the conduction band edge is more positive vs. NHE than the

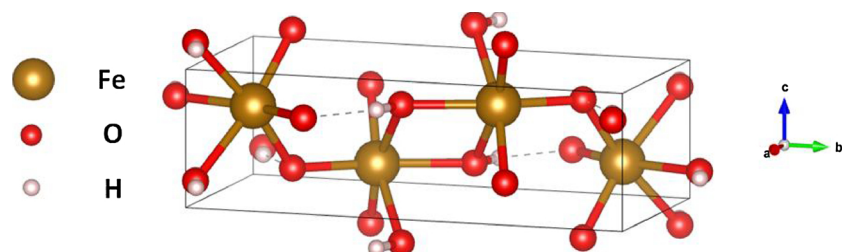


Fig. 9. Goethite unit cell showing the distinctive $\text{FeO}_3(\text{HO})_3$ octahedron present in all iron oxy-hydroxides. The crystallographic 3D structure was created using the VESTA 3 visualization system [16].

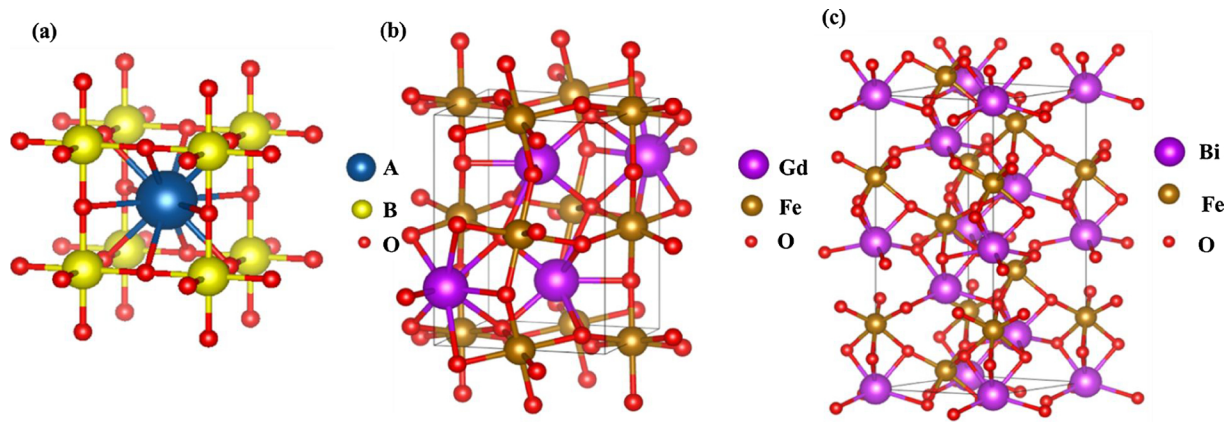
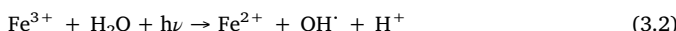


Fig. 10. (a) Crystal structure of simple cubic perovskite ABO_3 , (b) orthorhombic GdFeO_3 , (c) rhombohedral BiFeO_3 . Crystallographic 3D structures were created using the VESTA 3 visualization system [16].

O_2/O_2^- redox potential, resulting in a low reductive power of the photogenerated electrons [68]. Thus, the photogenerated electrons cannot react with dissolved molecular oxygen to produce superoxide radical anions and might therefore participate in the photoreductive dissolution of goethite [76]. Three different mechanisms are possibly involved in the photoreductive dissolution of goethite in the presence of an adsorbed electron donor: (i) a light-induced ligand-to-metal charge transfer resulting in the oxidation of the electron donor, the reduction of surface Fe^{3+} ions and the subsequent leaching of Fe^{2+} into the surrounding liquid; (ii) direct reduction of surface Fe^{3+} ions by photogenerated electrons; (iii) indirect reduction of surface Fe^{3+} ions by OH radicals resulting from the hole-mediated oxidation of surface OH groups [77,78]. Similar observations were reported for another iron-based compound, i.e., BiFeO_3 [79]. When formic acid is photocatalytically oxidized by BiFeO_3 , photogenerated electrons do not produce molecular hydrogen, but reduce surface Fe^{3+} ions instead [79]. In the presence of hydrogen peroxide (H_2O_2), Fe^{2+} is oxidized to Fe^{3+} and hydroxyl radicals are generated in the so-called photo-Fenton mechanism (Eqs. (3.1)–(3.3)) [80].



Due to the photo-Fenton mechanism, the photocatalytic activity of goethite is considerably enhanced in the presence of H_2O_2 at the expense of the photoreduction of the semiconductor [81–83]. The photoreductive dissolution of goethite is avoided when suitable electron scavengers are present in the suspension [74].

Goethite particles with various shapes and exposed facets have been synthesized and are widely described in the scientific literature [84,85]. Nevertheless, investigations regarding the effect of the different facets on the photocatalytic activity are limited. The first research on this subject was published in 2014 by Kakuta et al. [86]. They analyzed the decomposition of acetaldehyde on the [021] and [110] facets and found that the former shows a higher photocatalytic activity. They ascribed this effect to the higher concentration of Fe-OH sites on the [021] facet (3.4 sites per nm^2) in comparison to the [110] facet (2.8 sites per nm^2). The surface hydroxyl groups are assumed to act as hole acceptors to form hydroxyl radicals. This effect favors the charge-carrier separation and prevents the electron-hole recombination, enhancing the photocatalytic activity [86].

The main disadvantage of goethite, when compared with hematite, is its limited stability in alkaline media. It is well known that under cathodic condition goethite is reduced to iron (II) species [87], while under anodic potential it is rapidly oxidized to form soluble FeO_4^{2-} [88]. This hampers the application of goethite-based photoelectrodes for water oxidation/reduction reactions.

4. Iron-based perovskites

From the previous sections, it could be seen that hematite, which is the most stable and abundant iron-based oxide, and iron oxy-hydroxide, are having fundamental shortcomings when compared to other photocatalytic oxides like TiO_2 and WO_3 . In addition, the possible strategies that could be performed on hematite to improve its photocatalytic activity are limited because it is a binary oxide. Also, iron oxy-hydroxide, although being abundant and nontoxic, is highly unstable in alkaline electrolytes at high anodic potentials [88]. These deficits suggest to investigate other iron-based compounds and make use of an important fundamental property which is “magnetization” as well as other related properties like ferroelectricity. In this framework, iron-based perovskites are an interesting and versatile class of materials to study. The perovskites, with general formula ABO_3 , are a large family of compounds having a pristine cubic structure which was adopted originally from the mineral CaTiO_3 [89]. The A site is occupied by a large alkaline or rare earth metal ion and the B site is occupied by a relatively smaller d-block transition metal ion. Their crystal structure consists of BO_6 octahedra located in the 8 corners of the cube with the 12-fold coordinated A cation in the middle, as shown in Fig. 10a. However, the cubic structure is much affected by the ionic size and electronegativity of the cations A and B resulting in the observation of a Jahn Teller distortion effect of the ideal cubic structure [90–92]. This in turn leads to the formation of crystal structures having lower symmetry like orthorhombic or rhombohedral. Fig. 10(b–c) shows the crystal structure of some of the perovskites adopting non-cubic structures like GdFeO_3 and BiFeO_3 having orthorhombic and rhombohedral structures, respectively [93–96]. On the other hand, the anion site in the ABO_3 structure “O” refers to oxygen but also other large ions such as fluoride, chloride, bromide, or nitrite are possible [97,98]. The broad diversity of the properties of oxide perovskites is associated with their versatile crystal structures, in which around 90% of the elements in the periodic table can be accommodated [99]. As measure of the deviation from the ideal cubic structure, Goldschmidt [100] introduced a tolerance factor, t , which is used to define the degree of distortion in the structure upon changes in the ionic radii of A and B sites and is defined by:

$$t = (r_A + r_O)/(\sqrt{2}(r_B + r_O)) \quad (4.1)$$

where r_A , r_B , and r_O are the radii of the A cation, the B cation, and the anion, respectively. The cubic structure occurs if $0.89 < t < 1$ [92,101]. Lower values of t will lower the symmetry of the crystal structure. Perovskites, in general, are considered chemically stable, a property which is of most importance for any photocatalyst and photoelectrode material. On the other hand, most of the perovskites (in their pure form) have band gaps larger than 3 eV and can therefore only harvest UV light, and unfortunately photons with wavelengths less than 400 nm

only account for 3.5% of the solar spectrum [102].

Titanates, for example, have the nominal composition $ATiO_3$, where A is an alkaline earth metal such as Sr, Ca, or Ba or a transition metal like Mn, Co, Cu, or Fe. The highest band gap is shown for the $CaTiO_3$ member of the titanates family with $E_g = 3.6$ eV [103–106]. Alkali tantalate perovskites having nominal composition $ATaO_3$ where, A is Na, Li or K are particularly interesting since they are efficient for overall water splitting reaction but under UV irradiation [107–109]. The highest band gap for the undoped tantalates is recorded for the $NaTaO_3$ having $E_g = 4.2$ eV. The conduction and valence band positions of $NaTaO_3$ are at -1 V vs. NHE and 3 V vs. NHE respectively, at $pH = 0$ [110]. These values allow the degradation of many organic compounds like methanol, methane, and formic acid, but this is only achievable under UV light illumination [110]. While titanates seem available and cost effective, tantalates are compromised by the scarcity. The high cost of Ta precursors adds one more limitation, apart from being active only in UV light, to its utilization in technical applications.

Iron-based perovskites have the general formula $AFeO_3$, where A is a metal ion like Ca, Sr, Ba, Bi, La, Gd, Ga or Y [111–113]. On the other hand, iron-based compounds could also adopt the $FeAO_3$ structure, where A could be Ti [114], as will be discussed later. Hence, physical properties such as magnetism and/or ferroelectricity are added to the material. Both properties are beneficial for photocatalytic reaction. They facilitate extracting the photocatalyst from solution by an external magnet and assist in the separation of the photogenerated charges, respectively. Unlike titanates and tantalates, most of the iron-based perovskites have a band gap within the visible region of the solar spectrum. In this context, bismuth iron oxide ($BiFeO_3$ -BFO), a multi-ferroic member of the iron-based perovskites, represents the rare case where spontaneous antiferromagnetic ($T_N = 643$ K) and ferroelectric ($T_C \sim 123$ K) order coexist well above room temperature [8,9]. As mentioned above, BFO has a distorted perovskite structure. The unit-cell parameters are $a = 5.58$ Å and $c = 13.87$ Å, corresponding to a rhombohedral angle of 59.35°. BFO combines many intrinsic features that could enhance its photocatalytic performance. In the bulk form the Fe^{3+} electron spins are aligning in a canted G-type antiferromagnetic arrangement with a length of 62–64 nm. Hence, net magnetization will be enhanced by the uncompensated spins when the crystallite size is reduced below 62 nm, giving rise to a weak ferromagnetism [10,111–113,115]. Recently, BFO has also demonstrated good potentials as a photocatalyst because of its narrow band gap (~ 2.2 – 2.8 eV) [116–120] that enables it to utilize the visible region of the solar spectrum and that motivated further investigations of its potentials as a photocatalyst. Recent studies showed a direct band gap at ~ 2.5 eV and indirect band gap at ~ 1.8 eV [121]. Also, charge-transfer (CT) transitions and spectroscopic measurements of the dielectric function of $BiFeO_3$ single crystal [122] show a defect free intrinsic band gap of ~ 3.0 eV superimposed on a weak absorption band at 2.5 eV. This result signifies the effect of defects and oxygen vacancies on the band gap and the shifting of the optical properties into the visible region. Electronic-structure investigations have established the strongly hybridized nature of the valence band via the mixing of $Fe^{3+} d^5$ levels with O p and Bi s states that affects the chemical bonding [123,124]. Fig. 11 shows the absorption spectra of BFO film and the inset to the figure is a close-up to the spectrum from 1 to 2.2 eV that can be resolved into four different linear oscillator components. Two strong transitions observed near 3.6 and 4.8 eV are assigned as CT excitations and two broad reflectance bands between 1 and 2.5 eV predicted to be on-site d - d crystal-field excitations of Fe^{3+} ions in this energy range [125]. The two doubly degenerate d - d excitation ($^6A_{1g} \rightarrow ^4T_{2g}$ and $^6A_{1g} \rightarrow ^4T_{1g}$) energies of Fe^{3+} ions in $BiFeO_3$ were found to be located at 1.6, 1.7, 2.0, and 2.1 eV which are close to the reported values for a $BiFeO_3$ single crystal [125]. It is well known that the band gap of an oxide perovskite is mainly determined by the B cation d states at the conduction band and the O 2p states at the valance band. The large electronegativity differences between conventional B cations (such as Ti^{4+} , Zr^{4+} and Nb^{5+}) with a d^0

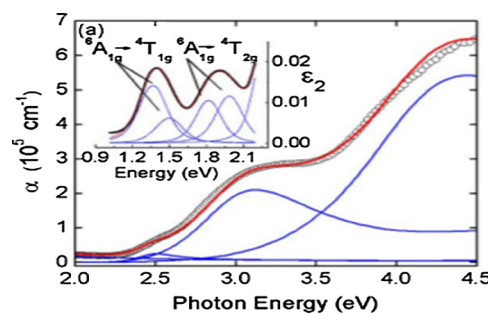


Fig. 11. Absorption spectrum obtained from $BiFeO_3$ film and. Inset is magnification from 1 to 2.1 eV. Reproduced with permission from reference [125].

electron configuration and the oxygen results in wide band gaps. In case of BFO the band gap is narrowed owing to the presence of partially filled d orbitals in Fe^{3+} . However, even for BFO with a band gap of 2.2 eV, only 25% of the solar energy can be absorbed. The small absorption coefficient further weakens the light harvesting capability of iron-based perovskites. The absorption coefficient of BFO at 400 nm is reported to be 10^4 to 10^5 cm^{-1} and becomes even lower in the visible range [126].

Iron-based perovskites have an intrinsic electric dipole moment due to a distortion in their crystal structures. This dipole moment induces the formation and alignment of ferroelectric domains that produce internal fields and high built-in potentials. This built-in potential promotes the separation of the photo-generated charges during the photoexcitation process [127,128]. Chen et al. [127] reported that the distortion of the octahedral sites, BO_6 , in BFO has an effect on the Fe–O bonds, the O–Fe–O angles within the octahedron, and the Fe–O–Fe angles between two nearest octahedrons. The reduction in the Fe–O bond deviation and the straightening in the O–Fe–O angles at the domain wall induce a marked band gap reduction as well as a shifting in the band edges of BFO [127]. The influence of ferroelectricity and the ferroelectric domain orientations on the charge separation and other physical properties of the BFO was demonstrated by Song et al. [129]. In their work, epitaxial BFO thin films with a bottom electrode layer of $SrRuO_3$ on $SrTiO_3$ substrates were deposited using pulsed laser deposition. They investigated the PEC properties of BFO films having ferroelectric domains with different crystallographic orientations, i.e. [001], [110], and [111]. Spontaneous polarization along the [111] orientation was found to be $110 \mu C/cm^2$, which is significantly higher than the $65 \mu C/cm^2$ for the [001] and $94 \mu C/cm^2$ for the [110] orientations, as shown in Fig. 12a. The photocurrent density along the [111] direction was also significantly enhanced to 0.080 mA/cm^2 at 0 V vs. Ag/AgCl, when compared to 0.0018 mA/cm^2 for the [001] direction, as shown in Fig. 12b. Furthermore, the band-edge position for BFO films having different domain orientations was obtained using Mott–Schottky plot. The calculated values of the CB for BFO thin films are shifted from -0.006 V vs. RHE for the [001] orientation to -0.286 V vs. RHE for the [111] orientation, indicating that the [111] has the highest band bending and giving rise to band positions that are energetically suitable for water splitting, as seen in Fig. 12c.

Distortion-induced ferroelectricity and its effect on the photocatalytic activity was also reported for perovskites other than the iron-based ones. $Sr_2Nb_2O_7$ is a niobate perovskite, and lower photocatalytic activity was expected for it due to the deviation of the bond angle of O–Nb–O from 180° . This change increased the migration energy of the charge carriers, thus hindering the photogenerated charges from migration and lead to higher possibility of recombination. Hence, it is plausible not to expect water splitting or photocatalytic activity for $Sr_2Nb_2O_7$. However, it shows water splitting activity due to a dipole moment along the perovskite layers resulting from the distortion of NbO_6 octahedra. It was suggested that it could enhance the charge separation of the photogenerated electrons and holes [130,131].

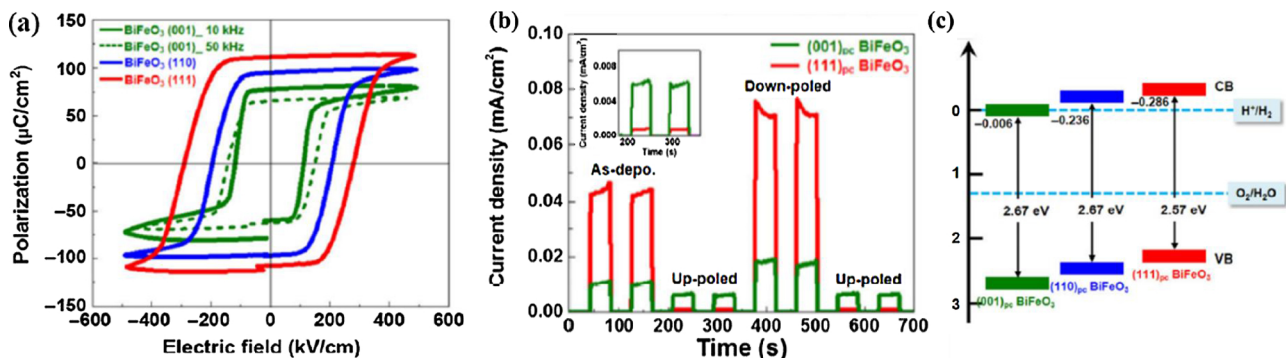


Fig. 12. (a) P – E hysteresis loop measurements for 400-nm-thick epitaxial BiFeO₃ thin films with different crystallographic orientations. (b) I – t curves for 50-nm-thick (001) and (111) BiFeO₃ thin-film photoanodes with different polarization states under zero bias (0 V vs. Ag/AgCl). (c) Band positions for epitaxial BiFeO₃ thin-film photoanodes with different crystallographic orientations. Reproduced with permission from reference [129].

Perovskites of the form $A_{1-x}A'_xB_{1-y}B'_yO_3 \pm \delta$ are particularly interesting [132,133]. They provide an opportunity to control the oxidation state of the transition metal (the redox properties) and the oxygen stoichiometry (δ) by partial substitution of the A- and/or B-site cations. This combination gives rise to a reticular “spongy-like” structure that offers many possibilities to tune the structural, physical and electronic properties of the material to fit photocatalytic requirements [134,135].

It is well established that the surface area of BFO synthesized by different methods is quite low compared to other oxides like TiO₂ and WO₃. This represents a major setback for the photocatalytic activity performance. However, the field of nanostructured semiconductors offer unique perspectives to sustain photocatalytic chemistry mainly due to the substantial dimensional reduction of the semiconducting framework and the large accessible pore surface. To improve the surface area of BFO, Papadas [136] used an inverse replica technique to nanocast well-ordered mesoporous BiFeO₃ with highly crystalline pore walls, large internal surface area of $141 \text{ m}^2 \text{ g}^{-1}$ and uniform pores with a volume of $0.16 \text{ m}^3 \text{ g}^{-1}$. This mesostructure exhibits substantially higher photocatalytic activity for water oxidation than the bulk-like and non-porous BiFeO₃ under UV-vis illumination.

Another iron-based member in the perovskite family is FeTiO₃, also known as ilmenite. It is one of the most common minerals in the earth [114]. It is an antiferromagnetic semiconductor with a band gap in the range of 2.59–2.9 eV. It has a rhombohedral structure and a Neel temperature of around 55 K. Unlike BFO, FeTiO₃ shows ferromagnetism at very low temperature, making it hard to utilize its magnetic properties at room temperature [137]. The pure FeTiO₃ phase still can be synthesized by solid state reaction at temperatures above 1200 C. Apart from the high temperature required for the synthesis, ilmenite has major shortcomings due to the instability of the Fe²⁺ ions. Zhang *et al.* [138] synthesized FeTiO₃ nanostructures with high energy facets via a facile one-pot hydrothermal approach. Different morphologies of FeTiO₃ nanostructures such as nanodisc, nanocube and nanooctahedron were adjusted by changing the amount of NaOH and the reaction time. The photocatalytic activity of these nanostructures was tested by the degradation of rhodamine B. The reactivity of the obtained FeTiO₃ nanostructures followed the order nanocube > nanooctahedron > nanodisc. By conducting electrochemical measurements on the different nanostructured materials, the authors found that the [012] facets shows the best photocatalytic activity.

The oxygen evolution reaction (OER) on metal oxides requires the coupling of 4-electron and proton transfer for the formation of an oxygen molecule. Grimaud *et al.* [139] discussed mechanisms that are fundamentally different from the conventional scheme. Based on their experimental data and density functional theory calculations, the authors showed that increasing the covalency of metal–oxygen bonds in perovskite oxides is critical to trigger lattice-oxygen oxidation and

enable non-concerted proton–electron transfers during OER. The understanding of new mechanisms and approaches could be beneficial to enhance OER in perovskites. Later studies indicated that perovskites electronic structure can be tuned to enhance OER activity and that could be done by the substitution of divalent ions in the A or B sites or by changing the oxygen vacancy content in the material [140,141]. It is proposed that oxygen vacancies left on the oxide surface from the OER can be refilled by OH[–] from the electrolyte. The subsequent deprotonation of these hydroxyl groups yields surface oxygen, which can diffuse and fill oxygen vacancies in the bulk of the oxygen-deficient perovskites [142,143]. Han *et al.* [142] studied the OER kinetics and the structural stability of iron-based and cobalt-based perovskites. The authors synthesized and investigated SrCoO_{3–} δ , SrFeO_{3–} δ , and Sr_xCa_{1–} x FeO_{3–} δ , whose fully oxidized forms (i.e. $\delta = 0$) have comparable O 2p-band centers (relative to the Fermi level) and metal–oxygen (M–O) covalency. They demonstrated that when the O 2p-band center is close enough to the Fermi level and when the M–O covalency is strong enough, like in SrCoO₃, the redox activity of the lattice oxygen in the perovskite structure will be activated during the OER, leading to the evolution of lattice oxygen. Furthermore, a pH-dependent OER activity was observed for the SrCoO_{3–} δ and CaFeO_{3–} δ samples [139]. Hence, an increase in the pH of the electrolyte can promote the kinetics of surface deprotonation and thus enhance the OER activity. However, SrFeO_{3–} δ and Sr_xCa_{1–} x FeO_{3–} δ exhibited a non-pH dependent OER, indicating a concerted proton-electron transfer. The authors expected similar redox activities of the lattice oxygen during the OER process upon replacing Co by Fe and partially replacing Sr by Ca i.e. Sr_xCa_{1–} x FeO₃. Nevertheless, this was not the case. Less oxygen can be intercalated into the lattice due to the reduced Fe–O–Fe bond distance in the FO₆ octahedron. Furthermore, the replacement of Sr by Ca reduces the Fe–O hybridization, shifts the Fermi level away from the O 2p band, and widens the band gap, making it difficult to intercalate oxygen into the lattice. These observations bring us again to the role of the lattice distortions in the photocatalytic and photoelectrocatalytic activity of perovskites. X-ray absorption spectroscopy measurements showed that an increase of the δ value from 0 to 0.5 will separate the O 2p band from the Fermi level by more than 0.8 eV. It will also weaken the Fe–O covalency by more than 0.3 eV in SrFeO_{3–} δ . Hence, the full oxidation of perovskites (i.e. the filling of oxygen vacancies) has a critical influence on the electronic structure and can determine the OER performance and mechanism.

4.1. Solid solutions based on Iron perovskites

A major limitation for using iron-based perovskites for large-scale photocatalytic and photoelectrocatalytic applications is their extremely low quantum efficiency [144]. Acquiring a set of desired properties on simple binary or ternary oxide is not an easy task, especially if many

requirements are needed to be fulfilled, such as stability, activity under visible light irradiation, and good efficiency. Solid solutions were found to be an effective approach to the combination of two or more oxides in one single compound benefiting from the properties of each oxide. One of the main advantages of solid solutions is that the properties of the resulting compound can be tuned in a systematic way to meet specific requirement. However, there is always the possibility of having a compound with new unexpected properties and not just a mixture of the individual oxides properties. SrTiO_3 (STO) and BFO are relevant materials due to their interesting properties. The attraction of STO for photocatalytic and/or photoelectrocatalytic water splitting is attributed to several facts. STO has a band gap energy of 3.2 eV with the conduction band edge located at ca. -0.5 V vs. RHE [145]. Furthermore, it has an ideal cubic perovskite structure, which is tolerant to different A- and/or B-site replacements [146], and a high chemical stability [147]. Finally, STO can be easily synthesized by many methods and into different shapes [148,149]. On the other hand, BFO has a much smaller band gap, 2.2 eV, but its photocatalytic efficiency is still limited due to its low conduction band position compared to the hydrogen reduction level [150], the usually small surface area and the low stability under reductive conditions [151]. Lu et al. [152] had synthesized a series of $\text{Sr}_{1-x}\text{Bi}_x\text{Ti}_{1-x}\text{Fe}_x\text{O}_3$ ($0 \leq x \leq 0.5$) solid solutions via a hydrothermal method. Up to 50% of BFO can be incorporated into the STO lattice without suffering significant changes in its cubic structure. They found that the microstructure of the compound depends on the Bi/Fe ratio. At an intermediate ratio of 0.4, a cubic structure exposing the (100) facet is dominant. At a Bi/Fe ratio of 0.1, the resulting particles are mainly spherical and are made up of agglomerations of nano-sized grains (Fig. 13a). Photocatalytic performance towards molecular hydrogen production showed a maximum for the platinized solid solution having the nominal composition $\text{Sr}_{0.6}\text{Bi}_{0.4}\text{Ti}_{0.6}\text{Fe}_{0.4}\text{O}_3$. 1 wt.% Pt was applied as co-catalyst and was loaded into powder sample using an impregnation method. H_2 production rate of $\sim 50 \mu\text{mol h}^{-1}$ was recorded corresponding to an apparent quantum efficiency $\sim 0.63\%$ at $\lambda \geq 250$ nm, as shown in Fig. 13b. This value is twice as much as pristine STO and almost five times greater than pristine BFO. The authors carried out density of state (DOS) near the Fermi levels to understand the observed activity and found out that the conduction band (CB) is dominated by Ti 3d orbitals and valence band (VB) is dominated by O 2p orbitals, as expected. DOS also indicated the formation of two sets of spin-polarized bands inside the band gap. They are mainly comprised of Fe 3d orbitals which are also contributing to the CB, indicating the hybridization between the Ti 3d and Fe 3d orbitals. As a consequence, a decrease in

the band gap of the solid solution comparing with that of the pristine STO is observed. On the other hand, the visible light absorption and photocatalytic activity can be understood as electron excitations from occupied Fe 3d orbitals to either empty Ti 3d orbitals or Fe 3d orbitals, i.e. $\text{Fe}^{3+} + \text{Ti}^{4+} \rightarrow \text{Fe}^{4+} + \text{Ti}^{3+}$ or $2\text{Fe}^{3+} \rightarrow \text{Fe}^{2+} + \text{Fe}^{4+}$.

Single crystals are the right form to investigate intrinsic properties and performance of materials without the complications connected to their structural features such as sizes, orientations, densities and distribution of crystalline grains, specific surface areas, and particle – particle or particle – conducting layer interface. Cho et al. [151] reported on the photoelectrochemical activity of high quality single crystalline solid solution thin films of STO-BFO prepared by pulsed laser deposition. Films with thickness around 180 nm were deposited on a conductive layer of SrRuO_3 (SRO)-buffered STO substrate and later used as photoelectrode. Fig. 14a shows a set of characterizations indicating the high quality of the single crystalline solid solution thin films. The BFO film exhibited a cathodic photocurrent because the Bi loss during the deposition processes leads to p-type conductivity [153,154]. The BFO:STO solid solution with molar ratio 3:1 exhibited the highest photocurrent density. The photoelectrodes also produced stable photocurrent for 12 h. Faradaic efficiencies of H_2 and O_2 formation close to 100% were measured as shown in Fig. 14b. These results indicate that the solid solution photoelectrodes have a good stability and the photogenerated charges are successfully collected for water splitting, accomplishing a solar-to-hydrogen energy conversion. It is worth mentioning here that the photoelectrodes showed high stability in basic solutions (pH 12). Most of the photocathodes are active and stable in the acid medium, while most of the photoanodes are stable under a natural or basic medium, except for WO_3 [155,156]. Thus, in the two-electrode system (photocathode and photoanode) and for unassisted water splitting, the stability of the photocathode is basic solutions is essential.

5. Ferrites

Ferrites with the general formula MFe_2O_4 (M = metal ion) are considered as promising materials to substitute hematite as a visible light active iron-based photocatalyst. Most ferrites crystallize in the spinel structure, a face-centered cubic structure with Fe^{3+} and M^{2+} ions occupying octahedral and/or tetrahedral sites. When M^{2+} and Fe^{3+} ions occupy 1/8 of the tetrahedral sites and 1/2 of the octahedral sites, respectively, a so-called normal spinel structure is formed (${}^T[\text{M}]^0[\text{Fe}_2]\text{O}_4$) [6]. Typical examples of spinel ferrites showing a

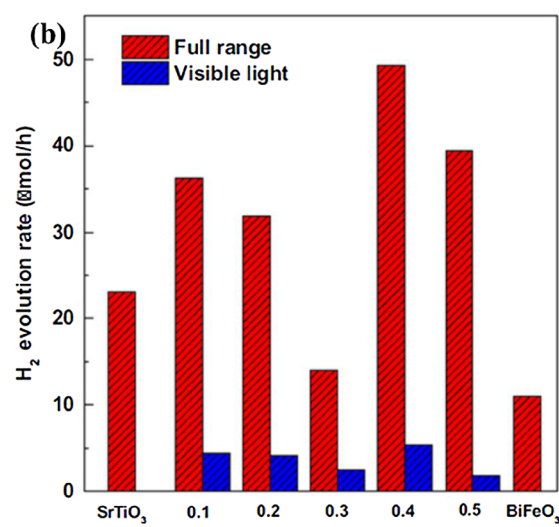
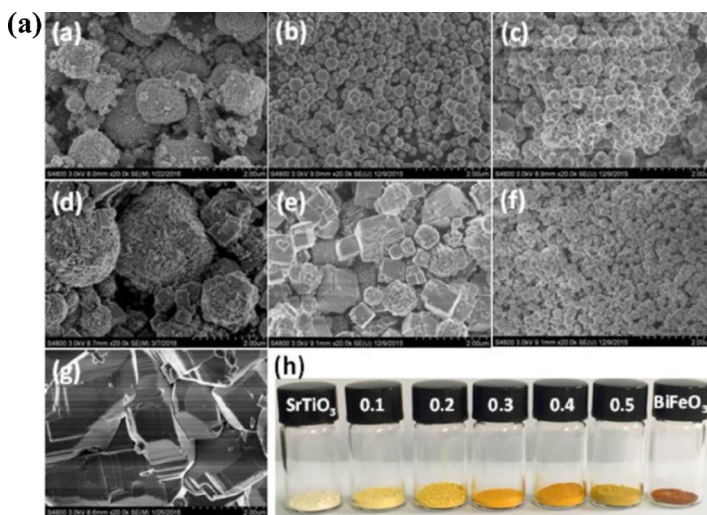


Fig. 13. (a) Field emission scanning electron microscopy images of $\text{Sr}_{1-x}\text{Bi}_x\text{Ti}_{1-x}\text{Fe}_x\text{O}_3$ ($0 \leq x \leq 0.5$), SrTiO_3 ($x = 0$) BiFeO_3 ($x = 1$) and (h) a photograph of sample powders. (b) Average photocatalytic hydrogen production rate under full range irradiation ($\lambda \geq 250$ nm) and visible light irradiation ($\lambda \geq 400$ nm). Reproduced with permission from reference [152].

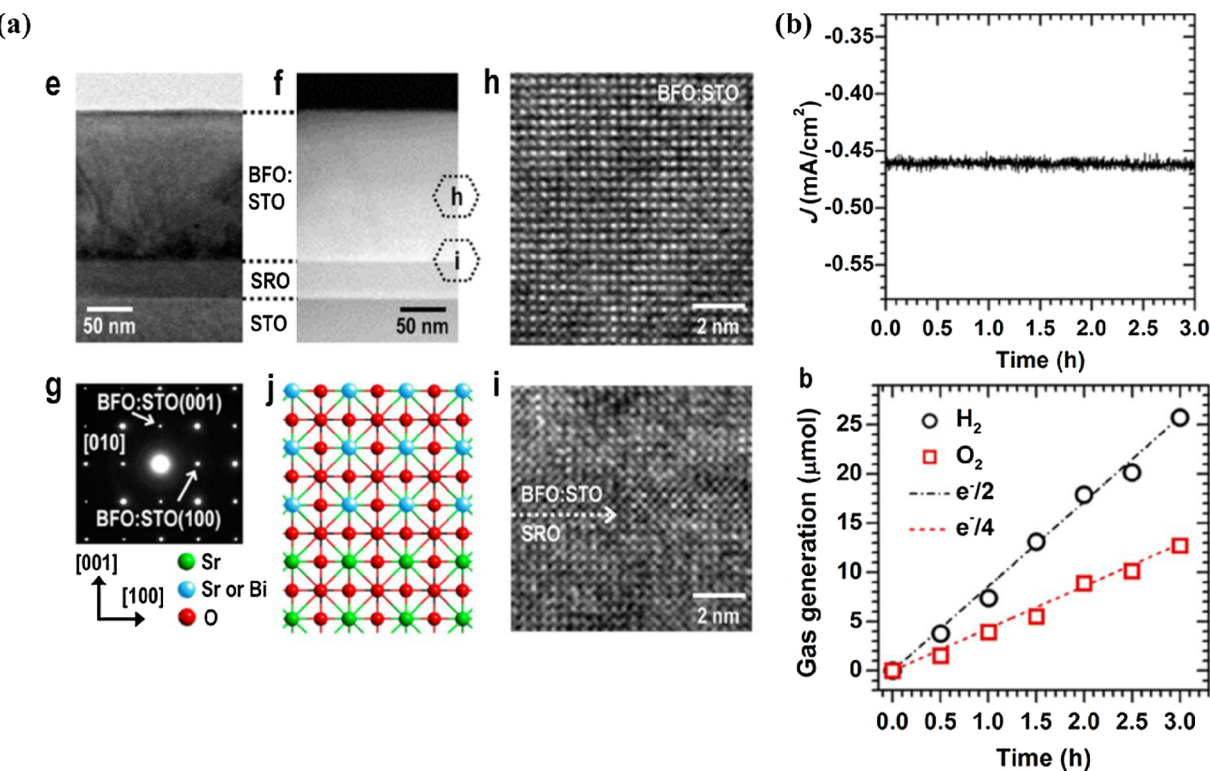


Fig. 14. (a) (e–f) TEM and high-angle annular dark-field scanning transmission electron microscope (HAADF-STEM) images of a BFO:STO (3:1) film on SRO/STO, respectively. (g) SAED pattern of BFO:STO film along the [010] zone axis. (h and i) High resolution cross-sectional TEM images on BFO:STO film and around the interface between BFO:STO film and SRO film, respectively. (j) Crystallographic model of the interface between BFO:STO solid solution and SRO films. (b) Current – time curve of BFO75-STO25 film/Pt, at 0 V vs. RHE. Amount of hydrogen and oxygen evolved by the photocathode, matching the number of charges measured. The theoretical lines were calculated according to Faraday's law of electrolysis. Reproduced with permission from reference [151].

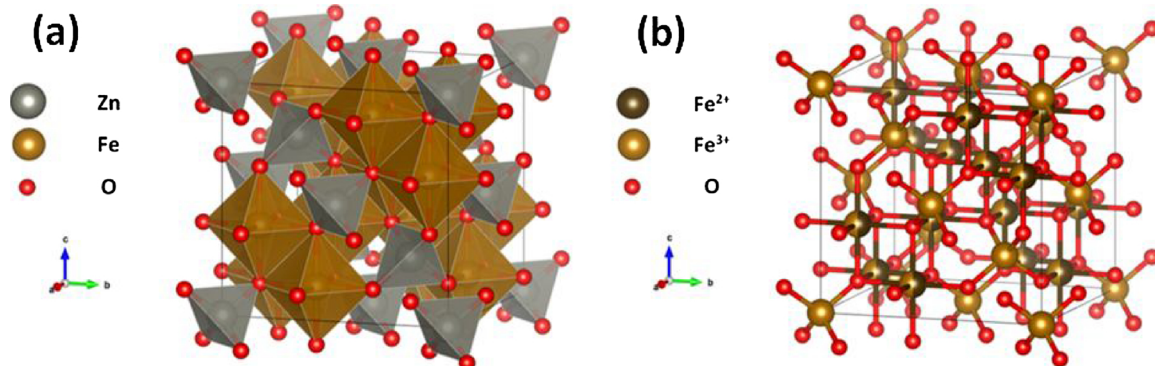


Fig. 15. (a) ZnFe₂O₄ unit cell with a normal spinel structure. Zn²⁺ and Fe³⁺ ions occupy 1/8 of the tetrahedral sites and 1/2 of the octahedral sites, respectively. (b) Fe₃O₄ unit cell with an inverse spinel structure. Fe²⁺ ions occupy 1/4 of the octahedral sites and Fe³⁺ ions occupy 1/8 of the octahedral sites and 1/4 of the tetrahedral sites. Crystallographic 3D structures were created using the VESTA 3 visualization system [16].

normal structure are ZnFe₂O₄ (Fig. 15a) and CdFe₂O₄. When M²⁺ ions occupy 1/4 of the octahedral sites and Fe³⁺ ions occupy 1/8 of the tetrahedral sites and 1/4 of the octahedral sites, a so-called inverse spinel structure is formed (Th[Fe]^{Oh}[FeM]O₄). NiFe₂O₄, CoFe₂O₄, and Fe₃O₄ (Fig. 15b) are typical examples of spinel ferrites having an inverse structure [6]. Between normal and inverse structure, spinel ferrites can adopt intermediate configurations defined as Th[M_(1-x)Fe_x]^{Oh}[Fe_(2-x)M_x]O₄, where x, the degree of inversion, can take values from 0 (normal structure) to 1 (inverse structure) [6]. Several factors, such as ionic radius, electronic configuration, and electrostatic energy (Madelung energy) can influence the distribution of the metal ions between the tetrahedral and octahedral sites [157]. Furthermore, the degree of inversion depends also on the synthetic conditions [158–161]. Like hematite, ferrites have a high chemical and thermal

stability in aqueous systems [162].

Unlike hematite, most of the spinel ferrites are magnetic materials both in a nanoparticulate or bulk form. As was described by Néel [163], the magnetic moment of ferrites are the sum of the magnetic moments of the individual cations in octahedral (Oh) and tetrahedral (Th) positions. Usually, the Oh-Th interactions are stronger than the Oh-Oh and the Th-Th interactions. The dominant Oh-Th interaction leads to complete or partial (non-compensated) anti-ferromagnetism (ferromagnetism) [163,164]. Another significant difference between hematite and ferrites is related to their band gap energies. The latter possesses narrow band gaps below 2 eV. Fig. 16 shows the band gap energies and the band-edges energetic positions for some semiconducting ferrites. As can be seen from this figure, ferrites such as *n*-MgFe₂O₄ and *n*-ZnFe₂O₄ are promising materials for photocatalytic and

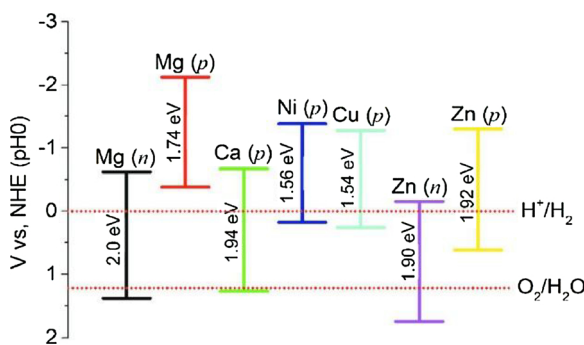


Fig. 16. Band-gap energies and band-edges energetic positions of representative ferrites (*n* and *p* refer to the semiconductor type of ferrites). Reproduced with permission from reference [165].

photoelectrocatalytic water oxidation whereas *p*-NiFe₂O₄, *p*-CuFe₂O₄, and *p*-CaFe₂O₄ might be suitable for water reduction [6,7,165]. Like hematite, the optical absorptivity of ferrites in the UV–vis–NIR range is dominated by ligand filled transitions of the octahedrally or tetrahedrally coordinated Fe³⁺ [166,167]. Ferrites with M²⁺ consisting in a transition metal with an electronic configuration different than d⁰ and d¹⁰ will also exhibit the inherent ligand filled transitions of the octahedrally or tetrahedrally coordinated M²⁺ cations [166].

A large number of scientific publications analyzing the photocatalytic activity of ferrites can be found in the literature [6,7,168]. Generally, the performance of these materials is far from the predicted theoretical maximums [169]. Authors attribute this effect to the strong recombination within the bulk or in the surface of the materials and to the Fermi level pinning produced by the large density of surface states [169]. Furthermore, experimental evidence suggest a very low mobility and short diffusion lengths of the charge carriers [169].

6. Iron-based core-shell nanostructures

The practical applications and performance of photocatalysts could be enhanced if obvious problems arising from using fine powders are addressed: The separation of fine particles used after the treatment process and the recycling of the photocatalyst, the low photon efficiency and the instability of some photocatalysts at the different environments used in photocatalytic reactions [79,170]. Unlike single-component catalysts, multi-component can be designed to integrate many functions into one system. Core–shell nanostructures with a magnetic core can be conveniently collected and separated using an external magnet [171]. Ferrites are among the widely used magnetic materials as a core in the core–shell nanostructures, they have a nominal composition of MFe₂O₄, where M incorporates various cations: transition metal like Ni, Fe, Co and Zn, alkaline earth metal like Sr, Ba and Ca or a combination of both. Many of their intriguing characteristic are beneficial to the field of photocatalysis. The narrow band gap of the ferrites [172] promotes visible light photocatalytic reactions. They have a good electrical conductivity due to the electron hopping process between different valence states of metals in O-sites, which is beneficial for the transfer of charge carriers [173]. Furthermore, ferrites have good superparamagnetic properties, low toxicity, easy preparation, high adsorption ability, low cost, and abundant resources [174]. These set of properties are common in most of the iron-based oxides with exception of hematite (α-Fe₂O₃) which is antiferromagnetic. Miaomiao Ye et al. [175] reported on the synthesis of the core–shell Fe₃O₄/SiO₂/TiO₂ nanocomposites fabricated in two steps; sol gel followed by calcination step. It has strong magnetic smooth core of Fe₃O₄, interlayer of SiO₂ and top thin layer of TiO₂ of ~12.6 nm. Fig. 17a:c shows the TEM images of the developed particles after the synthesis step of each layer of the nanocomposite. Their core shell structures showed important features: fast separation and recyclability for water treatment against

RhB due to its Fe₃O₄ magnetic core. The magnetic core is stabilized with an interlayer of SiO₂ that minimize chemical and /or photo dissolution of the magnetic core and the outer layer is composed of finite size TiO₂ nanocrystal having high surface area, which is the photocatalytic active layer. Finite size TiO₂ in water shows turbid suspension however, upon the application of external magnetic field, the solution quickly becomes transparent within 1 min due to the rapid harvest of the majority of the magnetic photocatalyst, and only 10 min is necessary to completely remove all of the composite nanoparticles, as shown in Fig. 17d. The Fe₃O₄/SiO₂/TiO₂ core–shell nanocomposite exhibits high photocatalytic efficiency, which is comparable to that of the well-known commercial TiO₂ (Degussa P25) plus high recyclability up to 18 cycles as shown in Fig. 17e.

The life time of the excited state charge carrier in most of the oxides is short (order of picosecond, 10⁻¹² sec) and they also have large surface overpotential and both are key factors in the fast charge recombination and the loss of most of the photoinduced carriers [3]. Significant improvement in the charge recombination could be achieved by surface modification in which core–shell nanocomposite could serve as a way to achieve this goal. α-Fe₂O₃, is an n-type semiconductor with E_g ~ 2.2 eV and is used as a visible light photocatalyst, coupling with a wide bandgap semiconductor such as ZnO, TiO₂, or SnO₂ could provide a mean to shift the photocatalytic activity of these oxides from UV to visible light plus boosting the separation of the photoexcited charges [176–178]. In this context, Yu-Kuei Hsu et al. [179] fabricated α-Fe₂O₃/ZnO core–shell nanocomposite such that ZnO nanowires of diameter 80 nm was grown via hydrothermal on FTO substrate followed by the deposition of α-Fe₂O₃ shell of few nm on top. The core–shell structure showed enhanced PEC performance compared to naked ZnO wires and α-Fe₂O₃ films. The onset potentials of the ZnO nanowires and α-Fe₂O₃ thin film were approximately -0.5 and 0 V, respectively. When the surfaces of the ZnO nanowires were uniformly covered with a thin layer of α-Fe₂O₃ as shell, the photocurrent increased significantly to 1.5 mA cm⁻². Also, the photo responses of the ZnO/α-Fe₂O₃ core–shell nanowires and that of bare ZnO show onset wavelengths of photocurrent generation about 600 and 390 nm, respectively, in the electrolyte. According to this comparison, the existence of an α-Fe₂O₃ shell layer is responsible for the conversion from UV to visible light as indicated from the results of absorption spectra. The enhanced activity of the core–shell nanocomposite stems from the formation of n/n heterojunction. Electrochemical impedance spectra were measured for bare ZnO nanowires and α-Fe₂O₃ thin film in darkness to estimate the position of their flat-band potential. From Mott Shottky measurement, the values of the flat-band potential for ZnO and α-Fe₂O₃ are -1.09 and -0.79 V, respectively [179]. From the measured flat-band potential and the band gap energy, the edges of the valence band and conduction band for ZnO and α-Fe₂O₃ before and after contact could be constructed and are shown in Fig. 18. The conduction band of α-Fe₂O₃ is lower than that of ZnO, but the energy difference between the conduction band and Fermi level in α-Fe₂O₃ is larger than that of ZnO because of the higher carrier concentration of ZnO. After contact of the n/n heterojunction, the electrons in the Fermi level of ZnO migrate to the Fermi level of α-Fe₂O₃ until their Fermi levels equalize, which would make the conduction band of ZnO lower than that of α-Fe₂O₃, because of the smaller energy difference between the conduction band and Fermi level in ZnO. The photogenerated electrons in α-Fe₂O₃ can easily transport to ZnO, due to the lower conduction band of ZnO. Relative to an α-Fe₂O₃ thin film, the onset potential of ZnO/α-Fe₂O₃ core–shell nanowires showed a significantly negative shift, which would benefit the water splitting at a smaller voltage. Furthermore, in contact with the electrolyte, under equilibrium conditions, the surface band bending becomes significant. This features collectively, would further serve as an efficient mechanism for charge separation. Although the iron-based core–shell nanostructures seem tempting and offer many choices towards the retrieving, the recyclability and the functionality of the photocatalyst but the stability of the

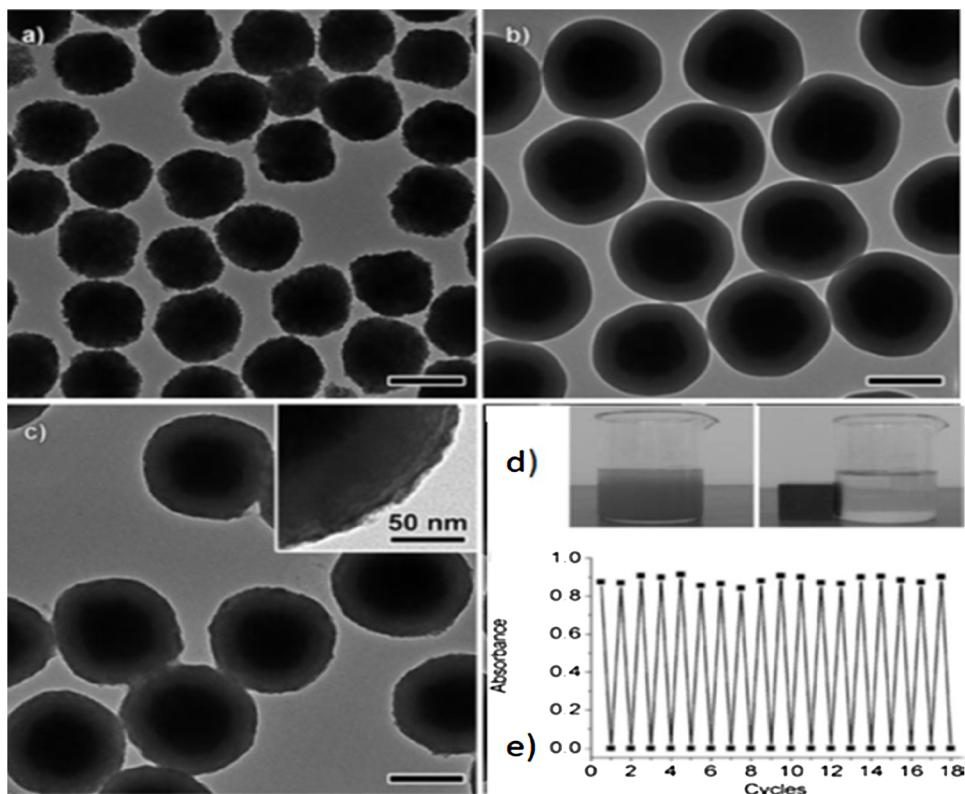


Fig. 17. TEM images of (a) Fe_3O_4 , (b) $\text{Fe}_3\text{O}_4/\text{SiO}_2$, (c) $\text{Fe}_3\text{O}_4/\text{SiO}_2/\text{TiO}_2$, (d) Separation process of $\text{Fe}_3\text{O}_4/\text{SiO}_2/\text{TiO}_2$ by using a magnet and (e) 18 cycles of the photocatalytic degradation of RhB in the presence of $\text{Fe}_3\text{O}_4/\text{SiO}_2/\text{TiO}_2$ core-shell structures (adopted from [175]).

magnetic core is still a concern [79]. Protecting the magnetic core from leaching into the solution or suffering photo / chemical corrosion during the photocatalytic reaction is of concern and further investigations need to be conducted to ensure reproducibility and stability.

In most of the reported cases, when a magnetic oxide is used as the core in a core-shell nanostructure, it utilizes its magnetic properties and its ability to interact with an external magnet to extract the photocatalyst from the system and recycle it for further reuse. On the other hand, the formation of heterojunction could have duel function such that it serves as a mechanism to separate the photogenerated charges along with the separation of the photocatalyst from the system.

7. Magnetic properties of iron oxides

The magnetic properties of iron oxides arise mainly from electronic exchange interactions between Fe ions on adjacent sites in the

crystalline structure [11]. This results in the parallel or antiparallel alignment of the atomic spins. Another exchange process, so-called super-exchange process, allow the coupling of unpaired electrons in the e_g orbitals of Fe^{3+} cations with electrons on the p orbitals of surrounding O^{2-} or OH^- anions [180,181]. The super-exchange process results in a chain coupling effect extended through the crystal [11,180,181]. Table 2 compiles magnetic parameters of the three iron oxides discussed in the previous sections, namely, hematite, goethite, and magnetite. The Neél temperature is the temperature above which antiferromagnetic materials become paramagnetic, i.e., they lose the microscopic magnetic ordering [182]. The analog of the Neél temperature for ferromagnetic and ferrimagnetic materials is the Curie temperature [182]. The magnetic saturation is the maximum magnetization that a material can accumulate by the action of an applied external magnetic field. The susceptibility indicates how responsive a material is to an applied magnetic field and the coercive force or

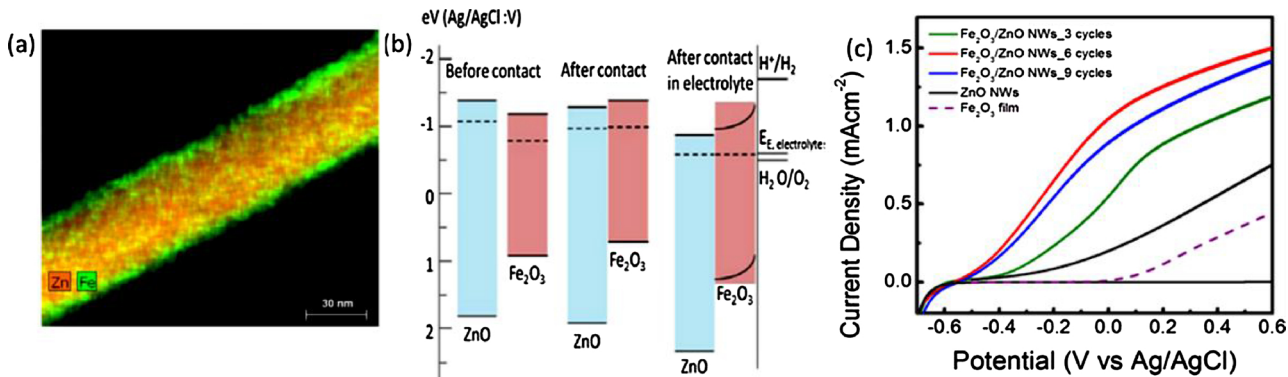


Fig. 18. (a) FE-TEM of $\alpha\text{-Fe}_2\text{O}_3/\text{ZnO}$, (b) Energy diagram of ZnO and $\alpha\text{-Fe}_2\text{O}_3$ before and after contact, (c) Photocurrent – voltage responses of the $\text{ZnO}/\alpha\text{-Fe}_2\text{O}_3$ core – shell nanowires. (adopted from [179].

Table 2

Magnetic structure, Neél and Curie temperature, coercive force, susceptibility and remanent magnetization of hematite, goethite and magnetite.

Property	Hematite	Goethite	Magnetite
Magnetic structure	Weakly ferromagnetic [11]	Antiferromagnetic [11]	Ferrimagnetic [11]
Neél temperature / K	–	400 [11]	–
Curie temperature / K	956 [11]	–	850 [11]
Magnetic saturation / kA m ^{−1}	2.5 [183]	≈ 1.5 [184]	480 [183]
Susceptibility	1.25 10 ^{−3} [183]	≈ 1 10 ^{−3} [185]	2.8 [183]
Coercive force / kA m ^{−1}	319 [183]	≈ 120 [184]	1.6 [183]
Remanent magnetization / kA m ^{−1}	1.0 [183]	1.1 [184]	5.0 [183]

coercivity is a measure of the external magnetic field necessary to demagnetize it [182]. Finally, the remanent magnetization is the residual magnetization conserved by a material after an external magnetic field is removed [182].

Hematite shows a weak ferromagnetism at temperatures below 956 K (T_c) [11]. Fe³⁺ cations are antiferromagnetically coupled across the shared octahedral faces along the c-axis (Fig. 1) forming two interpenetrating antiferromagnetic sublattices. However, these sublattices are not exactly antiparallel and due to this phenomenon called spin canting, hematite shows a weakly ferromagnetic behavior [11]. Spin canting is more pronounced in nanostructures smaller than about 8 nm where the surface contributions are predominant [11]. In the goethite structure, the spins are oriented along the b-axis (Fig. 9) with parallel and antiparallel directions in alternate chains of the FeO₃(HO)₃ octahedron [11]. Thus, goethite shows an antiferromagnetic order at room temperature. Unlike hematite and goethite, magnetite is ferrimagnetic at room temperature. In the magnetite crystal structure, Fe²⁺ cations are located in octahedral sites and Fe³⁺ cations are located in both octahedral and tetrahedral sites. Although the spins of the FeO₄ tetrahedrons and the FeO₆ octahedrons are antiparallel, their magnitudes are unequal [11]. This difference is the reason for the observed ferrimagnetism [11].

Photocatalysts are often combined with magnetic materials to improve their separation from the suspension, thus facilitating the recovery process [186,187]. Ferromagnetic semiconductors, such as ferrites, are also combined with non-magnetic photocatalysts to form composites that show higher photocatalytic activities than the bare materials. This enhancement is attributed to the heterojunction formation, which facilitates the charge-carrier separation. In such cases, the ferrite contributes to both, the recovery process and the improvement in the photocatalytic efficiency [188,189]. A proper band alignment between the materials forming a heterojunction is crucial in order to promote the charge separation rather than the charge recombination [190]. However, it is still not clear if the magnetic properties have a positive or negative impact in the photocatalytic activity. The first report on the effect of magnetic fields on heterogeneous photocatalysis was made by J. Kiwi in 1983 [191]. Since then, some other researchers have dedicated their efforts to investigate this effect [192]. However, skepticism arose in the scientific community mainly due to the difficulty in reproducing the results [193]. Kiwi reported that external magnetic fields vary the fraction of radical species that interact with heterogeneous catalysts. He showed a reduction in the photocatalytic H₂ production rate of Pt/TiO₂/RuO₂ under the influence of a 0.4 T external magnetic field. However, contradictory results are found in the literature. Wakasa et al. [194] reported a magnetically induced acceleration of the decomposition reaction of tert-butyl alcohol in the presence of TiO₂ under UV irradiation. They ascribed this effect to a decrease in the electron-hole recombination rate induced by the magnetic field [194]. For a deeper insight into the magnetic field effect in TiO₂ heterogeneous photocatalysis, the reader is referred to references [193] and [192]. The reported effects of external magnetic fields on the TiO₂ photocatalytic activity might be extended to other materials. However, the effect of the intrinsic magnetic field of ferrimagnetic materials such as magnetite is still unknown. In the case of photocatalytic microbial

decontamination, the scientific literature is also controversial. Several reports suggest that static magnetic fields (SMFs) do not affect or show extremely small effects on microorganism growth rates [195]. However, negative influences of SMFs in the growth of wastewater bacteria (*Escherichia coli* and *Pseudomonas putida*) are also reported [196]. The absence of a comprehensive view regarding the effect of SMFs lies in the fact that the reported investigations are usually vary in the strength and exposure time of the magnetic field or the chemical environment [195,196] which makes qualitative analysis not an easy task.

8. The synthesis methods of iron oxide photocatalysts

A variety of methods were found to be suitable for the synthesis of α-Fe₂O₃, γ-Fe₂O₃ and Fe₃O₄ with different physiochemical properties. It is well understood that photocatalytic properties are largely dependent on the morphology, particle size and specific surface area [197]. In addition, the synthetic route plays an important role in the photocatalytic efficiencies of such photocatalysts by influencing the behavior of iron oxides under irradiation. However, controlling size, shape, stability, and dispersibility of iron oxide NPs in solutions is still a challenge [198].

Recently, various morphologies synthesized through nanostructuring techniques have demonstrated an enhanced catalytic performance due to their chemical and electronic properties. Zero-dimensional (0D) nanocrystals (particles) encounter high recombination rate of photo-generated charge carriers [199]. One-dimensional (1D) nanocrystals (rods, wires, tubes, and belts) restrict electron flow in radial direction through guiding the movement of electrons via axial direction [198]. Two-dimensional (2D) nanocrystals (disks, platelets, sheets and films) providing many reactive reactive sites and enhanced charge behavior properties on its large surface [199]. On the other hand, three-dimensional (3D) nanocrystals (dendrites, flowers, cubes, sea-urchin-like and spheres) with their large surface area and pore channels provide high mass transfer rate of the reactants and products [197].

8.1. Co-precipitation method

The co-precipitation of Fe²⁺ and Fe³⁺ ions at a molar ratio of 1:2 in highly basic aqueous solution is considered as the most common method to synthesize either Fe₃O₄ or γ-Fe₂O₃ [200]. It is recommended to perform this reaction in oxygen-free conditions to avoid the oxidation of Fe²⁺ [200]. The nanoparticles synthesized by co-precipitation method are characterized by their poor shape control with a broad size distribution and poor dispersion. With no need for special stabilizing agent, co-precipitation is simple and low-cost method to obtain large quantity of water-soluble NPs, which is promising for environmental and medical applications [201]. However, it is difficult to avoid nucleation during reaction and the obtained particles have a weak magnetic response. In addition, a size selection procedure after co-precipitation is generally needed [202].

Table 3
Examples of the use of hematite-based photocatalysts for the de-coloration of dyes.

Material	Application	Main results	Remarks	Ref.
Mesoporous α -Fe ₂ O ₃ (soft chemistry and hard template methods)	Photocatalytic degradation of azo dye orange II using 11 W LED lamps ($\lambda = 400$ –700 nm)	\approx 20 times higher reaction rate for the α -Fe ₂ O ₃ sample prepared by soft chemistry	Synthetic method is a key factor affecting the photocatalytic activity	[209]
Hollow and mesoporous iodine doped α -Fe ₂ O ₃ (sol-gel method)	Photocatalytic degradation of methylene blue using a visible and UV radiation	1 % mole iodine doped α -Fe ₂ O ₃ showed \approx 98 % photodegradation after 45 min	Activity is affected by the surface absorption properties. Insertion of iodine reduces the band gap of α -Fe ₂ O ₃ and enhances the photocatalytic performance	[210]
Ring-like α -Fe ₂ O ₃ assembly (top-down etching method)	Photocatalytic degradation of Rhodamine B with H ₂ O ₂ using a 500 W xenon lamp with a 420 nm cutoff filter	72.3 % photodegradation after 4 h was reported	Ring-like assemblies show a higher photocatalytic activity than α -Fe ₂ O ₃ nanorings due to the larger specific surface area	[211]
Porous Fe ₂ O ₃ nanorods (chemical solution method with subsequent calcination	Photocatalytic degradation of rhodamine B, methylene blue, methyl orange, and eosin B using a 500 W Xe lamp	97% de-coloration after 270 min was reported	Large surface area, porous nanostructure, and superior stability and reusability of this material	[212]

8.2. Thermal decomposition

The thermal decomposition of organic-iron precursors in high-boiling organic solvent in the presence of surfactant stabilizer has been proven to be a promising synthetic route for preparing high quality iron oxide NPs and in particular single phase Fe₃O₄ NPs which are difficult to obtain [203]. The nanoparticles synthesized by thermal decomposition method are characterized by their very good shape control, high crystallinity and dispersity with a narrow size distribution (5–30 nm). Size control is achieved by separating the nucleation and growth steps, through ramping temperature during synthesis [204]. However, high reaction temperature and toxic reagents are used hence, the possible emission of toxic gases [198]. The particles obtained are usually insoluble in water, thus they need to be modified to render them suitable for environmental applications.

8.3. Solvothermal procedure

The reactions in the organic solvent-based solvothermal process are conducted in the presence of an organic solvent in a closed system at a temperature higher than the boiling point of the solvent. A surfactant can be also used as a capping agent to avoid the agglomeration of nanocrystals [203]. On the other hand, polyol-based solvothermal process includes the usage of high-boiling polyols could serve as reducing agents to produce metal particles as well as capping agents to control the particles growth and morphology [205]. The nanoparticles synthesized by these methods are characterized by their good shape control, good crystallinity and high dispersion with a narrow size distribution. They show also hydrophilic properties and therefore good dispersity in aqueous solution. Although the easy scaling-up of these methods, the relatively slow kinetic and sensitivity to the concentration of water and alkalinity [198] are the main drawbacks of these techniques.

8.4. Hydrothermal procedure

It is a specific solvothermal process where water is employed as a dispersion medium rather than organic solvent to enhance the dissolution of iron precursors. The addition of organic or inorganic dispersant is usually preferred [198]. The nanoparticles synthesized by hydrothermal method are characterized by their very good shape control, high degree of crystallinity and high dispersion with a very narrow size distribution. Although the relatively slow kinetic of this procedure, using less amounts of organic reagents with relatively cost-effective and high yield of products are the main advantages of this technique.

8.5. Microemulsion process

The nanoparticles are formed when mixing two water-in-oil microemulsions, where one contains a salt or a complex of metal, while the other contains a precipitating agent. Various morphologies are possibly obtained by controlling the preparation conditions [206]. Shape- and size-controlled iron oxide NPs could be obtained without additional size-selection process. Unfortunately, large amount of solvent should be used to synthesize appreciable quantities of nanomaterials.

9. An overview of the different photocatalytic applications of iron-based nanostructures

Hematite, iron oxy-hydroxide, Fe-doped TiO₂, iron-based pervoskites and spinel ferrites have been tested as photocatalysts for possible applications in photocatalytic wastewater treatment. Most experimental work has been performed with dyes as probe molecules. Although many researchers have reported photocatalytic decomposition of dyes, there is a significant problem in the photocatalytic activity

test, which is the inadequacy of dyes (such as methylene blue) for semiconductor photocatalysis. The photoinduced reaction by methylene blue photoabsorption may mislead into believing that a given semiconductor material has visible-light photocatalytic activity [207]. Hence, the use of transparent molecules in the region of working wavelengths is strongly recommended in a photocatalytic activity test to judge whether it is a *real* photocatalytic activity.

9.1. Photocatalytic oxidation applications

As mentioned earlier, hematite has been reported as an efficient photocatalyst for the de-coloration of dyes under visible light irradiation (see Table 3) [208]. However, little work has been done to investigate its activity towards the photocatalytic degradation of organic pollutants.

Kormann et al. [213] compared the photocatalytic activity of α -Fe₂O₃ colloid to that of ZnO and TiO₂ for the degradation of chlorinated hydrocarbon molecules. Interestingly, they found that α -Fe₂O₃ appears to react only with a selected set of molecules (i.e., with strong reducing agents like sulfite, oxalate and iodide). In addition, Fe₂O₃ was non-active at all for molecules such as chloroform, chloroacetic acid, and chloral. The lack of activity cannot be due to the redox potential of the valence band, because its oxidation potential is sufficiently positive, i.e. E_{vb} = +2.5 V (at pH 2), to oxidize water yielding ·OH radicals (E° = 2.47 V) [214]. The authors assumed that the photogenerated holes could be formed in deep traps, which negatively affect the activity.

The degradation of organic compounds has also been investigated on Fe-modified TiO₂. Franch et al. [215] have found that the adsorption of Fe(III) on TiO₂ increases the efficiency of the mineralization of maleic acid compared to bare TiO₂. They have reported that in TiO₂ + UV assays, malic, acrylic, malonic, oxalic, acetic and formic acid have been detected, whereas in the case of TiO₂/Fe + UV systems, malonic and formic acid are the only detected degradation intermediates of maleic acid. According to the authors, the adsorbed Fe(III) creates new acidic sites on the surface of TiO₂, which would increase the oxygen adsorption leading to higher yields of those pathways that need O₂ or O₂[−] participation. They discussed also the photoactivity of Fe–maleic acid complexes, where maleic acid could be oxidized by means of ligand to metal charge transfer (LMCT) to the adsorbed Fe(III), leading to the formation of the same carbon-centred radical that is formed through the photo-Kolbe process. Yu et al. [216] prepared a TiO₂-based visible-light photocatalyst, in which Fe(III) species are grafted on a rutile TiO₂ surface as an amorphous FeO(OH)-like structure. Fe(III)/TiO₂ showed an optical absorption in the visible light range over 400 nm, which is assigned to the interfacial charge transfer from the valence band of TiO₂ to the surface Fe(III) species. A high quantum efficiency (QE) of 22% for the decomposition of gaseous 2-propanol was reported under visible light irradiation (400–530 nm). The authors explained the higher activity of Fe(III)/TiO₂ compared to TiO₂ by photoproduced holes that are generated in the valence band of TiO₂ and contribute to the oxidative decomposition of 2-propanol, and the catalytic reduction of oxygen by photoproduced Fe(II) species on TiO₂. Lezner et al. [217] prepared an iron-modified TiO₂ by a sol-gel method and surface modification method, followed by calcination at 400 °C. The authors have investigated the photocatalytic activity of thus powders by the degradation of phenol in an aqueous solution. A degradation efficiency up to 61% of phenol was achieved after 60 min under visible light irradiation using Fe_(0.5%)-doped TiO₂ sample. They have found that the BET surface area decreases with increasing iron concentration, while the higher the concentration of iron the stronger the absorption in the visible range.

Iron oxy-hydroxides are promising photocatalysts especially for the degradation of organic pollutants. Li et al. [218] prepared α -FeOOH, also known as goethite, nanorods with diameters in the range 50–100 nm and over 1 μ m in length through a hydrothermal method. They attributed the origin of the 1D structure of α -FeOOH to the

anisotropic growth characteristics of the crystals. The photocatalytic properties of these nanorods were evaluated by decomposing methyl orange in water under UV-vis illumination in the presence of H₂O₂. The authors explained the activity of goethite by the specific outer facets and the high surface-to-volume ratio of the nanorods. Yang et al. [219] have used an *in-situ* precipitation method to prepare ultrafine amorphous FeOOH/ultrathin-g-C₃N₄ nanosheets heterojunction composites. The photocatalytic activities were evaluated using rhodamine B, methylene blue, and methyl orange as model organic pollutants under a 500 W Xe lamp equipped with a cutoff filter ($\lambda \geq 420$ nm). The α -FeOOH/g-C₃N₄ composite exhibited higher photocatalytic activities than both, α -FeOOH and g-C₃N₄. The authors reported ~95% of dye discoloration with ~55% TOC removal within 240 min using the α -FeOOH/g-C₃N₄ composite compared to ~20% of dye discoloration using g-C₃N₄. They attributed this photocatalytic activity to the narrower band gap, the enhanced visible light absorbance of FeOOH, and the effective separation of the photogenerated charge carriers. Zhu et al. [220] synthesized hierarchical heterostructures of β -FeOOH on electrospun TiO₂ nanofibers by a hydrothermal method. They have reported different types of FeOOH nanostructures such as 0D particles, 1D needles and 2D flakes and nanocables by varying the concentration of FeCl₃. The TiO₂@FeOOH nanocables exhibited surface areas ranging from 21–67 $\text{m}^2 \text{g}^{-1}$ and were capable of discoloring methyl orange in 80 min under a 300 W Xenon arc lamp of intensity 100 mW cm^{-2} equipped with a cutoff filter ($\lambda \geq 420$ nm) in the presence of hydrogen peroxide solution. Moreover, Abdinoor et al. [68] have synthesized four different polymorphs of nanostructured iron oxyhydroxides, namely; goethite (α -FeOOH), akaganeite (β -FeOOH), lepidocrocite (γ -FeOOH), and feroxyhyte (δ -FeOOH). They examined their photocatalytic properties by the photocatalytic discoloring of methylene blue under a 300 W Xenon arc lamp at an intensity of 100 mW cm^{-2} equipped with AM 1.5 cut-off filter. Feroxyhyte exhibited the best photocatalytic properties and discolored 85% of the methylene blue dye in five hours. In comparison, goethite, akaganeite, and lepidocrocite discolored only 40%, 35%, and 30%, respectively. The authors explained the enhanced activity of feroxyhyte to its larger surface area and its slightly smaller electronic band gap compared to the other FeOOH polymorphs.

The adsorption of zero-valent iron (ZVI) on the surface of photocatalytic semiconductor has been investigated. It is proven to be a good strategy to enhance the photocatalytic activity plus acquiring magnetic properties. Liang et al. [221] have reported on the immobilisation of ZVI on the surface of graphitic carbon nitride (g-C₃N₄) nanosheets by a borohydride-reduction method results in an enhancement of the photocatalytic activity compared to pure g-C₃N₄. The as prepared nano-hybrid material showed a photodegradation of 99.9% of rhodamine B (Fig. 19a and c) and simultaneous reduction of 92.9% of Cr(VI) ions (Fig. 19b and c) under visible light irradiation. The authors attributed these enhanced activities to the Fe[°], which improves the charge separation efficiency of g-C₃N₄ and lowers the recombination rate of the photogenerated charge carrier, as illustrated in Fig. 19d. Petala et al. [222] observed a photocatalytic activity for the removal of Cr(VI) under UV-C irradiation using a magnetic photocatalyst composed of ZVI homogeneously distributed over a mesoporous TiO₂. They attributed this activity to the synergistic effect between the two components. The authors have reported an important contribution of porous TiO₂ matrix by providing the host surface area and serving as an electron donor that can secure the reuse of the composite photocatalyst in consecutive cycles.

On the other hand, photocatalytic activity of BFO nanoparticles towards the de-coloration of dyes and the degradation of organic pollutants was also investigated by many workers. Gao et. al. [223] synthesized BFO nanoparticles of size ranging from 80 nm to 120 nm using a sol-gel method. BFO showed 90% photocatalytic degradation of methyl orange after UV-vis irradiation for 8 h. In case of bulk BFO, 70% of methyl orange was degraded after 16 h. However, using UV light, 90% was degraded after 16 h. Shun Li et. al. [130] prepared BFO microcrystals with various morphologies by a controlled hydrothermal

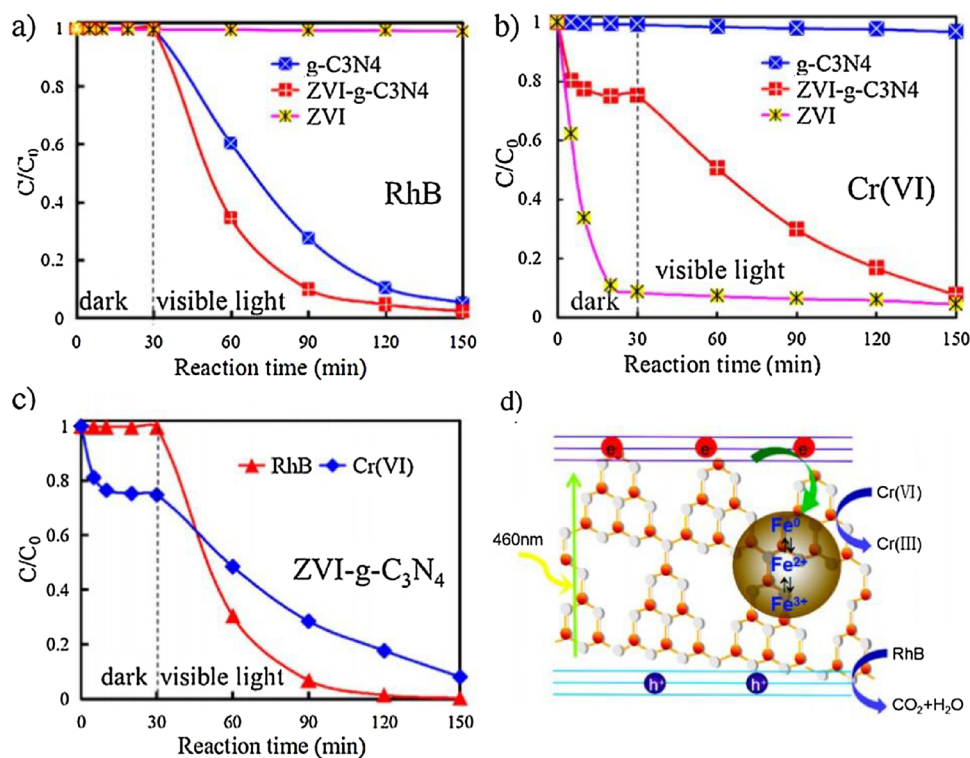


Fig. 19. Photocatalytic activity of a) RhB, b) Cr(VI) by $\text{g-C}_3\text{N}_4$, ZVI- $\text{g-C}_3\text{N}_4$ and ZVI and c) mixture of RhB and Cr (VI); d) the proposed photocatalytic mechanism. Adapted with permission from reference [221].

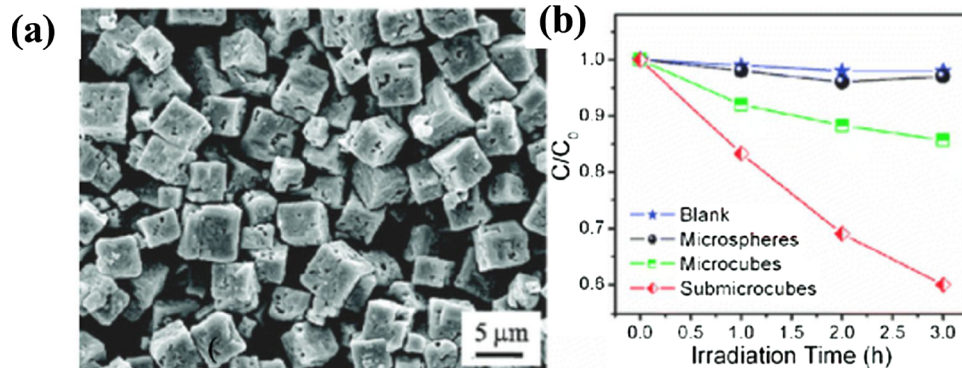


Fig. 20. (a) SEM images of BiFeO_3 submicron cubes. (b) The photodegradation efficiencies of CR as a function of irradiation time under visible-light by different BiFeO_3 specimens. Reproduce with permission from reference [130].

method in a strong alkaline medium. The photocatalytic activities were evaluated by the degradation of congo red in aqueous solution under visible-light irradiation. BFO microsphere did not show any activity in the degradation of organic compound due to its large size. Meanwhile, the microcubes showed weak photocatalytic performance under the same condition. However, with BFO submicron cubes, 40% of the congo red was decolorized after 3 h, demonstrating reasonable ability of BFO towards photocatalytic dye degradation. Fig. 20a shows the SEM images of BFO submicron cubes and Fig. 20b shows the photodegradation of CR using the different crystals morphologies and sizes.

Papadas et al. [136] observed much enhanced photocatalytic performance and stability after modifying the BiFeO_3 surface with gold nanoparticles. They used mesoporous SBA-15 silica and mesoporous CMK-3 carbon to produce pores. The photocatalytic oxygen evolution reactions were carried out using a 300 W xenon lamp with an optical cut-off filter ($\lambda > 380$ nm) and an alkaline solution of NaOH and $\text{Na}_2\text{S}_2\text{O}_8$ was used as electron acceptor. They reported oxygen evolution rate of $\sim 66 \mu\text{mol h}^{-1} \text{g}^{-1}$ for the mesoporous BFO. This OER activity

represents is 3-fold improvement compared to that of its bulky counterpart ($\sim 24 \text{ mmol h}^{-1} \text{g}^{-1}$). The surface modification with Au showed 8 times increase in the OER when compared to BFO mesostructured without Au. Au nanoparticles on the BiFeO_3 surface can substantially reduce the electron-hole recombination due to the interfacial electron transport at the Au/ BiFeO_3 junctions, thus enhancing the photocatalytic performance, Fig. 21a. Most significant thing is that the amount of oxygen evolved increased almost linearly with time, demonstrating that the present catalyst maintains a strong driving force for water oxidation over the examined period, Fig. 21b.

Jia Lishan et al. [224] reported on the visible light photocatalytic performance of $\text{SrFeO}_{3-\delta}$ towards phenol degradation. $\text{SrFeO}_{3-\delta}$ nanoparticles with size ranging from 70 nm to 100 nm were prepared from nitrate precursors via ultrasonication and calcined at 800 °C. The sonicated precursor showed 38.65% degradation after illumination for 4 h compared to 22.97% for nanoparticles prepared without sonication. Lin et al. [225] reported an enhanced photocatalytic activity of the heterojunction $\text{SrFeO}_{3-\delta}/\text{g-C}_3\text{N}_4$ towards degradation of chloramphenicol

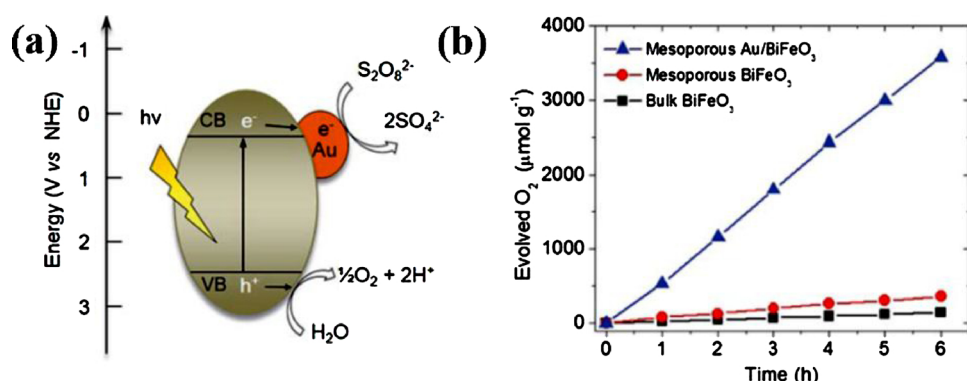


Fig. 21. (a) Schematic diagram showing the possible pathway for O₂ evolution by BFO/Au heterojunction. Reproduced with permission from reference. (b) Oxygen evolution profiles. Reproduced with permission from reference [136].

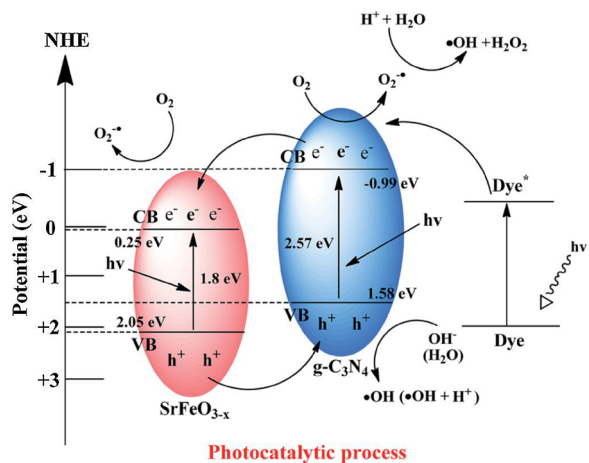


Fig. 22. Band structure diagram of SrFeO_{3-x}/g-C₃N₄. Reproduced with permission from reference [225].

(CAP) antibiotic. g-C₃N₄ was fabricated from melamine, SrFeO_{3-x} was fabricated employing sintering method with Fe₂O₃ and SrCO₃ at 1000 °C, and the heterojunctions of SrFeO_{3-x}/g-C₃N₄ were synthesized by sintering SrFeO_{3-x} with g-C₃N₄ at 400–600 °C. They found that the composite shows much higher photocatalytic activity than the component phase alone such that 91% of CAP was degraded by SrFeO_{3-x} in 96 h. This time was reduced to 24 h after forming a heterojunction with 4 wt % g-C₃N₄. The band position of both components is shown in Fig. 22. The position of CB and VB of the semiconductor g-C₃N₄ is higher than that of SrFeO_{3-x}. The photoinduced electrons on the g-C₃N₄

surface can easily transfer to SrFeO_{3-x} via the interfaces, while the holes on the SrFeO_{3-x} surface can migrate to g-C₃N₄ in a similar manner. The charge transfer effectively retards the recombination of electron–hole pairs in the two semiconductors. O₂^{·-} and OH[·] are the main and h⁺ is the minor active species in the whole process.

Spinel ferrite nanoparticles are also very attractive materials for the photocatalytic de-coloration and degradation of organic pollutants due to their nontoxicity, ease of synthesis and availability of the precursors [226,227]. Sun et al. [228] reported around 95% photocatalytic degradation of rhodamine B over a cubic ZnFe₂O₄ with spinel structure under visible light irradiation. The authors have attributed such activity to the impurities α-Fe₂O₃ and ZnO in the sample, which promote the separation of photo-generated electrons and holes. However, many researchers have combined spinel ferrites with other semiconductors such as TiO₂ [229], ZnO [230] and reduced graphene oxide (rGO) [231], in order to inhibit the recombination of charge carrier in ferrites. Zheng et al. [232] have reported that coating a TiO₂ layer on the surface of Fe₃O₄ results in a highly efficient magnetic photocatalyst for the degradation of monocrotophos insecticide under UV irradiation. The prepared nano-composite showed a complete degradation of monocrotophos with 71% reduction in TOC after 45 min of UV illumination, indicating the existence of intermediates. Fu et al. [233] prepared a combined CoFe₂O₄-graphene photocatalyst to produce an active photocatalyst for the degradation of several dyes under visible-light irradiation. The authors have explained the higher activity of this composite by the ease electron transfer from the CoFe₂O₄ conduction band to the reduced graphene oxide preventing the recombination of electrons and holes as shown in Fig. 23.

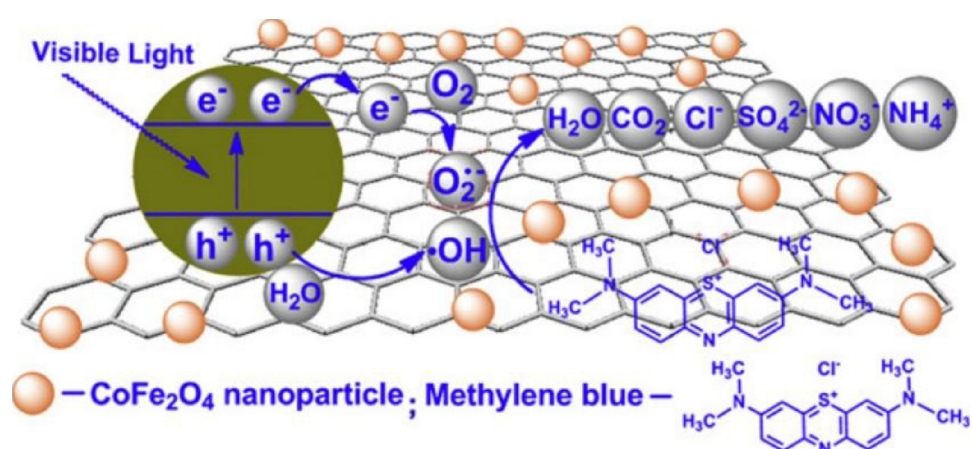
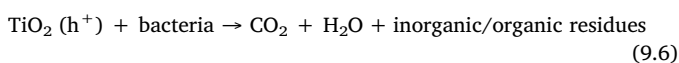
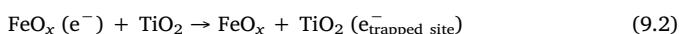
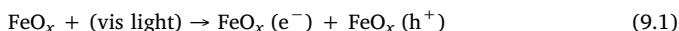


Fig. 23. Proposed mechanism of photocatalytic activity enhancement of CoFe₂O₄-graphene photocatalyst. Reproduced with permission from reference [233].

9.2. Anti-bacterial activities

Iron oxide NPs have been reported as efficient photocatalysts for antibacterial applications. [234]. Several studies have shown that the generation of reactive oxygen species (ROS) is the main mechanism of the antibacterial activity by iron-based materials [235]. Iron oxide NPs have been applied for the inactivation of *Staphylococcus aureus* [236,237] and *Escherichia coli* [237,238]. Iron(III) doped TiO_2 thin films [239,240], Ag-TiO₂ nanotubes modified with FeO_x magnetic oxide [241], nano-sized Fe₂O₃ powder, Fe₃O₄@TiO₂ core–shell nanoparticles [242] and FeO_x–TiO₂–PE [243] photocatalysts have shown very good activity in this area. Rtimi et al. have reported that a combination between FeO_x and TiO₂ leads to a bacterial inactivation through the following proposed mechanism (Eqs. (9.1)–(9.6)) [243]. They ascribed this activity to the photosensitizing effect of FeO_x under visible light irradiation and the charge transfer to TiO₂, where electron trapping at 150 fs was observed to compete with electron–hole recombination.



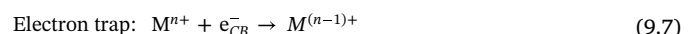
FeO_x–polyethylene transparent films were synthesized by Rtimi et al. [244] and acted efficiently to inactivate the *Escherichia coli*. The authors have reported a slight hindrance of bacterial inactivation upon scavenging ·OH radicals with DMSO, while a complete suppression of the bacterial inactivation was noticed due to the scavenging of photo-generated holes by EDTA-2Na. Moreover, no bacterial inactivation was observed in anaerobic conditions, suggesting that the oxidative radicals are generated only under aerobic conditions. Interestingly, the Fe-oxidation states of PE–FeOx were changed dramatically after the bacterial inactivation. The content of Fe(III)/Fe₂O₃ decreases from ~80.0% at time zero to ~53.0% with a concomitant increase in Fe₃O₄ and Fe(II)/FeO. Fig. 24 shows the effect of scavengers (Fig. 24a) and the reaction conditions (Fig. 24b) on the photocatalytic antibacterial activity. Fig. 24c suggests also a mechanism for the bacterial inactivation on PE–FeOx, which includes an electrostatic attraction of the negatively charged *Escherichia coli* at pH between 3 and 9 on the slightly positively charged PE–FeOx. Fe₂O₃ presents a CB at +0.1 eV and a VB at +2.2 eV, hence the holes interact with the adsorbed –OH surface groups but do not have enough potential to lead to the formation of ·OH radicals.

Spinel ferrite nanoparticles have been investigated as photocatalysts for antibacterial applications. The cytotoxicity effects of ferrites are related to the presence of different oxidation state of iron in these materials [245]. On the other hand, Biswas et al. [246] synthesized bismuth ferrite (BFO) nanorods fabricated on porous anodized alumina (AAO) templates. Thus BFO nanorods exhibited an enhanced polarization and significant magnetic susceptibility. The authors have reported that the asymmetric structure of the BFO nanorods give rise to augmented antibacterial response against *Staphylococcus aureus*. They found a significant peak shift upon interaction with bacterial cells in the XPS data, which indicates a change in Bi oxidation states. The authors have shown that the shifting behavior is possibly related to a redox reaction that takes place at the BFO nanorod–bacterial interface, which is ascertained for bacterial inactivation. Sanpo et al. [247,248] have reported that transition metal–substituted spinel ferrite enhances the antibacterial property of nanoparticles. The substitution of zinc and copper in cobalt ferrite nanoparticles significantly improves antibacterial activity against *Escherichia coli* and *Staphylococcus aureus* [249] as shown in Fig. 25. Xu et al. [250] have reported in a recent

study that ZnFe₂O₄/AgI composite exhibits a photocatalytic activity for the inactivation of bacteria under visible light irradiation. The authors attributed this efficiency to the introduction of 5% ZnFe₂O₄, which enhances the light harvesting and improves the separation efficiency of photogenerated charge carriers as illustrated in Fig. 26. Such effects lead to 100% removal of *Escherichia coli* in 80 min. They have also identified H₂O₂ as predominant active species in the photocatalytic inactivation of bacteria.

9.3. Photocatalytic hydrogen evolution

Another important application for iron-based photocatalysts which attracts an increasing attention recently is the photocatalytic hydrogen evolution. Several works have reported the activity of Fe-modified TiO₂ as photocatalysts for the photocatalytic hydrogen evolution. Unfortunately, although the earth-abundant hematite (α -Fe₂O₃) is a promising material from the viewpoint of the band gap energy, however its conduction band is too low to drive the reaction of hydrogen evolution [251,252]. The position of its conduction band edge (~0.2 eV vs. NHE) only allows the formation of molecular hydrogen if an external bias is applied [253]. On the other hand, core–shell based-photocatalysts have been widely studied in the field of photocatalytic hydrogen generation. Among all the core–shell structures, Fe₃O₄ based-core–shell photocatalysts have been explored, because Fe₃O₄ has the highest magnetization, ~90 emu/g, compared to the other iron oxides, which aids with the magnetic separation of the nanocomposite from the aqueous medium [254]. Magnetic Fe₃O₄ core not only contributes to the separable photocatalysts, but also act as an electron acceptor hindering the recombination of the photogenerated charge carriers [255]. Moreover, α -Fe₂O₃ and γ -Fe₂O₃ cores with high saturation magnetization were reported to help the photocatalyst separation [255]. Dholam et al. [256] synthesized Fe-doped TiO₂ thin films on ITO by two techniques; radio-frequency magnetron sputtering and a sol–gel method. They showed that the Fe-doped-TiO₂ obtained by sputtering has a red shift of the absorption edge in the visible light range more than that obtained by the sol–gel technique. They have inferred also that metal doping of TiO₂ by sputtering narrows the band gap because Fe ions have enough energy to displace Ti ions in TiO₂ lattice leading to the transfer of Fe-3d electrons to the conduction band of that narrowing the band gap. In contrast, the sol–gel metal doping only forms impurity energy levels into the band gap. The authors reported a H₂ production rate of 15.5 $\mu\text{mol h}^{-1}$ in visible light due to the ability of Fe ions to trap both electrons and holes avoiding recombination as per Eqs. (9.7) and (9.8). On the other hand, Madhumitha et al. [257] have improved the photocatalytic hydrogen evolution by using a magnetically separable core shell nano photocatalyst TiO₂/Fe₂O₃, prepared by co-precipitation method. They reported a maximum hydrogen rate of 2700 $\mu\text{mol h}^{-1}$ and a quantum yield of 3.86% at 550 nm when EDTA was used as a sacrificial reagent. Effective charge transfer from TiO₂ to Fe₂O₃ and the suppression of e[–]/h⁺ pair recombination attributed significant enhancement in photoactivity, thereby increasing the hydrogen production. The authors described the mechanism as shown in Fig. 27, where the core of Fe₂O₃ is acting as a sink for photogenerated electrons after the irradiation with visible light in the presence of water and sacrificial reagents. The excited electrons of the TiO₂ shell transfer then into the CB of the Fe₂O₃ magnetic core, making the interfacial contact close between TiO₂ and Fe₂O₃ and reducing protons to hydrogen. They have also attributed the better efficiency to the higher visible light harvesting capacities of the core–shell particles than bare TiO₂ and to the interfacial contact between Fe₂O₃ and TiO₂ that enhances the mobility and the charge carrier separation.



Chang and Tsai [258] synthesized magnetically separable

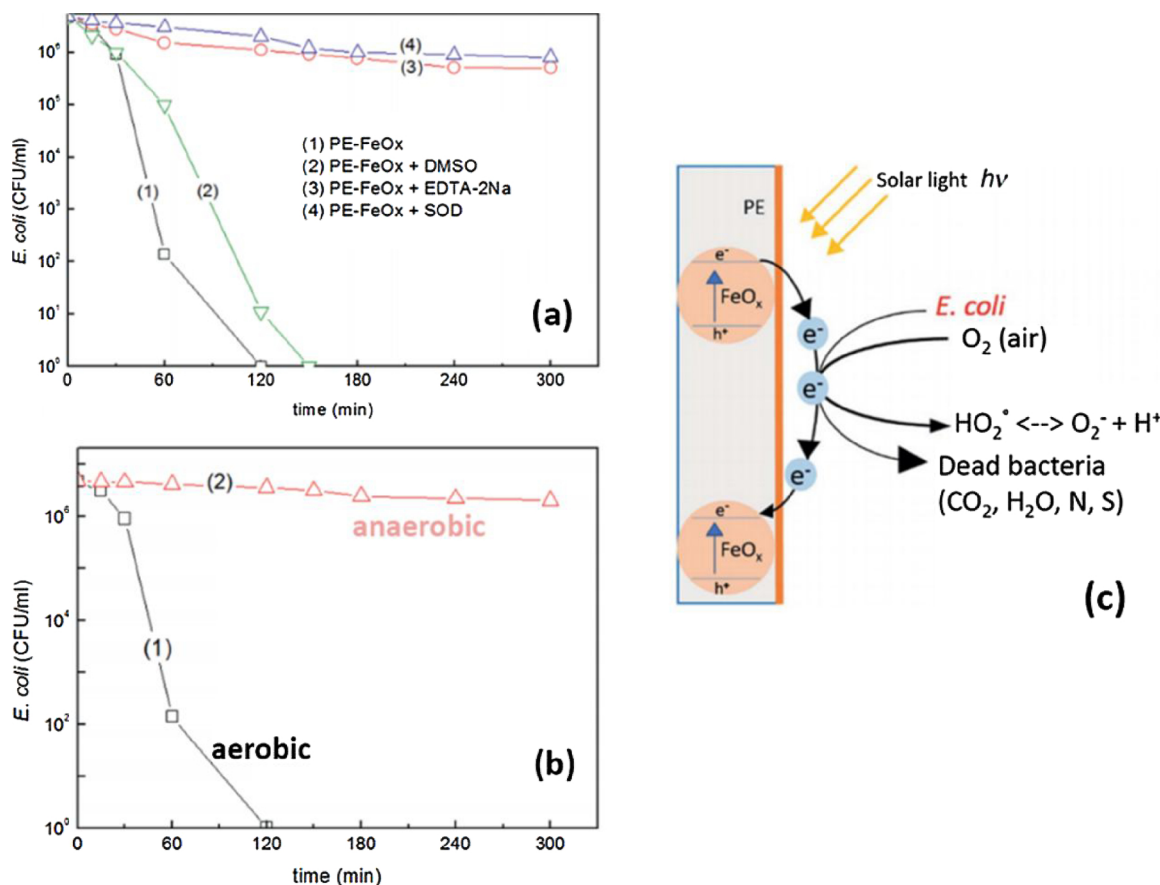


Fig. 24. Bacterial inactivation by PE-FeOx using (a) several radical scavengers, (b) different condition and (c) the proposed mechanism. Adapted with permission from reference [244].

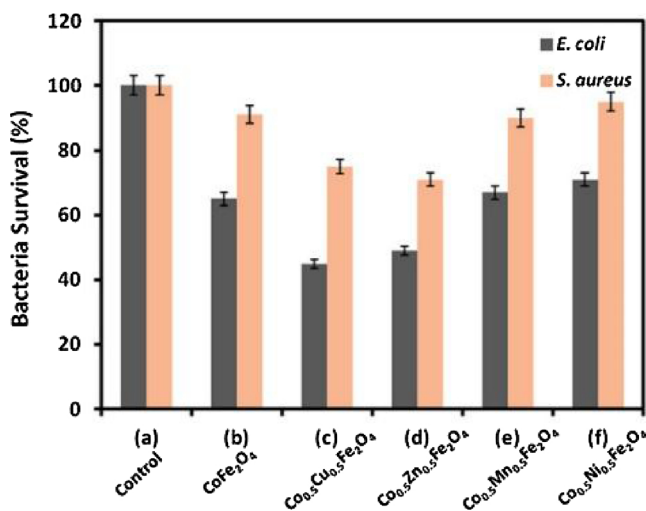


Fig. 25. Antibacterial activities against *Escherichia coli* and *Staphylococcus aureus* of synthesized transition metal-substituted cobalt ferrite nanoparticles. Reproduced with permission from reference [248].

photocatalyst by decorating $\text{Fe}_3\text{O}_4@\text{ZnS}$ core shell by CuS nanoparticles for making the structure with magnetic Fe_3O_4 in the core, with the formation of heterojunction at the interface between ZnS and CuS. They have recorded a photocatalytic H_2 evolution of $18,000 \mu\text{mol g}^{-1} \text{h}^{-1}$ using an aqueous solution contains a mixture of Na_2S , Na_2SO_3 , and NaCl as a sacrificial reagent and a 300 W high-pressure mercury lamp as an irradiation source. The authors attributed this activity to the effective suppression of photoexcited charge carriers recombination, leading

to the enhanced activity of the $\text{Fe}_3\text{O}_4@\text{ZnSeCuS}$ photocatalysts. Upon light irradiation, photoexcited electrons in CB of ZnS can transfer to the Fe_3O_4 and CuS as shown in Fig. 28. Therefore, the transferred electrons in CuS nanoparticles as well as the electrons on ZnS can reduce protons to H_2 . However, the transferred electrons in Fe_3O_4 nanoparticles could not participate in the hydrogen evolution, because the conduction band of Fe_3O_4 is too low to drive the reaction of hydrogen evolution. Hence, the main role of the Fe_3O_4 core is facilitating the magnetic separation of the composite from its suspension. Wang et al. [259] examined the photocatalytic hydrogen evolution over hierarchically structured TiO_2 ball-flowers doped with different Fe contents. The authors found that $\text{Ti} 2\text{p}_{1/2}$ and $2\text{p}_{3/2}$ peaks in XPS were affected by the doping of Fe ions because they shifted to higher binding energies, which may attribute to the diffusion of Fe^{3+} into the TiO_2 lattice and the subsequent formation of $\text{Fe}-\text{O}-\text{Ti}$ bonds. A hydrogen evolution of $697 \mu\text{mol g}^{-1}$ was observed for Fe/TiO_2 (27.6:1), after 4 h of light irradiation with a 300 W Xe lamp, which is five times greater than that for pure TiO_2 . The authors assigned this improvement to the enhancement in the visible-light absorption characteristics and the increase in the number of oxygen vacancies, which act as the reaction sites for water splitting.

Several alkaline earth metal ferrites such as MgFe_2O_4 , CaFe_2O_4 , and BaFe_2O_4 and their composites with other semiconductor nanoparticles have been widely studied as photocatalysts in aqueous suspensions for photocatalytic hydrogen evolution applications [260–262]. The deposition of co-catalysts (e.g. Pt and RuO_2) and the use of sacrificial reagents (e.g. methanol, ethanol, or triethanolamine) are highly recommended to achieve reasonable photocatalytic activities. Hong et al. [263] showed that the mesoporous NiFe_2O_4 nanospheres made by self-assembly associated aerosol spray pyrolysis exhibit a hydrogen evolution rate of $0.09 \mu\text{mol h}^{-1}$ under visible light irradiation (Xe lamp,

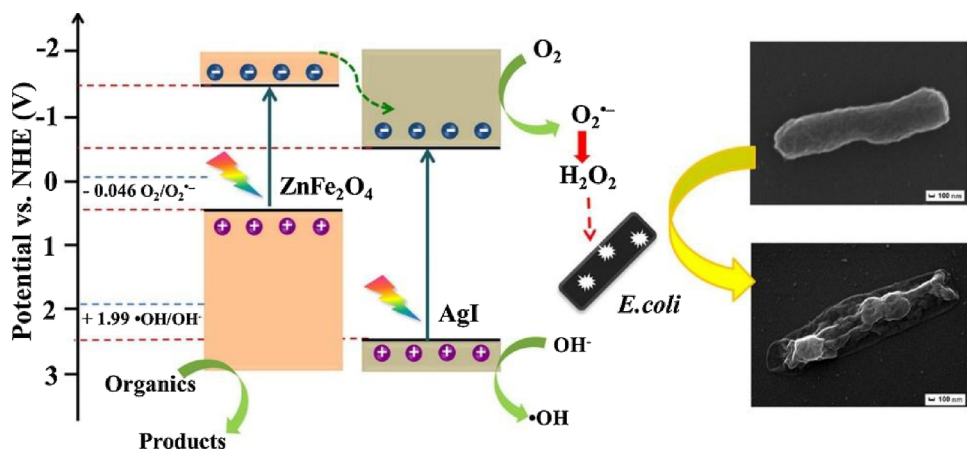


Fig. 26. The mechanism of the photocatalytic disinfection of *Escherichia coli* by $\text{ZnFe}_2\text{O}_4/\text{AgI}$ composites. Reproduced with permission from reference [250].

$\lambda > 420 \text{ nm}$). They explained such activity by its high surface area, wide absorption in the visible light region, and the higher crystallinity. Saadi et al. [264] reported a QY of 1% of H_2 evolution over CuFe_2O_4 using K_2S as a hole scavenger. Dom et al. [265] have used a microwave solid-state synthesis method to prepare a visible light active ZnFe_2O_4 spinel photocatalyst. Using a 300 W solar simulator equipped with an AM1.5 G filter, they reported a maximum H_2 evolution rate of $133.5 \mu\text{mol h}^{-1} \text{ g}^{-1}$ with a quantum yield of 0.19% from water-methanol mixture even in the absence of a co-catalyst. They found that the conduction band edge of ZnFe_2O_4 has a more negative potential than the water reduction level making it a potential photocatalyst for hydrogen evolution. The authors presumed that in the absence of Pt a co-catalyst, the surface states available in the thus prepared photocatalyst would be possibly playing the role of suppression of electron-hole recombination. Song et al. [266] synthesized hollow $\text{ZnFe}_2\text{O}_4/\text{ZnO}$ nanospheres with uniform shell about 10 nm thick. They observed around 7 times higher activity than that of the pure ZnFe_2O_4 as shown in Fig. 29a and b. A quantum efficiency and a hydrogen evolution rate of 1.61% and $2.15 \times 10^3 \mu\text{mol h}^{-1} \text{ g}^{-1}$, respectively were reported using $\text{ZnFe}_2\text{O}_4:\text{ZnO} = (7:3)$. They ascribed such improved activity to the inhibition of charge carrier recombination (see Fig. 29c) due to the band structure alignment and to the relatively shorter diffusion length of the very thin hollow spheres.

9.4. PEC applications

9.4.1. General view on PEC water splitting

The utilization of powdered photocatalysts in the photocatalytic water splitting will produce a mixture of H_2 and O_2 gas in the reactor. The evolved H_2 and O_2 from water is possibly separated using a photoelectrochemical cell based on thin film photoelectrodes [252]. Combining a n-type photoanode and a p-type photocathode in a tandem configuration provides independent optimization of photoelectrodes for water oxidation and reduction reactions [267]. In addition to the overpotential that is required to compensate for recombination, splitting water to O_2 and H_2 requires $237.7 \text{ kJ mol}^{-1}$ under standard conditions [268] and is possibly written as per Eqs. (9.9) and (9.10), respectively [252,267]. Thus, for efficient water splitting reaction, the quasi-Fermi level of holes at the photoanode must be not less than $1.23 + \eta_{\text{OER}}$ (V vs. RHE), while the electron quasi-Fermi level at the photocathode must be at least $-\eta_{\text{HER}}$ (V vs. RHE).



The efficient water splitting PEC cell after a band gap excitation involves three main processes: the diffusion of the photogenerated holes towards the semiconductor surface, the oxidation of water at the

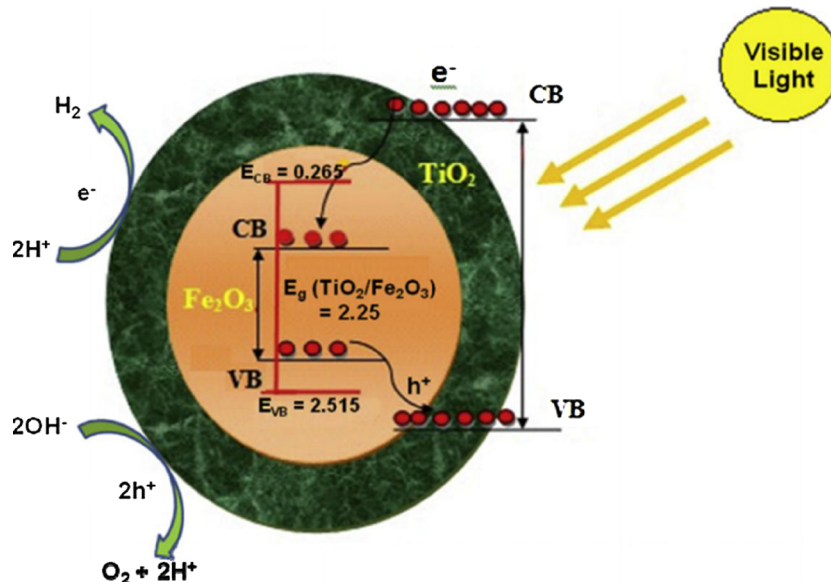


Fig. 27. The mechanism of hydrogen production on magnetically separable core shell $\text{TiO}_2/\text{Fe}_2\text{O}_3$ photocatalyst. Reproduced with permission from reference [257].

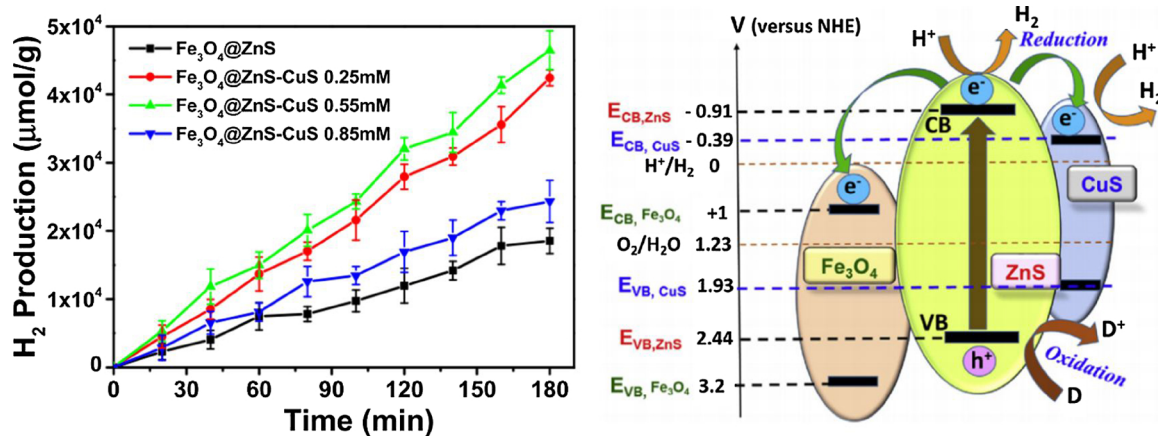


Fig. 28. The mechanism of hydrogen evolution on CuSZNs decorated Fe_3O_4 magnetically separable photocatalysts. Reproduced with permission from reference [258].

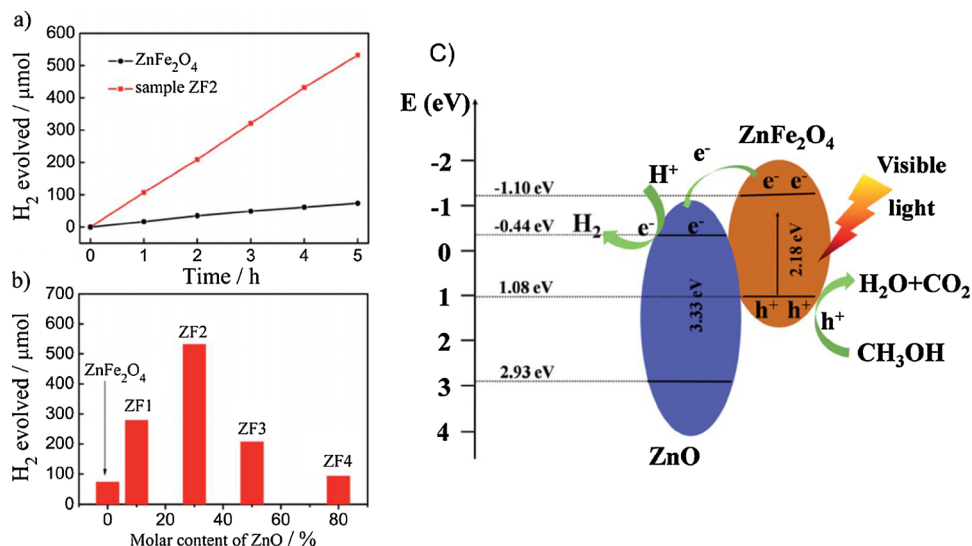


Fig. 29. (a) Hydrogen production under visible light irradiation ($\lambda > 420 \text{ nm}$). (b) Comparison of hydrogen production activities within 5 h. (c) The proposed mechanism. Adapted from ref. [266].

semiconductor-electrolyte interface, and the transfer of the photo-generated electrons to the back contact. In parallel, two undesired processes could take place: the recombination of the photogenerated charge carrier in the bulk, as well as their recombination at surfaces [268,269].

4.4.2. Iron-based photoelectrodes for PEC cell

Many have reported that hydrogen could not be directly generated on hematite electrodes unless a bias voltage is applied. The flat-band potential for polycrystalline hematite ($\alpha\text{-Fe}_2\text{O}_3$) has been determined at pH 10 to be -0.20 V vs. NHE [270]. This value is 0.39 V more positive than the potential required for the hydrogen evolution reaction. In contrast, hematite has a valence band that is excessively positive of H_2O oxidation reaction. With a band gap of 2.1 eV , hematite matches very well the band gap requirement of a photoanode in tandem configuration PEC cell. Fig. 30 represents a schematic for an n-type hematite photoanode. The relatively low specific surface area of hematite provides a higher current density which in turn increases the overpotential [271]. Hence, solar water oxidation photocurrents up to approximately 4 mA cm^{-2} have been achieved for Fe_2O_3 [272,273], which are still very low compared to the theoretical maximum photocurrent of 12 mA cm^{-2} at standard irradiation of 1 sun [274].

Doping hematite with other cations has been reported as a possible

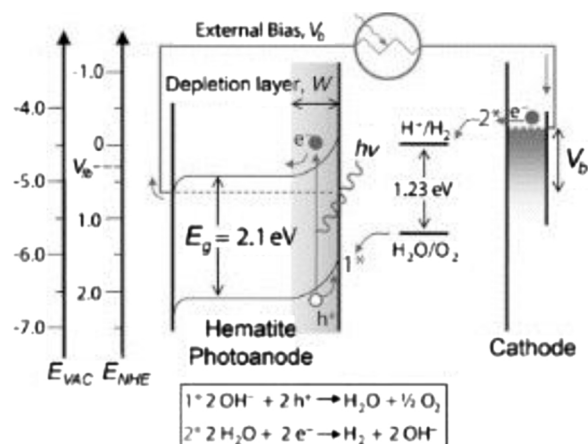


Fig. 30. Energy diagram for photoelectrochemical water splitting with an n-type photoanode (hematite) performing the oxygen evolution reaction and a cathode performing the hydrogen evolution reaction. Reproduced with permission from reference [275].

solution to increase its activity as a photoanode. Malviya et al. [276] prepared Sn, Nb, Si, Pt, Zr, Ti, Zn, Ni and Mn doped α -Fe₂O₃ thin films and used them as photoanodes for PEC solar water splitting using 1 M NaOH electrolyte solution. Sn-doped hematite photoanode achieved the highest photocurrent (~ 1 mA cm⁻²) and the lowest onset potential (~ 1.1 V_{RHE}). They have found that the photoanodes ranked in the following order: Sn > Nb > Si > Pt > Zr > Ti > Zn > Ni > Mn. Coupling hematite with other metal oxide semiconductors has been investigated to improve its performance as a photoanode for water splitting. Sivula et al. [277], reported an improvement in light absorption and increase in the surface area of α -Fe₂O₃ by using a host scaffold of WO₃. They also showed a higher water oxidation by the α -Fe₂O₃/WO₃ electrode because more α -Fe₂O₃ are closer to the hematite/electrolyte interface, allowing the photo-generated holes to transfer to the semiconductor–liquid junction and participate therefore in water oxidation. Tilley et al. [278] have reported a water splitting photocurrent of over 3 mA cm⁻² by hematite and IrO₂-based surface catalysis at an applied potential of +1.23 V vs. RHE under AM 1.5 G 100 mW cm⁻² simulated sunlight conditions. McDonald et al. [279] prepared α -Fe₂O₃/ZnFe₂O₄ composite (1:1) photoanode for water splitting, which produces a photocurrent of about 500 μ A cm⁻² at 0.44 V vs. NHE. This composite electrode showed a significantly enhanced photocurrent response because ZnFe₂O₄ has conduction and valence band edges shifted ca. 200 mV from those of Fe₂O₃ to the negative direction as illustrated in Fig. 31, allowing an efficient separation of electron–hole pairs at the Fe₂O₃/ZnFe₂O₄ interface. They have reported that a higher ratio of ZnFe₂O₄ negatively affects the activity, because it significantly reduces the surface area.

Iron oxy-hydroxides have been also used in PEC applications. Chemelewski et al. [280] synthesized an amorphous FeOOH 10 nm thick film on FTO substrate as an OER catalyst, which showed activity of 10 mA/cm² at an overpotential of ~ 550 mV in 1 M Na₂CO₃. The authors have tested the utility of amorphous FeOOH in a realistic system by depositing on amorphous Si triple junction solar cells. They have achieved a total water splitting efficiency of 4.3% at 0 V vs. RHE in a three-electrode configuration with almost no significant degradation of the film after 4 h of testing. Zhang et al. [281] have used a general gelatin-assisted wet chemistry method to synthesize iron oxy-hydroxides and cobalt-doped iron oxy-hydroxides nanomaterials. Both materials showed good performances especially Co_{0.54}Fe_{0.46}OOH, which exhibited an onset potential of 1.52 V and tafel slope of 47 mV/dec for OER. The authors ascribed the superior OER activity of Co-doped FeOOH to the branch structure on its surface, which provided many active edge sites, enhanced mass/charge transport capability and easy release oxygen gas bubbles.

PEC water splitting using ferrites is possibly classified into two parts: ferrites as photocathodes and photoanodes [165]. The CB position of ferrites is well above 0 V, as illustrated in Fig. 16, which make them theoretically good photocathodes for H₂ evolution reaction. Cao et al. have reported that CaFe₂O₄ thin films on FTO glass substrate in a

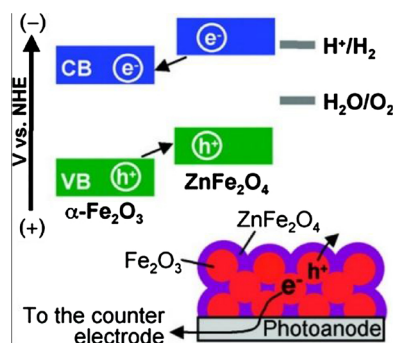


Fig. 31. The mechanism of charge carrier separation in α -Fe₂O₃/ZnFe₂O₄ composite. Reproduced with permission from reference [279].

three-electrode configuration with Pt as counter electrode gives a negative photocurrent of -117 μ A cm⁻² at -0.06 V vs. NHE and a photocurrent of 0.6 μ A cm⁻² at zero bias voltage [213]. Yang et al. observed a small photocurrent of about -0.3 μ A cm⁻² under visible light irradiation when a photocathode of CoFe₂O₄ porous nanosheets on FTO was used without the application of any bias voltage [282]. In addition, Sekizawa et al. recorded a dramatic improvement in the photocurrent to -20 μ A cm⁻² with no applied bias under visible light illumination when using Ag-doped CaFe₂O₄ as a photocathode [283]. The authors ascribed this enhancement to the red shift of photo-absorption and the increase of carrier mobility because of the high symmetry around Fe atom. On the other hand, several ferrites have been used as photoanodes for PEC water splitting. Tahir et al. have reported that thin films of ZnFe₂O₄ on FTO produce a photocurrent density of 350 μ A cm⁻² at 0.44 V vs. NHE with an incident photon to electron conversion efficiency of 13.5% at 350 nm [284]. They attributed this efficiency to the vertical growth of ZnFe₂O₄ nanostructure, which promotes the transport of photogenerated carrier from the electrode surface to the electrolyte.

9.4.3. Mechanism of PEC water splitting using hematite photoelectrode

In order to improve the PEC water splitting using iron-oxide based photoanodes, it is important to understand the mechanism of this reaction on the solids' surface. Using spectroscopic method, Klahr et al. as well as Cummings et al. recorded an absorption characteristics around 570 nm formed during PEC water oxidation on hematite [285,286]. This band is attributed to the oxidized Fe^{III}–OH surface species forming Fe^{IV}O that is active intermediate in H₂O oxidation reaction as shown in Fig. 32. The oxidation/reduction (or hole trapping/de-trapping) is associated with the formation of Fe^{IV}O/Fe^{III}–OH on the surface of hematite electrodes as measured in CV experiments [267]. Durrant and co-workers [287–289] studied the photogenerated species with hematite electrodes under water oxidation conditions using transient absorption spectroscopy. They suggested that long-lived holes must be generated to initiate water oxidation. They found a correlation between the photocurrent and the density of long-lived holes. They also suggested that the hole transfer from hematite to the solution or surface-bound water species is the rate limiting step, with a series of one-electron oxidation steps as the main mechanism occurred for water oxidation with hematite. Although the chemical nature of the long-lived holes is not specifically indicated, their photoelectrochemical impedance spectra give the impression that long-lived holes are very likely

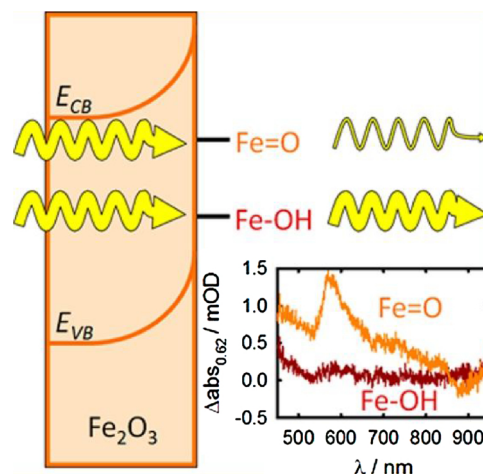


Fig. 32. Change in absorption spectra measured at 0.82 V vs. RHE (red) and 1.22 V vs. RHE (orange) measured under 0.1 mW cm⁻² 405 nm illumination with respect to the absorption spectra measured at 0.62 V. Reproduced with permission from reference [285] (For interpretation of the references to colour in this figure legend, the reader is referred to the web version of this article).

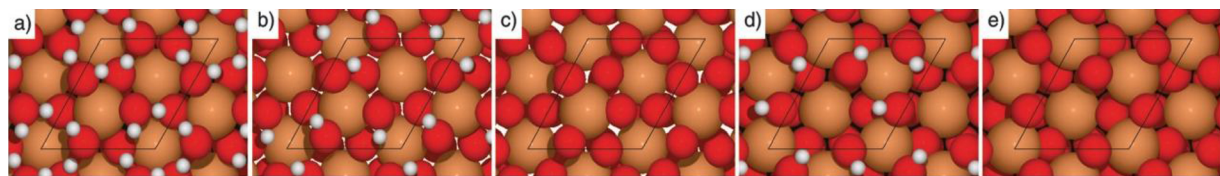
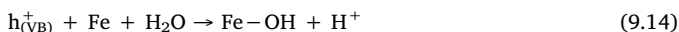
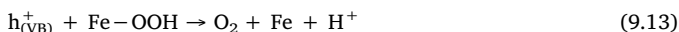
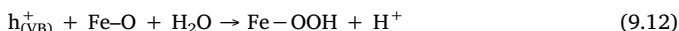


Fig. 33. Some possible surface terminations of α -Fe₂O₃: (a) (OH)₃-Fe-H₃O₃-R, (b) (OH)₃-Fe-O₃-R, (c) O₃-Fe-O₃-R, (d) (OH)₃-R, and (e) O₃-R. The unit cell is shown by the solid line. Reproduced with permission from reference [253].

the same species as surface-trapped holes.

The nature of the surface complexes on hematite has not been directly determined, however, the spectroscopic studies strongly support the formation of oxidized surface Fe–OH terminations, which further proceed to release O₂. Surface trapped holes is most likely a Fe^{IV}O group which can recombine with conduction and trapped electrons leading to surface recombination, or is possibly converted to Fe–O–OH and releases O₂ through a further oxidation and reaction with H₂O molecules [253]. This highlights the importance of surface terminations on the hole collection efficiency on hematite electrodes, which undoubtedly relate to the preparation methods. Therefore part of the difference in the practical results can arise from different measurement conditions [267]. It is generally accepted that surface states play an important role in determining water oxidation efficiency. In this context, the thermodynamics of reaction on the different surface terminations of (0001) Fe₂O₃ was investigated (see Fig. 33a–e). While Hellman and Pala [253] showed that hydroxylation of Fe₂O₃ is spontaneous, Trainor et al. [290] reported a fully hydroxylated species, are the thermodynamically most stable surface configurations of the (0001) surface in aqueous environments. These hydroxylated species are (OH)₃-Fe-H₃O₃-R and (OH)₃-R, where R represents the bulk hematite crystal. Based on these calculations, the oxidation of the surface terminated hydroxyl species, e.g. (OH)₃-Fe-H₃O₃-R and the removal of a proton (Eq. (9.11)) is the initial step in the photo-oxidation process, followed by an attack by a water molecule producing a surface peroxide intermediate species (Eq. (9.12)). An evolution of O₂ from this peroxide intermediate will then take place, leaving an unsaturated iron site on the surface (Eq. (9.13)). Finally, a coordination of a second water molecule will complete the reaction cycle (Eq. (9.14)). Young et al. [291] interpreted also a surface bound water species as an aqua, hydroxy, oxo, or peroxy ligand coordinated to a surface iron atom.

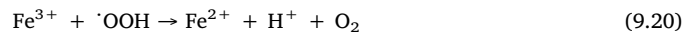
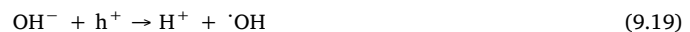
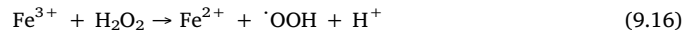
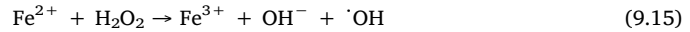


9.5. Interesting non-photocatalytic applications

Finally, one has to mention that iron-based nanostructures have demonstrated good catalytic potentials to overcome a series of environmental problems via either adsorption, reduction of heavy metals, or degradation of organic pollutants through a photo-Fenton reaction [292]. The leaching of Fe²⁺ and Fe³⁺ ions from iron oxide surface to the aqueous solution can accelerate the organic pollutant degradation by Fenton (Fe²⁺/H₂O₂) and Fenton-like (Fe³⁺/H₂O₂) reactions

[198,293]. Fe²⁺ on the surface can react with the oxygen dissolved in the reaction mixture generating Fe³⁺ ions and reactive oxygen species (O₂[·], H₂O₂ and ·OH) as shown in Fig. 34.

In the case when hydrogen peroxide is added to the iron-oxide based photocatalytic systems, Fenton-type reactions will take place, in which iron cations react with H₂O₂ according Eqs. (9.15)–(9.20) [162].



The addition of inorganic oxidants such as H₂O₂ (i.e photo-Fenton reaction), peroxymonosulfate PMS or peroxodisulfate PDS enhances the activity of ferrites [162]. These inorganic compounds can form in situ ·OH radicals or sulfate radicals (SO₄[·]), respectively [165]. Such ferrite-oxidant system provide additional benefits to the traditional Fenton systems such as avoiding sludge formation, operating under neutral pH condition, and the possibility of recycling iron compounds [295]. Sharma et al. [296] compared the visible light performance of magnetic spinel ferrites, having general formula MFe₂O₄ (M = Cu, Zn, Ni and Co) in the presence of different inorganic oxidants. The degradation rate of remazol black 5 was found to decrease in order H₂O₂ > KHSO₅ > K₂S₂O₈ > KBrO₃. When H₂O₂ and KHSO₅ were used, the reactivity of ferrites followed the order CuFe₂O₄ > ZnFe₂O₄ > NiFe₂O₄ > CoFe₂O₄ and CoFe₂O₄ > CuFe₂O₄ > NiFe₂O₄ > ZnFe₂O₄, respectively.

10. Conclusions

The growing scientific interest on nanostructured hematite photo-anodes for visible light water splitting allowed the understanding of the fundamental properties affecting the activity of this material. There is no doubt that abundance and low cost are advantages that every semiconductor must meet for their application in large-scale photocatalytic and photoelectrocatalytic systems. These two properties turned hematite into an enormously attractive material in this field. Attractive enough to devote large scientific efforts to overcome its main limitations: fast charge carrier recombination rates and short diffusion lengths. Although still distant from technical applications, the efficiencies of hematite photoanodes have been continuously improved. Nevertheless, the strategies usually employed to tackle these limitations required complex chemical and physical processes. The nanoscale approach has proven to be a working strategy, to a certain extent, to improve the performance of photoelectrodes with low carrier mobility

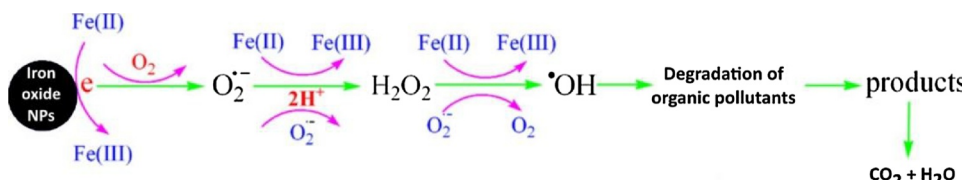


Fig. 34. The photocatalytic degradation mechanisms of organic pollutants by iron oxide. Adapted with permission from reference [294].

and short photogenerated carrier lifetimes. However, the performance of materials is ultimately defined by its chemical and physical properties and many drawbacks can't be solved by nanoscaling them. Hence, other strategies should be adopted as well. To overcome the short carrier lifetimes, the development of functional nanoengineered hematite photoanodes, usually by the combination with precious metal co-catalysts, is required. These complex materials are not inexpensive due to the cost of the noble metals and the complicated preparation routes, and the cost factor has to be considered.

The large knowledge collected for hematite is now of a great help to analyze the behavior of other iron-based compounds. Most of the scientific efforts are currently focused on the development of new materials via addressing the above-mentioned drawbacks. In this review article, light has been shed in other iron-based compounds rather than hematite, namely, iron oxy-hydroxide, iron-based perovskites, and ferrites. These semiconductors are proven to be promising and worth pursuing further. Nevertheless, there is still a lot to go. The effect of some physicochemical properties, such as the degree of inversion of ferrites or the multiferroicity of BiFeO_3 on the photocatalytic and photoelectrocatalytic activity is still not clear. Furthermore, an in-depth characterization regarding the charge carrier dynamics and a study of the surface chemistry behind the photocatalytic and photoelectrocatalytic processes at the surface of iron-containing semiconductors is lacking. In addition, the stability of iron compounds is still a common problem, especially in high alkaline and acidic media. Reduction of Fe^{3+} to Fe^{2+} and leaching of iron from the photocatalyst into the electrolyte is a major obstacle to durability and long-term usability of iron-based compounds. Solid solutions in which wide band gap robust perovskites, like SrTiO_3 , or oxides, like TiO_2 , are combined with iron-based compounds could represent a viable approach.

11. Perspectives and future

The field of environmental remediation assisted by photocatalytic processes is an exciting research subject that continues capturing the interest of scientists. At first glance, the photocatalytic process seems to be simple, but it demands a fine-tuning of several parameters that depend not only on the photocatalytic material. In addition, comparing the generally unsystematic experimental results is very complicated. The preparation methods for photocatalytic nanoparticles are varied, affecting the properties of the resulting material. Furthermore, standard tests to evaluate the photocatalytic efficiency are lacking. A clear example is the photocatalytic water splitting reaction. Many researchers report achieving photocatalytic water splitting in their works. However, they have conducted their experiments in the presence of sacrificial electron donors to produce molecular hydrogen. Real photocatalytic water splitting consists in producing hydrogen gas from the reduction of water with simultaneous oxidation of water to molecular oxygen without the interaction of electron or hole scavengers.

Most of the past and current studies are limited to laboratory investigations while the number of practical applications is still limited. Scientists make a lot of effort to increase their efficiencies and stability in the different experimental conditions. Although iron-based materials with their magnetic characteristics and contrast have already been successfully applied in areas of biomedicine, including diagnostics, targeting, nanocarrier, chemo and phototherapy agents, they still stumble, to some extent, in the field of photocatalysis. Different strategies including nanostructuring or the use of non-abundant and expensive co-catalysts and dopants are normally applied. More progression in the novel synthesis of nanocomposites with multifunctional modalities can find better ways to use iron-based oxides as a photocatalyst. Also, solid solution that incorporates wide band gap semiconductors, normally known to be highly stable, and iron-based oxides offer a good route to follow in order to achieve stability and good photocatalytic properties. Nevertheless, such strategies still need further studies to come to a solid conclusion or to achieve a breakthrough.

When large-scale applications are the final goal, the research focus should be directed towards the use of abundant and noble-metal free cocatalysts and protective layers. From the economical point of view, the high cost of the photocatalysts might be overcome by ensuring their reuse. In this regard, the magnetism of several iron-based materials is an advantage when combined in core-shell structures. The resulting hybrid materials possess a shell that provides the desired functionality and a magnetic core that allows an easy particle separation. The combination of iron-based materials with other photocatalysts is a good opportunity to enhance their activity and reduce their well-known photocorrosion. Graphene seems to be a good candidate for forming such hybrid structures due to its interesting electrical and mechanical properties and its high surface area. However, understanding the relationship between these both parts of the composite is a prerequisite for the broad application of these nanomaterials in photocatalysis.

Iron-based nanostructures are still promising materials for applications in solar-fuel generation and environmental remediation. Due to the continuously increasing knowledge about the fundamental aspects behind their photocatalytic performances and the constant synthesis of new compounds, the future perspectives are optimistic. The application-oriented research should carefully consider the previously discussed technical limitations in order to achieve significant results.

Acknowledgements

This Special Issue is dedicated to honor the retirement of Dr. John Kiwi at the Swiss Federal Institute of Technology (Lausanne), a key figure in the topic of photocatalytic materials for the degradation of contaminants of environmental concern.

Yamen AlSalka would like to acknowledge the support from the program 57169181 granted by the Deutscher Akademischer Austauschdienst (DAAD) and the Federal Foreign Office. Wegdan Ramadan is thankful to the Alexander von Humboldt foundation for the financial support. Financial support by the Korean Government (MSIP) through the NRF under the Global Research Laboratory program (2014K1A1A2041044), the Deutsche Forschungsgemeinschaft under the program SPP 1613 (BA 1137/22-1), and the Niedersächsische Ministerium für Wissenschaft und Kultur (NTH-research group "ElektroBak") is gratefully acknowledged.

References

- [1] M. Mishra, D.-M. Chun, $\alpha\text{-Fe}_2\text{O}_3$ as a photocatalytic material: a review, *Appl. Catal. A Gen.* 498 (2015) 126–141.
- [2] K. Sivula, F. Le Formal, M. Grätzel, Solar water splitting: progress using hematite ($\alpha\text{-Fe}_2\text{O}_3$) photoelectrodes, *ChemSusChem* 4 (2011) 432–449.
- [3] S.D. Tilley, M. Cornuz, K. Sivula, M. Grätzel, Light-induced water splitting with hematite: improved nanostructure and iridium oxide catalysis, *Angew. Chem.* 122 (2010) 6549–6552.
- [4] G. Wang, Y. Ling, D.A. Wheeler, K.E. George, K. Horsley, C. Heske, J.Z. Zhang, Y. Li, Facile synthesis of highly photoactive $\alpha\text{-Fe}_2\text{O}_3$ -based films for water oxidation, *Nano Lett.* 11 (2011) 3503–3509.
- [5] S.-M. Lam, J.-C. Sin, A.R. Mohamed, A newly emerging visible light-responsive BiFeO_3 perovskite for photocatalytic applications: a mini review, *Mater. Res. Bull.* 90 (2017) 15–30.
- [6] D.H. Taffa, R. Dillert, A.C. Ulpe, K.C. Bauerfeind, T. Bredow, D.W. Bahnemann, M. Wark, Photoelectrochemical and theoretical investigations of spinel type ferrites ($\text{M}_x\text{Fe}_{3-x}\text{O}_4$) for water splitting: a mini-review, *J. Photonics Energy* 7 (2016) 012009.
- [7] R. Dillert, D.H. Taffa, M. Wark, T. Bredow, D.W. Bahnemann, Research update: photoelectrochemical water splitting and photocatalytic hydrogen production using ferrites (MFe_2O_4) under visible light irradiation, *APL Mater.* 3 (2015) 104001.
- [8] G. Smolenskii, I. Chupis, Ferroelectromagnets, *Sov. Phys. Uspekhi* 25 (1982) 475.
- [9] I. Sosnowska, M. Loewenhaupt, W. David, R. Ibberson, Investigation of the unusual magnetic spiral arrangement in BiFeO_3 , *Phys. B Condens. Matter* 180 (1992) 117–118.
- [10] T.-J. Park, G.C. Papaefthymiou, A.J. Vescas, A.R. Moodenbaugh, S.S. Wong, Size-dependent magnetic properties of single-crystalline multiferroic BiFeO_3 nanoparticles, *Nano Lett.* 7 (2007) 766–772.
- [11] R.M. Cornell, U. Schwertmann, The iron oxides: structure, properties, reactions, Occurrences and Uses, 2nd ed., Wiley-VCH, 2003.
- [12] U. Schwertmann, R.M. Cornell, Iron Oxides in the Laboratory: Preparation and

Characterization, 2nd ed., Wiley-VCH, 2000.

[13] J. Lee, S. Han, Thermodynamics of native point defects in α -Fe₂O₃: an ab initio study, *Phys. Chem. Chem. Phys.* 15 (2013) 18906–18914.

[14] L. Pauling, S.B. Hendricks, The crystal structures of hematite and corundum, *J. Am. Chem. Soc.* 47 (1925) 781–790.

[15] S. Petit, S.T.A.G. Melissen, L. Duclaux, M.T. Sougrati, T. Le Bahers, P. Sautet, D. Dambournet, O. Borkiewicz, C. Laberty-Robert, O. Durupthy, How should iron and titanium be combined in oxides to improve photoelectrochemical properties? *J. Phys. Chem. C* 120 (2016) 24521–24532.

[16] K. Momma, F. Izumi, VESTA 3 for three-dimensional visualization of crystal, volumetric and morphology data, *J. Appl. Crystallogr.* 44 (2011) 1272–1276.

[17] D.M. Sherman, T.D. Waite, Electronic spectra of Fe³⁺ oxides and oxide hydroxides in the near IR to near UV, *Am. Mineral.* 70 (1985) 1262–1269.

[18] A.W. Adamson, W.L. Waltz, E. Zinato, D.W. Watts, P.D. Fleischauer, R.D. Lindholm, Photochemistry of transition-metal coordination compounds, *Chem. Rev.* 68 (1968) 541–585.

[19] D.M. Sherman, Crystal chemistry, electronic structures, and spectra of Fe sites in clay minerals: applications to photochemistry and electron transport, in: C.L. M.S.W. S., B.D. F. (Eds.), *Spectroscopic Characterization of Minerals and Their Surfaces*, ACS Publications, 1990, pp. 284–309.

[20] E. Guiot, Z.Y. Wu, S. Gota, M. Gautier-Soyer, Polarized OK edge spectra of Fe₂O₃ (0001) nanometric films: a full multiple scattering interpretation, *J. Electron Spectrosc. Relat. Phenomena* 101 (1999) 371–375.

[21] W. Mackrodt, F. Jollet, M. Gautier-Soyer, A first-principles Hartree-Fock interpretation of the X-ray oxygen K-edge spectrum of haematite (α -Fe₂O₃), *Philos. Mag. B* 79 (1999) 25–36.

[22] F. De Groot, M. Grioni, J. Fuglie, J. Ghijssen, G. Sawatzky, H. Petersen, Oxygen 1s x-ray-absorption edges of transition-metal oxides, *Phys. Rev. B* 40 (1989) 5715.

[23] B. Gilbert, C. Frandsen, E. Maxey, D. Sherman, Band-gap measurements of bulk and nanoscale hematite by soft x-ray spectroscopy, *Phys. Rev. B* 79 (2009) 035108.

[24] Y. Ma, P. Johnson, N. Wassdahl, J. Guo, P. Skytt, J. Nordgren, S. Kevan, J.-E. Rubensson, T. Böske, W. Eberhardt, Electronic structures of α -Fe₂O₃ and Fe₃O₄ from O K-edge absorption and emission spectroscopy, *Phys. Rev. B* 48 (1993) 2109.

[25] Z. Wu, S. Gota, F. Jollet, M. Pollak, M. Gautier-Soyer, C. Natoli, Characterization of iron oxides by x-ray absorption at the oxygen K edge using a full multiple-scattering approach, *Phys. Rev. B* 55 (1997) 2570.

[26] S. Sorenson, E. Driscoll, S. Haghight, J.M. Dawlaty, Ultrafast carrier dynamics in hematite films: the role of photoexcited electrons in the transient optical response, *J. Phys. Chem. C* 118 (2014) 23621–23626.

[27] S.R. Pendlebury, M. Barroso, A.J. Cowan, K. Sivula, J. Tang, M. Grätzel, D. Klug, J.R. Durrant, Dynamics of photogenerated holes in nanocrystalline α -Fe₂O₃ electrodes for water oxidation probed by transient absorption spectroscopy, *Chem. Commun.* 47 (2011) 716–718.

[28] S. Shen, S.A. Lindley, X. Chen, J.Z. Zhang, Hematite heterostructures for photoelectrochemical water splitting: rational materials design and charge carrier dynamics, *Energy Environ. Sci.* 9 (2016) 2744–2775.

[29] M. Barroso, C.A. Mesa, S.R. Pendlebury, A.J. Cowan, T. Hisatomi, K. Sivula, M. Grätzel, D.R. Klug, J.R. Durrant, Dynamics of photogenerated holes in surface modified α -Fe₂O₃ photoanodes for solar water splitting, *Proc. Natl. Acad. Sci.* 109 (2012) 15640–15645.

[30] D.A. Wheeler, G. Wang, Y. Ling, Y. Li, J.Z. Zhang, Nanostructured hematite: synthesis, characterization, charge carrier dynamics, and photoelectrochemical properties, *Energy Environ. Sci.* 5 (2012) 6682–6702.

[31] N.J. Cherepy, D.B. Liston, J.A. Lovejoy, H. Deng, J.Z. Zhang, Ultrafast studies of photoexcited electron dynamics in γ - and α -Fe₂O₃ semiconductor nanoparticles, *J. Phys. Chem. B* 102 (1998) 770–776.

[32] J. Moser, M. Grätzel, Photoelectrochemistry with colloidal semiconductors; laser studies of halide oxidation in colloidal dispersions of TiO₂ and α -Fe₂O₃, *Helv. Chim. Acta* 65 (1982) 1436–1444.

[33] R. Stramal, J. Thomas, Photochemistry of iron oxide colloids, *J. Colloid Interface Sci.* 110 (1986) 121–129.

[34] S. Kerisit, K.M. Rosso, Kinetic Monte Carlo model of charge transport in hematite (α -Fe₂O₃), *J. Chem. Phys.* 127 (2007) 124706.

[35] M. Barroso, S.R. Pendlebury, A.J. Cowan, J.R. Durrant, Charge carrier trapping, recombination and transfer in hematite (α -Fe₂O₃) water splitting photoanodes, *Chem. Sci.* 4 (2013) 2724–2734.

[36] G. Wang, Y. Ling, Y. Li, Oxygen-deficient metal oxide nanostructures for photoelectrochemical water oxidation and other applications, *Nanoscale* 4 (2012) 6682–6691.

[37] N. Dimitrijevic, D. Savic, O. Micic, A. Nozilic, Interfacial electron-transfer equilibria and flatband potentials of alpha-ferric oxide and titanium dioxide colloids studied by pulse radiolysis, *J. Phys. Chem.* 88 (1984) 4278–4283.

[38] F. Morin, Electrical properties of α -Fe₂O₃, *Phys. Rev.* 93 (1954) 1195.

[39] J.H. Kennedy, K.W. Frese, Flatband potentials and donor densities of polycrystalline α -Fe₂O₃ determined from mott-schottky plots, *J. Electrochem. Soc.* 125 (1978) 723–726.

[40] H. Dotan, K. Sivula, M. Grätzel, A. Rothschild, S.C. Warren, Probing the photoelectrochemical properties of hematite (α -Fe₂O₃) electrodes using hydrogen peroxide as a hole scavenger, *Energy Environ. Sci.* 4 (2011) 958–964.

[41] P. Liao, M.C. Toroker, E.A. Carter, Electron transport in pure and doped hematite, *Nano Lett.* 11 (2011) 1775–1781.

[42] M. Butler, Photoelectrolysis and physical properties of the semiconducting electrode WO₂, *J. Appl. Phys.* 48 (1977) 1914–1920.

[43] H. Tang, K. Prasad, R. Sanjines, P. Schmid, F. Levy, Electrical and optical properties of TiO₂ anatase thin films, *J. Appl. Phys.* 75 (1994) 2042–2047.

[44] Y. Yamada, Y. Kanemitsu, Determination of electron and hole lifetimes of rutile and anatase TiO₂ single crystals, *Appl. Phys. Lett.* 101 (2012) 133907.

[45] W. Gissler, R. Memming, Photoelectrochemical processes at semiconducting WO₃ layers, *J. Electrochem. Soc.* 124 (1977) 1710–1714.

[46] J. Schoonman, K. Vos, G. Blasse, Donor densities in TiO₂ photoelectrodes, *J. Electrochem. Soc.* 128 (1981) 1154–1157.

[47] M. Gondal, M. Sayeed, A. Alarfaj, Activity comparison of Fe₂O₃, NiO, WO₃, TiO₂ semiconductor catalysts in phenol degradation by laser enhanced photo-catalytic process, *Chem. Phys. Lett.* 445 (2007) 325–330.

[48] K.M. Rosso, D.M. Smith, M. Dupuis, An ab initio model of electron transport in hematite (α -Fe₂O₃) basal planes, *J. Chem. Phys.* 118 (2003) 6455–6466.

[49] Y. Ling, G. Wang, J. Reddy, C. Wang, J.Z. Zhang, Y. Li, The influence of oxygen content on the thermal activation of hematite nanowires, *Angew. Chemie* 124 (2012) 4150–4155.

[50] E. Voloshina, Hematite, its stable surface terminations and their reactivity toward water, reference module in chemistry, Molecular Sciences and Chemical Engineering, Elsevier, 2013.

[51] H. Guo, A.S. Barnard, Thermodynamic modelling of nanomorphologies of hematite and goethite, *J. Mater. Chem.* 21 (2011) 11566–11577.

[52] S.K. Shaikhutdinov, W. Weiss, Oxygen pressure dependence of the α -Fe₂O₃ (0001) surface structure, *Surf. Sci.* 432 (1999) L627–L634.

[53] S. Thevuthasan, Y. Kim, S. Yi, S. Chambers, J. Morais, R. Denecke, C. Fadley, P. Liu, T. Kendelewicz, G. Brown Jr., Surface structure of MBE-grown α -Fe₂O₃ (0001) by intermediate-energy X-ray photoelectron diffraction, *Surf. Sci.* 425 (1999) 276–286.

[54] S. Chambers, S. Yi, Fe termination for α -Fe₂O₃ (0001) as grown by oxygen-plasma-assisted molecular beam epitaxy, *Surf. Sci.* 439 (1999) L785–L791.

[55] I.C. Man, H.Y. Su, F. Calle-Vallejo, H.A. Hansen, J.I. Martínez, N.G. Inoglu, J. Kitchin, T.F. Jaramillo, J.K. Nørskov, J. Rossmeisl, Universality in oxygen evolution electrocatalysis on oxide surfaces, *ChemCatChem* 3 (2011) 1159–1165.

[56] J. Rossmeisl, Z.-W. Qu, H. Zhu, G.-J. Kroes, J.K. Nørskov, Electrolysis of water on oxide surfaces, *J. Electroanal. Chem.* 607 (2007) 83–89.

[57] P. Liao, J.A. Keith, E.A. Carter, Water oxidation on pure and doped hematite (0001) surfaces: prediction of Co and Ni as effective dopants for electrocatalysis, *J. Am. Chem. Soc.* 134 (2012) 13296–13309.

[58] M. Gautier-Soyer, M. Pollak, M. Henriot, M. Guillet, The (1 \times 2) reconstruction of the α -Fe₂O₃ (1012) surface, *Surf. Sci.* 352 (1996) 112–116.

[59] M.A. Henderson, S.A. Joyce, J.R. Rustad, Interaction of water with the (1 \times 1) and (2 \times 1) surfaces of α -Fe₂O₃ (012), *Surf. Sci.* 417 (1998) 66–81.

[60] G.M. Wang, Y.C. Ling, D.A. Wheeler, K.E.N. George, K. Horsley, C. Heske, J.Z. Zhang, Y. Li, Facile Synthesis of Highly Photoactive alpha-Fe₂O₃-Based Films for Water Oxidation, *Nano Lett.* 11 (2011) 3503–3509.

[61] J.A. Glasscock, P.R.F. Barnes, I.C. Plumb, N. Savvides, Enhancement of photoelectrochemical hydrogen production from hematite thin films by the introduction of Ti and Si, *J. Phys. Chem. C* 111 (2007) 16477–16488.

[62] N.T. Hahn, C.B. Mullins, Photoelectrochemical performance of nanostructured Ti- and Sn-Doped alpha-Fe₂O₃ photoanodes, *Chem. Mater.* 22 (2010) 6474–6482.

[63] M.G. Ahmed, I.E. Kretschmer, T.A. Kandiel, A.Y. Ahmed, F.A. Rashwan, D.W. Bahnemann, A Facile Surface Passivation of Hematite Photoanodes with TiO₂ Overlays for Efficient Solar Water Splitting, *ACS Appl. Mater. Interfaces* 7 (2015) 24053–24062.

[64] K. Zhang, T.J. Dong, G.C. Xie, L.M. Guan, B.D. Guo, Q. Xiang, Y.W. Dai, L.Q. Tian, A. Batool, S.U. Jan, R. Boddula, A.A. Thebo, J.R. Gong, Sacrificial interlayer for promoting charge transport in hematite photoanode, *ACS Appl. Mater. Interfaces* 9 (2017) 42723–42733.

[65] C.Y. Wang, C. Bottcher, D.W. Bahnemann, J.K. Dohrmann, A comparative study of nanometer sized Fe(III)-doped TiO₍₂₎ photocatalysts: synthesis, characterization and activity, *J. Mater. Chem.* 13 (2003) 2322–2329.

[66] H.C. Wu, S.H. Li, S.W. Lin, Effect of Fe concentration on Fe-Doped anatase TiO₂ from GGA + U calculations, *Int. J. Photoenergy* (2012).

[67] V.N. Krasil'nikov, V.P. Zhukov, L.A. Perelyaeva, I.V. Baklanova, I.R. Shein, Electronic band structure, optical absorption, and photocatalytic activity of iron-doped anatase, *Phys. Solid State* 55 (2013) 1903–1912.

[68] A.A. Jelle, M. Hmadedh, P.G. O'Brien, D.D. Perovic, G.A. Ozin, Photocatalytic properties of all four polymorphs of nanostructured Iron oxyhydroxides, *ChemNanoMat* 2 (2016) 1047–1054.

[69] H. Yang, R. Lu, R.T. Downs, G. Costin, Goethite, α -FeO(OH), from single-crystal data, *Acta Crystallogr. Sect. E Struct. Rep. Online* 62 (2006) i250–i252.

[70] D. Strangway, R. Honea, B. McMahon, E. Larson, The magnetic properties of naturally occurring goethite, *Geophys. J. Int.* 15 (1968) 345–359.

[71] J. Forsyth, I. Hedley, C. Johnson, The magnetic structure and hyperfine field of goethite (α -FeOOH), *J. Phys. C Solid State Phys.* 1 (1968) 179.

[72] R.V. Morris, H.V. Lauer, C.A. Lawson, E.K. Gibson, G.A. Nace, C. Stewart, Spectral and other physicochemical properties of submicron powders of hematite (α -Fe₂O₃), maghemite (γ -Fe₂O₃), magnetite (Fe₃O₄), goethite (α -FeOOH), and lepidocrocite (γ -FeOOH), *J. Geophys. Res. Solid Earth* 90 (1985) 3126–3144.

[73] H. Zhang, M. Bayne, S. Fernando, B. Legg, M. Zhu, R.L. Penn, J.F. Banfield, Size-dependent bandgap of nanogoethite, *J. Phys. Chem. C* 115 (2011) 17704–17710.

[74] J. Ma, C. Zhu, J. Lu, B. Ouyang, Q. Xie, H. Liu, S. Peng, T. Chen, Kinetics analysis of interfacial electron-transfer processes in goethite suspensions systems, *Chemosphere* 188 (2017) 667–676.

[75] J.E. Katz, X. Zhang, K. Attenkofer, K.W. Chapman, C. Frandsen, P. Zarzycki, K.M. Rosso, R.W. Falcone, G.A. Waychunas, B. Gilbert, Electron small polaron and their mobility in iron (oxyhydr) oxide nanoparticles, *Science* 337 (2012) 1200–1203.

[76] W. Feng, D. Nansheng, Photochemistry of hydrolytic iron (III) species and photoinduced degradation of organic compounds. A mini review, *Chemosphere* 41 (2000) 1137–1147.

[77] T.D. Waite, F.M. Morel, Photoreductive dissolution of colloidal iron oxides in natural waters, *Environ. Sci. Technol.* 18 (1984) 860–868.

[78] C. Pulgarin, J. Kiwi, Iron oxide-mediated degradation, photodegradation, and biodegradation of aminophenols, *Langmuir* 11 (1995) 519–526.

[79] W. Ramadan, R. Dillert, J. Koch, C. Tegenkamp, D.W. Bahnemann, Changes in the solid-state properties of bismuth iron oxide during the photocatalytic reformation of formic acid, *Catal. Today* (2018).

[80] G. Ruppert, R. Bauer, G. Heisler, The photo-Fenton reaction—an effective photochemical wastewater treatment process, *J. Photochem. Photobiol. A Chem.* 73 (1993) 75–78.

[81] T. Li, G. Zhang, P. Wang, Removal of BPA through a goethite-photocatalyzed fenton-like reaction with the enhancement of oxalic acid, material science and environmental engineering, Proceedings of the 3rd Annual 2015 International Conference on Material Science and Environmental Engineering (ICMSEE2015, Wuhan, Hubei, China, 5–6 June 2015) (2015) 115.

[82] Y. Mameri, N. Debbache, M. el mehdi Benacherine, N. Seraghni, T. Sehili, Heterogeneous photodegradation of paracetamol using Goethite/H₂O₂ and Goethite/oxalic acid systems under artificial and natural light, *J. Photochem. Photobiol. A Chem.* 315 (2016) 129–137.

[83] S. Belattar, N. Debbache, I. Ghoul, T. Sehili, A. Abdessemed, Photodegradation of phenol red in the presence of oxyhydroxide of Fe (III)(Goethite) under artificial and a natural light, *Water Environ. J.* 32 (2018) 358–365.

[84] F. Gaboriaud, J.-J. Ehrhardt, Effects of different crystal faces on the surface charge of colloidal goethite (α -FeOOH) particles: an experimental and modeling study, *Geochim. Cosmochim. Acta* 67 (2003) 967–983.

[85] H. Li, T. Wang, Y. Zhang, L. Jiang, C. Shu, C. Wang, Controllable fabrication of Iron oxide/oxyhydroxide with diverse nanostructures and their excellent performance in visible light induced photocatalytic degradation of rhodamine B, *J. Nanosci. Nanotechnol.* 12 (2012) 1910–1918.

[86] S. Kakuta, T. Numata, T. Okayama, Shape effects of goethite particles on their photocatalytic activity in the decomposition of acetaldehyde, *Catal. Sci. Technol.* 4 (2014) 164–169.

[87] M. Fracchia, A. Visibile, E. Ahlberg, A. Vertova, A. Minguzzi, P. Ghigna, S. Rondinini, α -and γ -FeOOH: Stability, Reversibility, and Nature of the Active Phase under Hydrogen Evolution, *Acc Appl. Energy Mater.* 1 (2018) 1716–1725.

[88] W. Luo, C. Jiang, Y. Li, S.A. Shevlin, X. Han, K. Qiu, Y. Cheng, Z. Guo, W. Huang, J. Tang, Highly crystallized α -FeOOH for a stable and efficient oxygen evolution reaction, *J. Mater. Chem. A* 5 (2017) 2021–2028.

[89] H.D. Megaw, Crystal structure of barium titanate, *Nature* 155 (1945) 484–485.

[90] P. Lemmens, P. Millet, Spin–orbit–topology, a triptych, *Quantum Magnetism*, Springer, 2004, pp. 433–477.

[91] C. Frontera, J. García-Muñoz, A. Llobet, M.A.G. Aranda, Selective spin-state switch and metal-insulator transition in GdBa₂Co_{5.5}, *Phys. Rev. B* 65 (2002) 180405.

[92] U. Müller, *Inorganic Structural Chemistry*, New York (1993).

[93] R.V. Shpanchenko, V.V. Chernaya, A.A. Tsirlin, P.S. Chizhov, D.E. Sklovsky, E.V. Antipov, E.P. Khlybov, V. Pomjakushin, A.M. Balagurov, J.E. Medvedeva, Synthesis, structure, and properties of new perovskite PbVO₃, *Chem. Mater.* 16 (2004) 3267–3273.

[94] M. Holcomb, L. Martin, A. Scholl, Q. He, P. Yu, C.-H. Yang, S. Yang, P.-A. Glans, M. Valvidares, M. Huijben, Probing the evolution of antiferromagnetism in multiferroics, *Phys. Rev. B* 81 (2010) 134406.

[95] S. Kiselev, Detection of magnetic order in ferroelectric BiFeO₃ by neutron diffraction, *Sov. Phys. J.* 7 (1963) 742.

[96] S. Geller, Crystal structure of gadolinium orthoferrite, GdFeO₃, *J. Chem. Phys.* 24 (1956) 1236–1239.

[97] R.W. Wyckoff, *Crystal Structures Vol 1*, Interscience Publishers, New York, 1948.

[98] R.H. Langley, C.K. Schmitz, M.B. Langley, The synthesis and characterization of some fluoride perovskites, an undergraduate experiment in solid state chemistry, *J. Chem. Educ.* 61 (1984) 643.

[99] M.A. Peña, J.L.G. Fierro, Chemical structures and performance of perovskite oxides, *Chem. Rev.* 101 (2001) 1981–2018.

[100] V.M. Goldschmidt, Die gesetze der krystallochemie, *Naturwissenschaften* 14 (1926) 477–485.

[101] A.F. Wells, *Structural Inorganic Chemistry*, Oxford university press, 2012.

[102] C.A. Gueynard, The sun's total and spectral irradiance for solar energy applications and solar radiation models, *Sol. Energy* 76 (2004) 423–453.

[103] K. Maeda, Rhodium-doped barium titanate perovskite as a stable p-type semiconductor photocatalyst for hydrogen evolution under visible light, *ACS Appl. Mater. Interfaces* 6 (2014) 2167–2173.

[104] L. Li, Y. Zhang, A.M. Schultz, X. Liu, P.A. Salvador, G.S. Rohrer, Visible light photochemical activity of heterostructured PbTiO₃–TiO₂ core–shell particles, *Catal. Sci. Technol.* 2 (2012) 1945–1952.

[105] K. Van Benthem, C. Elsässer, R. French, Bulk electronic structure of SrTiO₃: experiment and theory, *J. Appl. Phys.* 90 (2001) 6156–6164.

[106] Y. Xu, M.A. Schoonen, The absolute energy positions of conduction and valence bands of selected semiconducting minerals, *Am. Mineral.* 85 (2000) 543–556.

[107] H. Kato, A. Kudo, Water splitting into H₂ and O₂ on alkali tantalate photocatalysts ATaO₃ (A = Li, Na, and K), *J. Phys. Chem. B* 105 (2001) 4285–4292.

[108] H. Kato, K. Asakura, A. Kudo, Highly efficient water splitting into H₂ and O₂ over lanthanum-doped NaTaO₃ photocatalysts with high crystallinity and surface nanostructure, *J. Am. Chem. Soc.* 125 (2003) 3082–3089.

[109] A. Yamakata, T.-a. Ishibashi, H. Kato, A. Kudo, H. Onishi, Photodynamics of NaTaO₃ catalysts for efficient water splitting, *J. Phys. Chem. B* 107 (2003) 14383–14387.

[110] P. Kanhere, P. Shenai, S. Chakraborty, R. Ahuja, J. Zheng, Z. Chen, Mono-and co-doped NaTaO₃ for visible light photocatalysis, *J. Chem. Soc. Faraday Trans. 16* (2014) 16085–16094.

[111] W. Ramadan, P.A. Shaikh, S. Ebrahim, A. Ramadan, B. Hannoyer, S. Jouen, X. Sauvage, S. Ogale, Highly efficient photocatalysis by BiFeO₃/ α (γ)-Fe₂O₃ ferrimagnetic nano p/n junctions formed by dopant-induced phase separation, *J. Nanoparticle Res.* 15 (2013) 1848.

[112] P. Dhanasekaran, N. Gupta, Factors affecting the production of H₂ by water splitting over a novel visible-light-driven photocatalyst GaFeO₃, *Int. J. Hydrogen Energy* 37 (2012) 4897–4907.

[113] P. Tang, H. Chen, F. Cao, G. Pan, Magnetically recoverable and visible-light-driven nanocrystalline YFeO₃ photocatalysts, *Catal. Sci. Technol.* 1 (2011) 1145–1148.

[114] S.E. Haggerty, V. Sautter, Ultradep (Greater than 300 kilometers), ultramafic upper mantle xenoliths, *Science* 248 (1990) 993–996.

[115] X. Xu, Y. Chen, W. Zhou, Y. Zhong, D. Guan, Z. Shao, Earth-abundant silicon for facilitating water oxidation over iron-based perovskite electrocatalyst, *Adv. Mater. Interfaces* (2018) 1701693.

[116] A. Kumar, R.C. Rai, N.J. Podraza, S. Denev, M. Ramirez, Y.-H. Chu, L.W. Martin, J. Ihlefeld, T. Heeg, J. Schubert, Linear and nonlinear optical properties of BiFeO₃, *Appl. Phys. Lett.* 92 (2008) 121915.

[117] R. Palai, R. Katiyar, H. Schmid, P. Tissot, S. Clark, J. Robertson, S. Redfern, G. Catalan, J. Scott, B phase and γ – β metal-insulator transition in multiferroic BiFeO₃, *Phys. Rev. B* 77 (2008) 014110.

[118] C.-W. Nan, M. Bichurin, S. Dong, D. Viehland, G. Srinivasan, Multiferroic magnetoelectric composites: historical perspective, status, and future directions, *J. Appl. Phys.* 103 (2008) 1.

[119] M. Fiebig, Revival of the magnetoelectric effect, *J. Phys. D Appl. Phys.* 38 (2005) R123.

[120] H. Schmid, Multi-ferroic magnetoelectrics, *Ferroelectrics* 162 (1994) 317–338.

[121] J.F. Ihlefeld, N.J. Podraza, Z.K. Liu, R.C. Rai, X. Xu, T. Heeg, Y.B. Chen, J. Li, R.W. Collins, J.L. Musfeldt, X.Q. Pan, J. Schubert, R. Ramesh, D.G. Schlom, Optical band gap of BiFeO₃ grown by molecular-beam epitaxy, *Appl. Phys. Lett.* 92 (2008) 142908.

[122] R.V. Pisarev, A.S. Moskvin, A.M. Kalashnikova, T. Rasing, Charge transfer transitions in multiferroic BiFeO₃ and related ferrite insulators, *Phys. Rev. B* 79 (2009) 235128.

[123] S.J. Clark, J. Robertson, Band gap and Schottky barrier heights of multiferroic BiFeO₃, *Appl. Phys. Lett.* 90 (2007) 132903.

[124] J.B. Neaton, C. Edler, U.V. Waghmare, N.A. Spaldin, K.M. Rabe, First-principles study of spontaneous polarization in multiferroic BiFeO₃, *Phys. Rev. B* 71 (2005) 014113.

[125] M.O. Ramirez, A. Kumar, S.A. Denev, N.J. Podraza, X.S. Xu, R.C. Rai, Y.H. Chu, J. Seidel, L.W. Martin, S.Y. Yang, E. Saiz, J.F. Ihlefeld, S. Lee, J. Klug, S.W. Cheong, M.J. Bedzyk, O. Auciello, D.G. Schlom, R. Ramesh, J. Orenstein, J.L. Musfeldt, V. Gopalan, Magon sidebands and spin-charge coupling in bismuth ferrite probed by nonlinear optical spectroscopy, *Phys. Rev. B* 79 (2009) 224106.

[126] S.R. Basu, L.W. Martin, Y.H. Chu, M. Gajek, R. Ramesh, R.C. Rai, X. Xu, J.L. Musfeldt, Photoconductivity in BiFeO₃ thin films, *Appl. Phys. Lett.* 92 (2008) 091905.

[127] Y.-W. Chen, J.-L. Kuo, K.-H. Chew, Polar ordering and structural distortion in electronic domain-wall properties of BiFeO₃, *J. Appl. Phys.* 122 (2017) 075103.

[128] W. Ji, K. Yao, Y.-F. Lim, Y.C. Liang, A. Suwardi, Epitaxial ferroelectric BiFeO₃ thin films for unassisted photocatalytic water splitting, *Appl. Phys. Lett.* 103 (2013) 062901.

[129] J. Song, T.L. Kim, J. Lee, S.Y. Cho, J. Cha, S.Y. Jeong, H. An, W.S. Kim, Y.-S. Jung, J. Park, Domain-engineered BiFeO₃ thin-film photoanodes for highly enhanced ferroelectric solar water splitting, *Nano Res.* 11 (2018) 642–655.

[130] X. Chen, S. Shen, L. Guo, S.S. Mao, Semiconductor-based photocatalytic hydrogen generation, *Chem. Rev.* 110 (2010) 6503–6570.

[131] A. Kudo, H. Kato, S. Nakagawa, Water splitting into H₂ and O₂ on new Sr₂M₂O₇ (M = Nb and Ta) photocatalysts with layered perovskite structures: factors affecting the photocatalytic activity, *J. Phys. Chem. B* 104 (2000) 571–575.

[132] L. Kindermann, D. Das, H. Nickel, K. Hilpert, Chemical compatibility of the LaFeO₃ base perovskites (La_{0.6} Sr_{0.4}) ZFe_{0.8}M_{0.2}O₃ – δ (Z = 1, 0.9; M = Cr, Mn, Co, Ni) with yttria stabilized zirconia, *Solid State Ion.* 89 (1996) 215–220.

[133] J. Mizusaki, N. Mori, H. Takai, Y. Yonemura, H. Minamiue, H. Tagawa, M. Dokiya, H. Inaba, K. Naraya, T. Sasamoto, Oxygen nonstoichiometry and defect equilibrium in the perovskite-type oxides La₁ – xSr_xMnO₃ + d, *Solid State Ion.* 129 (2000) 163–177.

[134] W.-H. Lin, C. Cheng, C.-C. Hu, H. Teng, NaTaO₃ photocatalysts of different crystalline structures for water splitting into H₂ and O₂, *Appl. Phys. Lett.* 89 (2006) 211904.

[135] W. Zhang, J. Tang, J. Ye, Photoluminescence and photocatalytic properties of SrSnO₃ perovskite, *Chem. Phys. Lett.* 418 (2006) 174–178.

[136] I. Papadas, J.A. Christodoulides, G. Kioseoglou, G.S. Armatas, A high surface area ordered mesoporous BiFeO₃ semiconductor with efficient water oxidation activity, *J. Mater. Chem. A* 3 (2015) 1587–1593.

[137] A.T. Raghavender, N. Hoa Hong, K. Joon Lee, M.-H. Jung, Z. Skoko, M. Vasilevskiy, M.F. Cerqueira, A.P. Samantilleke, Nano-ilmenite FeTiO₃: synthesis and characterization, *J. Magn. Magn. Mater.* 331 (2013) 129–132.

[138] X. Zhang, T. Li, Z. Gong, H. Zhao, L. Wang, J. Wan, D. Wang, X. Li, W. Fu, Shape controlled FeTiO₃ nanostructures: crystal facet and photocatalytic property, *J. Alloys. Compd.* 653 (2015) 619–623.

[139] A. Grimaud, O. Diaz-Morales, B. Han, W.T. Hong, Y.-L. Lee, L. Giordano, K.A. Stoerzinger, M.T. Koper, Y. Shao-Horn, Activating lattice oxygen redox

reactions in metal oxides to catalyse oxygen evolution, *Nat. Chem.* 9 (2017) 457.

[140] J.T. Mefford, X. Rong, A.M. Abakumov, W.G. Hardin, S. Dai, A.M. Kolpak, K.P. Johnston, K.J. Stevenson, Water electrolysis on $\text{La}_{1-x}\text{Sr}_x\text{CoO}_3 - \delta$ perovskite electrocatalysts, *Nat. Commun.* 7 (2016) 11053.

[141] X. Cheng, E. Fabbri, M. Nachtegaal, I.E. Castelli, M. El Kazzi, R. Haumont, N. Marzari, T.J. Schmidt, Oxygen evolution reaction on $\text{La}_{1-x}\text{Sr}_x\text{CoO}_3$ perovskites: a combined experimental and theoretical study of their structural, electronic, and electrochemical properties, *Chem. Mater.* 27 (2015) 7662–7672.

[142] B. Han, A. Grimaud, L. Giordano, W.T. Hong, O. Diaz-Morales, L. Yueh-Lin, J. Hwang, N. Charles, K.A. Stoerzinger, W. Yang, Iron-based perovskites for catalyzing oxygen evolution reaction, *J. Phys. Chem. C* 122 (2018) 8445–8454.

[143] H.A. Tahini, X. Tan, U. Schwingenschlögl, S.C. Smith, Formation and migration of oxygen vacancies in SrCoO_3 and their effect on oxygen evolution reactions, *ACS Catal.* 6 (2016) 5565–5570.

[144] H. Yi, T. Choi, S. Choi, Y.S. Oh, S.W. Cheong, Mechanism of the switchable photovoltaic effect in ferroelectric BiFeO_3 , *Adv. Mater.* 23 (2011) 3403–3407.

[145] X. Xu, G. Liu, C. Random, J.T. Irvine, g- C_3N_4 coated SrTiO_3 as an efficient photocatalyst for H_2 production in aqueous solution under visible light irradiation, *Int. J. Hydrogen Energy* 36 (2011) 13501–13507.

[146] R.H. Mitchell, *Perovskites: Modern and Ancient*, Almaz Press Thunder Bay, 2002.

[147] F. Wagner, G. Somorjai, Photocatalytic hydrogen production from water on Pt-free SrTiO_3 in alkali hydroxide solutions, *Nature* 285 (1980) 559.

[148] D.-S. Bae, E.-J. Kim, S.-W. Park, K.-S. Han, Fabrication and microstructure of the SrTiO_3 composite membranes by Sol-Gel process, *J. Mater. Sci.* 41 (2006) 6162–6164.

[149] M. Lv, Y. Xie, Y. Wang, X. Sun, F. Wu, H. Chen, S. Wang, C. Shen, Z. Chen, S. Ni, Bismuth and chromium co-doped strontium titanates and their photocatalytic properties under visible light irradiation, *J. Chem. Soc. Faraday Trans.* 17 (2015) 26320–26329.

[150] Y. Zhang, A.M. Schultz, P.A. Salvador, G.S. Rohrer, Spatially selective visible light photocatalytic activity of $\text{TiO}_2/\text{BiFeO}_3$ heterostructures, *J. Mater. Chem.* 21 (2011) 4168–4174.

[151] S. Cho, J.-W. Jang, W. Zhang, A. Suwardi, H. Wang, D. Wang, J.L. MacManus-Driscoll, Single-crystalline thin films for studying intrinsic properties of $\text{BiFeO}_3-\text{SrTiO}_3$ solid solution photoelectrodes in solar energy conversion, *Chem. Mater.* 27 (2015) 6635–6641.

[152] L. Lu, M. Lv, D. Wang, G. Liu, X. Xu, Efficient photocatalytic hydrogen production over solid solutions $\text{Sr}_{1-x}\text{Bi}_x\text{Ti}_{1-x}\text{Fe}_x\text{O}_3$ ($0 \leq x \leq 0.5$), *Appl. Catal. B* 200 (2017) 412–419.

[153] A. Tsurumaki, H. Yamada, A. Sawa, Impact of Bi deficiencies on ferroelectric resistive switching characteristics observed at p-type Schottky-like $\text{Pt/Bi}_{1-x}\text{FeO}_3$ interfaces, *Adv. Funct. Mater.* 22 (2012) 1040–1047.

[154] H. Yang, H. Luo, H. Wang, I. Usov, N. Suvorova, M. Jain, D. Feldmann, P. Dowden, R. DePaula, Q. Jia, Rectifying current-voltage characteristics of BiFeO_3/Nb -doped SrTiO_3 heterojunction, *Appl. Phys. Lett.* 92 (2008) 102113.

[155] M.R. Shaner, K.T. Fountaine, S. Ardo, R.H. Coridan, H.A. Atwater, N.S. Lewis, Photoelectrochemistry of core-shell tandem junction n-p+ -Si/n-WO₃ microwire array photoelectrodes, *Energy Environ. Sci.* 7 (2014) 779–790.

[156] F.F. Abdi, L. Han, A.H. Smets, M. Zeman, B. Dam, R. Van De Krol, Efficient solar water splitting by enhanced charge separation in a bismuth vanadate-silicon tandem photoelectrode, *Nat. Commun.* 4 (2013) 2195.

[157] J. Smit, H.P.J. Wijn, *Ferrites: Physical Properties of Ferrimagnetic Oxides in Relation to Their Technical Applications*, (1959).

[158] H. O'neill, C. St, Temperature dependence of the cation distribution in zinc ferrite (ZnFe_2O_4) from powder XRD structural refinements, *Eur. J. Mineral.* (1992) 571–580.

[159] S. Nakashima, K. Fujita, K. Tanaka, K. Hirao, T. Yamamoto, I. Tanaka, First-principles XANES simulations of spinel zinc ferrite with a disordered cation distribution, *Phys. Rev. B* 75 (2007) 174443.

[160] T. Kamiyama, K. Haneda, T. Sato, S. Ikeda, H. Asano, Cation distribution in ZnFe_2O_4 fine particles studied by neutron powder diffraction, *Solid State Commun.* 81 (1992) 563–566.

[161] M. Akhtar, M. Nadeem, S. Javaid, M. Atif, Cation distribution in nanocrystalline ZnFe_2O_4 investigated using x-ray absorption fine structure spectroscopy, *J. Phys. Condens. Matter* 21 (2009) 405303.

[162] E. Casbeer, V.K. Sharma, X.-Z. Li, Synthesis and photocatalytic activity of ferrites under visible light: a review, *Sep. Purif. Technol.* 87 (2012) 1–14.

[163] L. Neel, Magnetic properties of ferrites: ferrimagnetism and antiferromagnetism, *Ann. Phys.* 3 (1948) 137–198.

[164] D.S. Mathew, R.-S. Juang, An overview of the structure and magnetism of spinel ferrite nanoparticles and their synthesis in microemulsions, *Chem. Eng. J.* 129 (2007) 51–65.

[165] B. Ren, Y. Huang, C. Han, M.N. Nadagouda, D.D. Dionysiou, Ferrites as photocatalysts for water splitting and degradation of contaminants, ferrites and ferrites: chemistry and applications in sustainable energy and environmental remediation, *Am. Chem. Soc.* (2016) 79–112.

[166] R. Rai, S. Wilser, M. Gumiñak, B. Cai, M. Nakarmi, Optical and electronic properties of NiFe_2O_4 and CoFe_2O_4 thin films, *Appl. Phys. A* 106 (2012) 207–211.

[167] N. Pailhé, A. Wattiaux, M. Gaudon, A. Demourgues, Correlation between structural features and vis-NIR spectra of α - Fe_2O_3 hematite and AFe_2O_4 spinel oxides ($\text{A} = \text{Mg, Zn}$), *J. Solid State Chem.* 181 (2008) 1040–1047.

[168] A. Arimi, L. Megatif, L.I. Granone, R. Dillert, D.W. Bahnemann, Visible-light photocatalytic activity of zinc ferrites, *J. Photochem. Photobiol. A Chem.* (2018).

[169] N. Guijarro, P. Bornoz, M. Prévot, X. Yu, X. Zhu, M. Johnson, X. Jeanbourquin, F. Le Formal, K. Sivula, Evaluating spinel ferrites MFe_2O_4 ($\text{M} = \text{Cu, Mg, Zn}$) as photoanodes for solar water oxidation: prospects and limitations, *Sustain. Energy Fuels* 2 (2018) 103–117.

[170] S. Xuan, W. Jiang, X. Gong, Y. Hu, Z. Chen, Magnetically separable $\text{Fe}_3\text{O}_4/\text{TiO}_2$ hollow spheres: fabrication and photocatalytic activity, *J. Phys. Chem. C* 113 (2009) 553–558.

[171] A. Yanhui, X. Jingjing, F. Degang, B. Long, Y. Chunwei, Deposition of anatase titania onto carbon encapsulated magnetite nanoparticles, *Nanotechnology* 19 (2008) 405604.

[172] K.N. Harish, H.S. Bhojya Naik, P.N. Prashanth Kumar, R. Viswanath, Optical and photocatalytic properties of solar light active Nd-Substituted Ni ferrite catalysts: for environmental protection, *ACS Sustain. Chem. Eng.* 1 (2013) 1143–1153.

[173] H. Zhu, S. Zhang, Y.-X. Huang, L. Wu, S. Sun, Monodisperse $\text{M}_x\text{Fe}_{3-x}\text{O}_4$ ($\text{M} = \text{Fe, Cu, Co, Mn}$) nanoparticles and their electrocatalysis for oxygen reduction reaction, *Nano Lett.* 13 (2013) 2947–2951.

[174] B. Cui, H. Lin, J.-B. Li, X. Li, J. Yang, J. Tao, Core–ring structured NiCo_2O_4 nanoplatelets: synthesis, characterization, and electrocatalytic applications, *Adv. Funct. Mater.* 18 (2008) 1440–1447.

[175] M. Ye, Q. Zhang, Y. Hu, J. Ge, Z. Lu, L. He, Z. Chen, Y. Yin, Magnetically recoverable core–Shell nanocomposites with enhanced photocatalytic activity, *Chem. Eur. J.* 16 (2010) 6243–6250.

[176] W. Wu, S. Zhang, X. Xiao, J. Zhou, F. Ren, L. Sun, C. Jiang, Controllable Synthesis, Magnetic properties, and enhanced photocatalytic activity of spindelike mesoporous α - $\text{Fe}_2\text{O}_3/\text{ZnO}$ core–Shell heterostructures, *ACS Appl. Mater. Interfaces* 4 (2012) 3602–3609.

[177] J. Liu, R. Che, H. Chen, F. Zhang, F. Xia, Q. Wu, M. Wang, Microwave absorption enhancement of multifunctional composite microspheres with spinel Fe_3O_4 cores and anatase TiO_2 shells, *Small* 8 (2012) 1214–1221.

[178] Z. Lou, F. Li, J. Deng, L. Wang, T. Zhang, Branch-like hierarchical heterostructure (α - $\text{Fe}_2\text{O}_3/\text{TiO}_2$): a novel sensing material for trimethylamine gas sensor, *ACS Appl. Mater. Interfaces* 5 (2013) 12310–12316.

[179] Y.-K. Hsu, Y.-C. Chen, Y.-G. Lin, Novel $\text{ZnO}/\text{Fe}_2\text{O}_3$ core–Shell nanowires for photoelectrochemical water splitting, *ACS Appl. Mater. Interfaces* 7 (2015) 14157–14162.

[180] E. Murad, *Properties and Behavior of Iron Oxides As Determined by Mössbauer Spectroscopy*, Iron in Soils and Clay Minerals, Springer, 1988, pp. 309–350.

[181] J. Coey, *Magnetic Properties of Iron in Soil Iron Oxides and Clay Minerals*, Iron in Soils and Clay Minerals, Springer, 1988, pp. 397–466.

[182] N.A. Spaldin, N.D. Mathur, Magnetic materials: fundamentals and device applications, *Phys. Today* 56 (2003) 62–63.

[183] R. Thompson, F. Oldfield, *Magnetic Properties of Natural Materials*, Environmental Magnetism, Springer, 1986, pp. 21–38.

[184] F. Martin-Hernandez, M. García-Hernández, Magnetic properties and anisotropy constant of goethite single crystals at saturating high fields, *Geophys. J. Int.* 181 (2010) 756–761.

[185] M.A. Chaparro, A.M. Sinito, J.C. Bidegain, R.E. de Barrio, Magnetic studies of natural goethite samples from Tharsis, Huelva, Spain, *Geofísica Int.* 45 (2006) 219–230.

[186] S. Kurinobu, K. Tsurusaki, Y. Natui, M. Kimata, M. Hasegawa, Decomposition of pollutants in wastewater using magnetic photocatalyst particles, *J. Magn. Magn. Mater.* 310 (2007) e1025–e1027.

[187] P. Xu, G.M. Zeng, D.L. Huang, C.L. Feng, S. Hu, M.H. Zhao, C. Lai, Z. Wei, C. Huang, G.X. Xie, Use of iron oxide nanomaterials in wastewater treatment: a review, *Sci. Environ. Health* 424 (2012) 1–10.

[188] S. Ma, S. Zhan, Y. Jia, Q. Zhou, Superior antibacterial activity of $\text{Fe}_3\text{O}_4\text{-TiO}_2$ nanosheets under solar light, *ACS Appl. Mater. Interfaces* 7 (2015) 21875–21883.

[189] A. Habibi-Yangjeh, M. Shekofteh-Gohari, Novel magnetic $\text{Fe}_3\text{O}_4/\text{ZnO}/\text{NiWO}_4$ nanocomposites: enhanced visible-light photocatalytic performance through pn heterojunctions, *Sep. Purif. Technol.* 184 (2017) 334–346.

[190] D. Beydoun, R. Amal, G.K.-C. Low, S. McEvoy, Novel photocatalyst: titania-coated magnetite. Activity and photodissolution, *J. Phys. Chem. B* 104 (2000) 4387–4396.

[191] J. Kiwi, Magnetic field effects on photosensitized electron transfer reactions in the presence of titanium dioxide- and cadmium sulfide-loaded particles, *J. Phys. Chem.* 87 (1983) 2274–2276.

[192] H. Okumura, S. Endo, S. Joonwichien, E. Yamasue, K. Ishihara, Magnetic field effect on heterogeneous photocatalysis, *Catal. Today* 258 (2015) 634–647.

[193] H. Okumura, Magnetic field effect (MFE) on heterogeneous photocatalysis and the role of oxygen, *Int. J. Magn. Electromag.* 2 (2016).

[194] M. Wakasa, S. Suda, H. Hayashi, N. Ishii, M. Okano, Magnetic field effect on the photocatalytic reaction with ultrafine TiO_2 particles, *J. Phys. Chem. B* 108 (2004) 11882–11885.

[195] J. Miyakoshi, Effects of static magnetic fields at the cellular level, *Prog. Biophys. Mol. Biol.* 87 (2005) 213–223.

[196] J. Filipič, B. Kraigher, B. Tepuš, V. Kokol, I. Mandic-Mulec, Effects of low-density static magnetic fields on the growth and activities of wastewater bacteria *Escherichia coli* and *Pseudomonas putida*, *Bioresour. Technol.* 120 (2012) 225–232.

[197] H. Wu, L. Wang, Phase transformation-induced crystal plane effect of iron oxide microspine dendrites on gaseous toluene photocatalytic oxidation, *Appl. Surf. Sci.* 288 (2014) 398–404.

[198] Y.L. Pang, S. Lim, H.C. Ong, W.T. Chong, Research progress on iron oxide-based magnetic materials: synthesis techniques and photocatalytic applications, *Ceram. Int.* 42 (2016) 9–34.

[199] J.S. Lee, J. Jang, Hetero-structured semiconductor nanomaterials for photocatalytic applications, *J. Ind. Eng. Chem.* 20 (2014) 363–371.

[200] A.K. Gupta, M. Gupta, Synthesis and surface engineering of iron oxide nanoparticles for biomedical applications, *Biomaterials* 26 (2005) 3995–4021.

[201] D. Arndt, V. Zielasek, W. Dreher, M. Bäumer, Ethylene diamine-assisted synthesis of iron oxide nanoparticles in high-boiling polyols, *J. Colloid Interface Sci.* 417 (2014) 188–198.

[202] S. Shylesh, V. Schünemann, W.R. Thiel, Magnetically separable nanocatalysts: bridges between homogeneous and heterogeneous catalysis, *Angew. Chemie Int. Ed.* 49 (2010) 3428–3459.

[203] J. Liu, L. Wang, J. Wang, L. Zhang, Simple solvothermal synthesis of hydrophobic magnetic monodispersed Fe_3O_4 nanoparticles, *Mater. Res. Bull.* 48 (2013) 416–421.

[204] A.P. Herrera, L. Polo-Corrales, E. Chavez, J. Cabarcas-Bolivar, O.N.C. Uwakweh, C. Rinaldi, Influence of aging time of oleate precursor on the magnetic relaxation of cobalt ferrite nanoparticles synthesized by the thermal decomposition method, *J. Magn. Magn. Mater.* 328 (2013) 41–52.

[205] M. Abbas, B. Parvatheswara Rao, S.M. Naga, M. Takahashi, C. Kim, Synthesis of high magnetization hydrophilic magnetite (Fe_3O_4) nanoparticles in single reaction—Surfactantless polyol process, *Ceram. Int.* 39 (2013) 7605–7611.

[206] W. Wu, Q. He, C. Jiang, Magnetic iron oxide nanoparticles: synthesis and surface functionalization strategies, *Nanoscale Res. Lett.* 3 (2008) 397.

[207] X. Yan, T. Ohno, K. Nishijima, R. Abe, B. Ohtani, Is methylene blue an appropriate substrate for a photocatalytic activity test? A study with visible-light responsive titania, *Chem. Phys. Lett.* 429 (2006) 606–610.

[208] A. Hernández-Ramírez, I. Medina-Ramírez, Semiconducting materials, in: A. Hernández-Ramírez, I. Medina-Ramírez (Eds.), *Photocatalytic Semiconductors: Synthesis, Characterization, and Environmental Applications*, Springer International Publishing, Cham, 2015, pp. 1–40.

[209] E. Domingo, A. Beltrán, R. Sanchis, T. García, B. Solsona, F. Galindo, Photocatalytic activity of mesoporous α - Fe_2O_3 synthesized via Soft chemistry and hard template methods for degradation of azo dye orange II, *Catal. Lett.* 148 (2018) 1289–1295.

[210] S. Demirci, M. Yurduskal, T. Dikici, C. Sarıoğlu, Fabrication and characterization of novel iodine doped hollow and mesoporous hematite (Fe_2O_3) particles derived from sol-gel method and their photocatalytic performances, *J. Hazard. Mater.* 345 (2018) 27–37.

[211] X. Yan, Y. Wu, D. Li, C. Luo, Y. Wang, J. Hu, G. Li, P. Li, H. Jiang, W. Zhang, Facile synthesis of ring-like α - Fe_2O_3 assembly composed of small hematite particles for highly efficient photocatalysis, *J. Mater. Sci. Mater. Electron.* 29 (2018) 2610–2617.

[212] X. Liu, K. Chen, J.-J. Shim, J. Huang, Facile synthesis of porous Fe_2O_3 nanorods and their photocatalytic properties, *J. Saudi Chem. Soc.* 19 (2015) 479–484.

[213] J. Cao, T. Kako, P. Li, S. Ouyang, J. Ye, Fabrication of p-type CaFe_2O_4 nanoflakes for photoelectrochemical hydrogen generation, *Electrochim. commun.* 13 (2011) 275–278.

[214] W.H. Koppenol, J.F. Liebman, The oxidizing nature of the hydroxyl radical. A comparison with the ferryl ion (FeO_2^{+}), *J. Phys. Chem.* 88 (1984) 99–101.

[215] M.I. Franch, J.A. Ayllón, J. Peral, X. Domènech, Enhanced photocatalytic degradation of maleic acid by Fe(III) adsorption onto the TiO_2 surface, *Catal. Today* 101 (2005) 245–252.

[216] H. Yu, H. Irie, Y. Shimodaira, Y. Hosogi, Y. Kuroda, M. Miyauchi, K. Hashimoto, An efficient visible-light-Sensitive Fe(III)-Grafted TiO_2 photocatalyst, *J. Phys. Chem. C* 114 (2010) 16481–16487.

[217] M. Lezner, E. Grabowska, Z. A, Preparation and photocatalytic activity of iron-modified titanium dioxide photocatalyst, *Physicochem. Problems Min. Process.* 48 (2012) 193–200.

[218] S. Li, G.W. Qin, Y. Zhang, W. Pei, L. Zuo, C. Esling, Anisotropic growth of Iron oxyhydroxide nanorods and their photocatalytic activity, *Adv. Eng. Mater.* 12 (2010) 1082–1085.

[219] H. Yang, S. Zhang, R. Cao, X. Deng, Z. Li, X. Xu, Constructing the novel ultrafine amorphous iron oxyhydroxide/g- C_3N_4 nanosheets heterojunctions for highly improved photocatalytic performance, *Sci. Rep.* 7 (2017) 8686.

[220] T. Zhu, W. Li Ong, L. Zhu, G. Wei Ho, TiO_2 fibers supported β - FeOOH nanostuctures as efficient visible light photocatalyst and room temperature sensor, *Sci. Rep.* 5 (2015) 10601.

[221] Z. Liang, Q. Wen, X. Wang, F. Zhang, Y. Yu, Chemically stable and reusable nano zero-valent iron/graphite-like carbon nitride nanohybrid for efficient photocatalytic treatment of Cr(VI) and rhodamine B under visible light, *Appl. Surf. Sci.* 386 (2016) 451–459.

[222] E. Petala, M. Baikousi, M.A. Karakassides, G. Zoppiello, J. Filip, J. Tucek, K.C. Vasilopoulos, J. Pechousek, R. Zboril, Synthesis, physical properties and application of the zero-valent iron/titanium dioxide heterocomposite having high activity for the sustainable photocatalytic removal of hexavalent chromium in water, *J. Chem. Soc. Faraday Trans.* 18 (2016) 10637–10646.

[223] F. Gao, X. Chen, K. Yin, S. Dong, Z. Ren, F. Yuan, T. Yu, Z. Zou, J.M. Liu, Visible-light photocatalytic properties of weak magnetic BiFeO_3 nanoparticles, *Adv. Mater.* 19 (2007) 2889–2892.

[224] L. Jia, T. Ding, Q. Li, Y. Tang, Study of photocatalytic performance of SrFeO_{3-x} by ultrasonic radiation, *Catal. Commun.* 8 (2007) 963–966.

[225] H.-P. Lin, C.-C. Chen, W.W. Lee, Y.-Y. Lai, J.-Y. Chen, Y.-Q. Chen, J.-Y. Fu, Synthesis of a SrFeO_{3-x} /g- C_3N_4 heterojunction with improved visible-light photocatalytic activities in chloramphenicol and crystal violet degradation, *RSC Adv.* 6 (2016) 2323–2336.

[226] K.K. Singh, K.K. Senapati, K.C. Sarma, Synthesis of superparamagnetic Fe_3O_4 nanoparticles coated with green tea polyphenols and their use for removal of dye pollutant from aqueous solution, *J. Environ. Chem. Eng.* 5 (2017) 2214–2221.

[227] V.V. Tolmacheva, V.V. Apyari, E.V. Kochuk, S.G. Dmitrienko, Magnetic adsorbents based on iron oxide nanoparticles for the extraction and preconcentration of organic compounds, *J. Anal. Chem.* 71 (2016) 321–338.

[228] S. Sun, X. Yang, Y. Zhang, F. Zhang, J. Ding, J. Bao, C. Gao, Enhanced photocatalytic activity of sponge-like ZnFe_2O_4 synthesized by solution combustion method, *Prog. Nat. Sci.* 22 (2012) 639–643.

[229] P.N. Gaikwad, P.P. Hankare, T.M. Wandre, K.M. Garadkar, R. Sasikala, Photocatalytic performance of magnetically separable Fe, N co-doped TiO_2 -cobalt ferrite nanocomposite, *Mater. Sci. Eng. B* 205 (2016) 40–45.

[230] S.D. Kulkarni, S. Kumbar, S.G. Menon, K.S. Choudhari, S. C, Magnetically separable core-shell ZnFe_2O_4 @ ZnO nanoparticles for visible light photodegradation of methyl orange, *Mater. Res. Bull.* 77 (2016) 70–77.

[231] J. Wang, Q. Deng, M. Li, K. Jiang, J. Zhang, Z. Hu, J. Chu, Copper ferrites@reduced graphene oxide anode materials for advanced lithium storage applications, *Sci. Rep.* 7 (2017) 8903.

[232] L. Zheng, H. Xu, F. Pi, Y. Zhang, X. Sun, Synthesis of Fe_3O_4 @ mTiO_2 nanocomposites for the photocatalytic degradation of Monocrotaphos under UV illumination, *RSC Adv.* 6 (2016) 87273–87281.

[233] Y. Fu, H. Chen, X. Sun, X. Wang, Combination of cobalt ferrite and graphene: high-performance and recyclable visible-light photocatalysis, *Appl. Catal. B* 111–112 (2012) 280–287.

[234] K. Byrapa, S. Ohara, T. Adschari, Nanoparticles synthesis using supercritical fluid technology “towards biomedical applications, *Adv. Drug Deliv. Rev.* 60 (2008) 299–327.

[235] G.U. Singh, M. Ramovatar, R. Paulraj, Iron oxide nanoparticles induced cytotoxicity, oxidative stress and DNA damage in lymphocytes, *J. Appl. Toxicol.* 37 (2017) 1232–1244.

[236] N. Tran, A. Mir, D. Mallik, A. Sinha, S. Nayar, T.J. Webster, Bactericidal effect of iron oxide nanoparticles on *Staphylococcus aureus*, *Int. J. Nanomed.* 5 (2010) 277–283.

[237] P. Nehra, R.P. Chauhan, N. Garg, K. Verma, Antibacterial and antifungal activity of chitosan coated iron oxide nanoparticles, *Br. J. Biomed. Sci.* 75 (2018) 13–18.

[238] R.A. Ismail, G.M. Sulaiman, S.A. Abdulrahman, T.R. Marzoog, Antibacterial activity of magnetic iron oxide nanoparticles synthesized by laser ablation in liquid, *Mater. Sci. Eng. C* 53 (2015) 286–297.

[239] S.M.H. Al-Jawad, A.A. Taha, M.M. Salim, Synthesis and characterization of pure and Fe doped TiO_2 thin films for antimicrobial activity, *Opt. Int. J. Light Electron. Opt.* 142 (2017) 42–53.

[240] T.A. Egerton, S.A.M. Kosa, P.A. Christensen, Photoelectrocatalytic disinfection of *E. Coli* suspensions by iron doped TiO_2 , *J. Chem. Soc. Faraday Trans.* 8 (2006) 398–406.

[241] M. Mangayam, J. Kiwi, S. Giannakis, C. Pulgarin, I. Zivkovic, A. Magrez, S. Rtimi, FeO_x magnetization enhancing *E. Coli* inactivation by orders of magnitude on Ag-TiO_2 nanotubes under sunlight, *Appl. Catal. B* 202 (2017) 438–445.

[242] T. Nardi, S. Rtimi, C. Pulgarin, Y. LeTerrier, Antibacterial surfaces based on functionally graded photocatalytic Fe_3O_4 @ TiO_2 core-shell nanoparticle/epoxy composites, *RSC Adv.* 5 (2015) 105416–105421.

[243] S. Rtimi, R. Sanjines, J. Kiwi, C. Pulgarin, M. Bensimon, I. Khmel, V. Nadochenko, Innovative photocatalyst (FeO_x - TiO_2): transients induced by femtosecond laser pulse leading to bacterial inactivation under visible light, *RSC Adv.* 5 (2015) 101751–101759.

[244] S. Rtimi, C. Pulgarin, R. Sanjines, J. Kiwi, Novel FeOx -polyethylene transparent films: synthesis and mechanism of surface regeneration, *RSC Adv.* 5 (2015) 80203–80211.

[245] K.K. Kefeni, B.B. Mamba, T.A.M. Msagati, Application of spinel ferrite nanoparticles in water and wastewater treatment: a review, *Sep. Purif. Technol.* 188 (2017) 399–422.

[246] K. Biswas, D. De, J. Bandyopadhyay, N. Dutta, S. Rana, P. Sen, S.K. Bandyopadhyay, P.K. Chakraborty, Enhanced polarization, magnetic response and pronounced antibacterial activity of bismuth ferrite nanorods, *Mater. Chem. Phys.* 195 (2017) 207–212.

[247] N. Sanpo, C.C. Berndt, J. Wang, Microstructural and antibacterial properties of zinc-substituted cobalt ferrite nanowhiskers synthesized by sol-gel methods, *J. Appl. Phys.* 112 (2012) 084333.

[248] N. Sanpo, C.C. Berndt, C. Wen, J. Wang, Transition metal-substituted cobalt ferrite nanoparticles for biomedical applications, *Acta Biomater.* 9 (2013) 5830–5837.

[249] N. Sanpo, C. Wen, C.C. Berndt, J. Wang, Antibacterial properties of spinel ferrite nanoparticles, in: A. Méndez-Vilas (Ed.), *Microbial Pathogens and Strategies for Combating Them: Science, Technology and Education*, Formatek Research Center, Spain, 2013, pp. 239–250.

[250] Y. Xu, Q. Liu, M. Xie, S. Huang, M. He, L. Huang, H. Xu, H. Li, Synthesis of zinc ferrite/silver iodide composite with enhanced photocatalytic antibacterial and pollutant degradation ability, *J. Colloid Interface Sci.* 528 (2018) 70–81.

[251] P.V. Kamat, J. Bisquert, Solar fuels. Photocatalytic hydrogen generation, *J. Phys. Chem. C* 117 (2013) 14873–14875.

[252] A. Hakki, Y. AlSalka, C.B. Mendive, J. Ubogui, P.C. dos Santos Claro, D. Bahnenmann, Hydrogen production by heterogeneous photocatalysis, in: K. Wandelt (Ed.), *Encyclopedia of Interfacial Chemistry*, Elsevier, Oxford, 2018, pp. 413–419.

[253] A. Hellman, R.G.S. Pala, First-principles study of photoinduced water-splitting on Fe_2O_3 , *J. Phys. Chem. C* 115 (2011) 12901–12907.

[254] A. Syed Nabeel, H. Waseem, Heterogeneous photocatalysis and its potential applications in water and wastewater treatment: a review, *Nanotechnology* 29 (2018) 342001.

[255] C.-J. Chang, Z. Lee, M. Wei, C.-C. Chang, K.-W. Chu, Photocatalytic hydrogen production by magnetically separable Fe_3O_4 @ ZnS and NiCo_2O_4 @ ZnS core-shell nanoparticles, *Int. J. Hydrogen Energy* 40 (2015) 11436–11443.

[256] R. Dholam, N. Patel, M. Adami, A. Miotello, Hydrogen production by photocatalytic water-splitting using Cr- or Fe-doped TiO_2 composite thin films

photocatalyst, *Int. J. Hydrogen Energy* 34 (2009) 5337–5346.

[257] A. Madhumitha, V. Preethi, S. Kanmani, Photocatalytic hydrogen production using TiO_2 coated iron-oxide core shell particles, *Int. J. Hydrogen Energy* 43 (2018) 3946–3956.

[258] C.-J. Chang, W.-C. Tsai, CuS_nS decorated Fe_3O_4 nanoparticles as magnetically separable composite photocatalysts with excellent hydrogen production activity, *Int. J. Hydrogen Energy* (2018).

[259] F. Wang, T. Shen, Z. Fu, Y. Lu, C. Chen, Enhanced photocatalytic water-splitting performance using Fe-doped hierarchical TiO_2 ball-flowers, *Nanotechnology* 29 (2018) 035702.

[260] H.G. Kim, P.H. Borse, W. Choi, J.S. Lee, Photocatalytic Nanodiodes for Visible-Light Photocatalysis, *Angew. Chemie Int. Ed.* 44 (2005) 4585–4589.

[261] J. Chen, D. Zhao, Z. Diao, M. Wang, L. Guo, S. Shen, Bifunctional modification of graphitic carbon nitride with MgFe_2O_4 for enhanced photocatalytic hydrogen generation, *ACS Appl. Mater. Interfaces* 7 (2015) 18843–18848.

[262] H.G. Kim, P.H. Borse, J.S. Jang, E.D. Jeong, O.-S. Jung, Y.J. Suh, J.S. Lee, Fabrication of $\text{CaFe}_2\text{O}_4/\text{MgFe}_2\text{O}_4$ bulk heterojunction for enhanced visible light photocatalysis, *Chem. Commun.* (2009) 5889–5891.

[263] D. Hong, Y. Yamada, M. Sheehan, S. Shikano, C.-H. Kuo, M. Tian, C.-K. Tsung, S. Fukuzumi, Mesoporous nickel ferrites with spinel structure prepared by an aerosol spray pyrolysis method for photocatalytic hydrogen evolution, *ACS Sustain. Chem. Eng.* 2 (2014) 2588–2594.

[264] S. Saadi, A. Bouguelia, M. Trari, Photoassisted hydrogen evolution over spinel CuM_2O_4 ($\text{M} = \text{Al, Cr, Mn, Fe and Co}$), *Renew. Energy* 31 (2006) 2245–2256.

[265] R. Dom, R. Subasri, N.Y. Hebalkar, A.S. Chary, P.H. Borse, Synthesis of a hydrogen producing nanocrystalline ZnFe_2O_4 visible light photocatalyst using a rapid microwave irradiation method, *RSC Adv.* 2 (2012) 12782–12791.

[266] H. Song, L. Zhu, Y. Li, Z. Lou, M. Xiao, Z. Ye, Preparation of ZnFe_2O_4 nanostructures and highly efficient visible-light-driven hydrogen generation with the assistance of nanoheterostructures, *J. Mater. Chem. A* 3 (2015) 8353–8360.

[267] O. Zandi, T.W. Hamann, The potential versus current state of water splitting with hematite, *J. Chem. Soc. Faraday Trans.* 17 (2015) 22485–22503.

[268] T. Lindgren, L. Vayssières, H. Wang, S. Lindquist, Photo-oxidation of Water at hematite electrodes, in: A. Kokorin, D. Bahnemann (Eds.), *Chemical Physics of Nanostructured Semiconductors*, CRC Press, London, 2003.

[269] S.U.M. Khan, J.O.M. Bockris, A model for electron transfer at the illuminated p-type semiconductor-solution interface, *J. Phys. Chem.* 88 (1984) 2504–2515.

[270] K.G. McGregor, M. Calvin, J.W. Otvos, Photoeffects in Fe_2O_3 sintered semiconductors, *J. Appl. Phys.* 50 (1979) 369–373.

[271] S. Licht, B. Wang, S. Mukerji, T. Soga, M. Umeho, H. Tributsch, Efficient solar water splitting, exemplified by RuO_2 -catalyzed AlGaAs/Si photoelectrolysis, *J. Phys. Chem. B* 104 (2000) 8920–8924.

[272] A. Kay, I. Cesar, M. Grätzel, New benchmark for water photooxidation by nanostructured $\alpha\text{-Fe}_2\text{O}_3$ films, *J. Am. Chem. Soc.* 128 (2006) 15714–15721.

[273] J.Y. Kim, G. Magesh, D.H. Youn, J.-W. Jang, J. Kubota, K. Domen, J.S. Lee, Single-crystalline, wormlike hematite photoanodes for efficient solar water splitting, *Sci. Rep.* 3 (2013) 2681.

[274] K. Sivula, R. van de Krol, Semiconducting materials for photoelectrochemical energy conversion, *Nat. Rev. Mater.* 1 (2016) 15010.

[275] S. Kevin, L.F. Florian, Gt. Michael, Solar water splitting: progress using hematite ($\alpha\text{-Fe}_2\text{O}_3$) photoelectrodes, *ChemSusChem* 4 (2011) 432–449.

[276] K.D. Malviya, H. Dotan, D. Shlenkevich, A. Tsyganok, H. Mor, A. Rothschild, Systematic comparison of different dopants in thin film hematite ($\alpha\text{-Fe}_2\text{O}_3$) photoanodes for solar water splitting, *J. Mater. Chem. A* 4 (2016) 3091–3099.

[277] K. Sivula, F.L. Formal, M. Grätzel, $\text{WO}_3\text{-Fe}_2\text{O}_3$ photoanodes for water splitting: a host scaffold, guest absorber approach, *Chem. Mater.* 21 (2009) 2862–2867.

[278] S.D. Tilley, M. Cornuz, K. Sivula, M. Grätzel, Light-Induced Water Splitting with Hematite: Improved Nanostructure and Iridium Oxide Catalysis, *Angew. Chemie Int. Ed.* 49 (2010) 6405–6408.

[279] K.J. McDonald, K.-S. Choi, Synthesis and photoelectrochemical properties of $\text{Fe}_2\text{O}_3/\text{ZnFe}_2\text{O}_4$ composite photoanodes for use in solar water oxidation, *Chem. Mater.* 23 (2011) 4863–4869.

[280] W.D. Chemelewski, H.-C. Lee, J.-F. Lin, A.J. Bard, C.B. Mullins, Amorphous FeOOH oxygen evolution reaction catalyst for photoelectrochemical water splitting, *J. Am. Chem. Soc.* 136 (2014) 2843–2850.

[281] X. Zhang, L. An, J. Yin, P. Xi, Z. Zheng, Y. Du, Effective construction of high-quality Iron oxy-hydroxides and Co-doped Iron oxy-hydroxides nanostructures: towards the promising oxygen evolution reaction application, *Sci. Rep.* 7 (2017) 43590.

[282] H. Yang, Y. Mao, M. Li, P. Liu, Y. Tong, Electrochemical synthesis of CoFe_2O_4 porous nanosheets for visible light driven photoelectrochemical applications, *New J. Chem.* 37 (2013) 2965–2968.

[283] K. Sekizawa, T. Nonaka, T. Arai, T. Morikawa, Structural improvement of CaFe_2O_4 by metal doping toward enhanced cathodic photocurrent, *ACS Appl. Mater. Interfaces* 6 (2014) 10969–10973.

[284] A.A. Tahir, K.G.U. Wijayantha, Photoelectrochemical water splitting at nanostructured ZnFe_2O_4 electrodes, *J. Photochem. Photobiol. A Chem.* 216 (2010) 119–125.

[285] B. Klahr, T. Hamann, Water oxidation on hematite photoelectrodes: insight into the nature of Surface States through *in situ* spectroelectrochemistry, *J. Phys. Chem. C* 118 (2014) 10393–10399.

[286] C.Y. Cummings, F. Marken, L.M. Peter, A.A. Tahir, K.G.U. Wijayantha, Kinetics and mechanism of light-driven oxygen evolution at thin film $\alpha\text{-Fe}_2\text{O}_3$ electrodes, *Chem. Commun.* 48 (2012) 2027–2029.

[287] A.J. Cowan, C.J. Barnett, S.R. Pendlebury, M. Barroso, K. Sivula, M. Grätzel, J.R. Durrant, D.R. Klug, Activation energies for the rate-limiting step in water photooxidation by nanostructured $\alpha\text{-Fe}_2\text{O}_3$ and TiO_2 , *J. Am. Chem. Soc.* 133 (2011) 10134–10140.

[288] A.J. Cowan, J.R. Durrant, Long-lived charge separated states in nanostructured semiconductor photoelectrodes for the production of solar fuels, *Chem. Soc. Rev.* 42 (2013) 2281–2293.

[289] S.R. Pendlebury, M. Barroso, A.J. Cowan, K. Sivula, J. Tang, M. Grätzel, D. Klug, J.R. Durrant, Dynamics of photogenerated holes in nanocrystalline $\alpha\text{-Fe}_2\text{O}_3$ electrodes for water oxidation probed by transient absorption spectroscopy, *Chem. Commun.* 47 (2011) 716–718.

[290] T.P. Trainor, A.M. Chaka, P.J. Eng, M. Newville, G.A. Waychunas, J.G. Catalano, G.E. Brown, Structure and reactivity of the hydrated hematite (0001) surface, *Surf. Sci.* 573 (2004) 204–224.

[291] K.M.H. Young, B.M. Klahr, O. Zandi, T.W. Hamann, Photocatalytic water oxidation with hematite electrodes, *Catal. Sci. Technol.* 3 (2013) 1660–1671.

[292] Boris I. Kharisov, Oxana V. Kharissova, H.V. Rasika Dias, Ubaldo Ortiz Méndez, Idalia Gómez, Y.P. de la Fuente, A.V. Dimas, Iron-based Nanomaterials in the Catalysis, Advanced Catalytic Materials - Photocatalysis and Other Current Trends, InTech, 2016, p. 35.

[293] R.S. Jack, G.A. Ayoko, M.O. Adebajo, R.L. Frost, A review of iron species for visible-light photocatalytic water purification, *Environ. Sci. Pollut. Res. Int.* 22 (2015) 7439–7449.

[294] G.-D. Fang, D.-M. Zhou, D.D. Dionysiou, Superoxide mediated production of hydroxyl radicals by magnetite nanoparticles: demonstration in the degradation of 2-chlorobiphenyl, *J. Hazard. Mater.* 250–251 (2013) 68–75.

[295] R.C.C. Costa, Md.Ft.F. Lelis, L.C.A. Oliveira, J.D. Fabris, J.D. Ardisson, R.R.V.A. Rios, C.N. Silva, R.M. Lago, Remarkable effect of Co and Mn on the activity of $\text{Fe}_{3-x}\text{M}_x\text{O}_4$ promoted oxidation of organic contaminants in aqueous medium with H_2O_2 , *Catal. Commun.* 4 (2003) 525–529.

[296] R. Sharma, V. Kumar, S. Bansal, S. Singhal, Assortment of magnetic nanospins for activation of distinct inorganic oxidants in photo-Fentons process, *J. Mol. Catal. A Chem.* 402 (2015) 53–63.